A La Niña-like climate response to south African biomass burning aerosol in CESM simulations

Anahita Amiri-Farahani*[1,2], Robert J. Allen[2], King-Fai Li[1], Pierre Nabat[3], Daniel M. Westervelt[4]

[1]University of California Riverside, Department of Environmental Sciences, Riverside, CA, USA
[2]University of California Riverside, Department of Earth and Planetary Sciences, Riverside, CA, USA
[3]Centre National de Recherches Météorologiques, UMR3589, Météo-France-CNRS, Toulouse, France
[4]Lamont-Doherty Earth Observatory, Columbia University, Palisades, New York, USA

* Now at Climate and Space Sciences and Engineering, University of Michigan, Ann Arbor, USA

Key Points:

- South African biomass burning aerosol locally warms the atmosphere
- This heating drives local ascent and divergence, triggering a teleconnection to the Pacific
- The Pacific Walker circulation strengthens and a La Niña-like response develops

Corresponding author: R.J. Allen, rjallen@ucr.edu

Abstract

The climate response to atmospheric aerosols, including their effects on dominant modes of climate variability like El Niño Southern Oscillation (ENSO), remains highly uncertain. This is due to several sources of uncertainty, including aerosol emission, transport, removal, vertical distribution, and radiative properties. Here, we conduct coupled ocean atmosphere simulations with two versions of the Community Earth System Model (CESM) driven by semi-empirical fine-mode aerosol direct radiative effects without dust and sea salt. Aerosol atmospheric heating off the west coast of Africa−most of which is due to biomass burning−leads to a significant atmospheric dynamical response, including localized ascent and upper-level divergence. Coupled Model Intercomparison Project version 6 (CMIP6) biomass burning simulations support this response. Moreover, CESM shows that the anomalous aerosol heating in the Atlantic triggers an atmospheric teleconnection to the tropical Pacific, including strengthening of the Walker circulation. The easterly trade winds accelerate, and through coupled ocean-atmosphere processes and the Bjerknes feedback, a La Niña-like response develops. Observations also support a relationship between south African biomass burning emissions and ENSO, with La Niña events preceding strong south African biomass burning in boreal fall. Our simulations suggest a possible two-way feedback between ENSO and south African biomass burning, with La Niña promoting more biomass burning emissions, which may then strengthen the developing La Niña.

1 Introduction

The burden of tropospheric aerosols has increased since preindustrial times due to anthropogenic activities (S. Smith et al., 2004; Bond et al., 2007). Aerosols affect the climate system in several ways, including the scattering and absorbing of solar radiation (direct effects), as well as through modification of cloud properties (indirect effects). In terms of direct effects, sulfate aerosols primarily reflect solar radiation and cause cooling of the climate system. Conversely, black carbon (BC), the strongest absorbing aerosol species, primarily absorbs solar radiation and warms the atmosphere (Ramanathan et al., 2001). The most recent Intergovernmental Panel on Climate Change (IPCC) assessment report quantifies the aerosol direct radiative forcing (RF) at $-0.35\pm0.5\ Wm^{-2}$ (Boucher et al., 2013). Larger uncertainty exists with BC, with a direct RF of 0.71 W m^{-2} and 90% confidence bounds of 0.08 to 1.27 W m^{-2} (Bond et al., 2013). This large uncertainty is related to several factors, including uncertainty in BC emission inventories, absorption aerosol optical depth, and vertical profile (Ramanathan & Carmichael, 2008; Koch et al., 2009; Ming et al., 2010; Zarzycki & Bond, 2010; C. E. Chung et al., 2012; Ban-Weiss et al., 2012; Bond et al., 2013; Allen & Landuyt, 2014; Cohen & Wang, 2014; Myhre & Samset, 2015; Samset & Myhre, 2015).

Some of the uncertainty associated with aerosols, including BC, is related to biomass burning. The direct RF of biomass burning aerosol is not well constrained, with a central estimate of 0.0 W m^{-2} and a corresponding uncertainty range of −0.20 to +0.20 W m^{-2} (Myhre et al., 2013). Recent studies also suggest that biomass burning aerosols yields a relatively large negative indirect effect of about −1 W m^{-2} (Ward et al., 2012; Grandey et al., 2016; Jiang et al., 2016; Landry et al., 2017; Lu et al., 2018). ∼40% of global BC emissions originate from landscape fires, including agricultural waste burning, grassland fire, peat fire, and various types of forest fire (van Marle et al., 2017; van der Werf et al., 2017). A best-guess uncertainty assessment for carbon emissions associated with biomass burning at regional scales is at least 50%, but likely higher in areas where small fire burned area is important (van der Werf et al., 2017). Furthermore, simulated aerosol optical depth (AOD) in regions with large biomass burning emissions (e.g., south Africa) is likely underestimated (by a factor of ∼2-4) by most models (Kaiser et al., 2012; Tosca et al., 2013; Shindell et al., 2013).

Despite the short atmospheric lifetime of aerosols and their heterogeneous spatial distribution, aerosols can alter both local and remote atmospheric circulation (Ramanathan et al., 2005; Shindell et al., 2012; Lewinschal et al., 2013; Undorf et al., 2018; Wilcox et al., 2019). Previous studies show that aerosols are linked to several circulation responses, including meridional shifts of the Intertropical Convergence Zone (ITCZ) (Hwang et al., 2013; Allen et al., 2015; Allen, 2015; Rotstayn, Collier, & Luo, 2015; Westervelt et al., 2018) and the associated decrease in Sahel rainfall (Biasutti & Giannini, 2006; Rotstayn & Lohmann, 2002; Undorf et al., 2018). Aerosols have also been associated with perturbing the width of the tropical belt (Allen et al., 2012b; Kovilakam & Mahajan, 2015; Allen & Ajoku, 2016), an equatorward shift of the Northern Hemisphere storm tracks (Kristjansson et al., 2005; Ming & Ramaswamy, 2009), and weakening of the global monsoon system, including the south Asian monsoon (Meehl et al., 2008; Bollasina et al., 2011; Polson et al., 2014; Guo et al., 2016; Z. Li et al., 2016).

Absorbing aerosol, which directly heats the atmosphere, may be particularly efficient at perturbing atmospheric circulation and precipitation due to its ability to increase tropospheric stability and perturb meridional temperature gradients (C. Chung & Ramanathan, 2006; Meehl et al., 2008; Ming et al., 2010; Allen et al., 2012a, 2012b; Kovilakam & Mahajan, 2015; Shen & Ming, 2018). Absorbing aerosol over the southeastern Atlantic Ocean, due to south African biomass burning during the dry season (∼July-October), may also influence the large-scale atmospheric circulation (Ramanathan & Carmichael, 2008; Randles & Ramaswamy, 2010; Sakaeda et al., 2011). Randles and Ramaswamy (2010) show that strong atmospheric absorption can increase upward motion and low-level convergence over southern Africa during the dry season. These changes increase sea level pressure over land in the biomass burning region and enhance the hydrologic cycle by increasing clouds, atmospheric water vapor, and precipitation. Similarly, Tosca et al. (2013) perform biomass burning simulations (direct and semi-direct effects only) constrained by satellite aerosol AOD. They find significant model underestimation of observed AOD in the three major tropical burning regions, including south Africa. For these regions, they apply a scaling factor, ranging from 1.45 to 2.40, to bring the AODs into agreement with the satellite time series. They show that fire emissions reduce global surface temperatures by 0.13K, weaken the Hadley circulation, and perturb precipitation patterns, including precipitation reductions along the equator and over tropical forests in South America, Africa and equatorial Asia.

Dominant modes of climate variability, such as El Niño Southern Oscillation (ENSO) and the North Atlantic Oscillation (NAO), affect weather, economies and ecosystems regionally and worldwide. Several studies suggest that aerosols are capable of perturbing these dominant modes of climate variability. Booth et al. (2012) found that aerosols account for much of the simulated multi-decadal variability of North Atlantic sea surface temperatures, and associate this to aerosol-microphysical effects. Tang et al. (2018) found BC drives a positive NAO response and a poleward shift of the Atlantic storm track, leading to drying of the Mediterranean. A similar positive NAO-like response to semi-empirical aerosol forcing (C. E. Chung et al., 2005) was also reported by Allen and Sherwood (2011). Anthropogenic aerosols may also be able to modify the Pacific Decadal Oscillation (PDO), thereby altering the width of the tropical belt (Allen et al., 2014). Similarly, Takahashi and Watanabe (2016) found sulfate aerosols are responsible for one-third of the 1991-2010 trade-wind intensification in the tropical Pacific. Westervelt et al. (2018) showed that the precipitation response to future projected reductions in aerosol emissions is largest in the tropics and projects onto ENSO. Tropical Pacific sea salt emissions have also been associated with enhancing ESNO variability (Yang et al., 2016), and mid-latitude/Arctic BC with increasing the frequency of extreme ENSO events (Lou et al., 2019). However, no studies to date have directly linked biomass burning aerosols to ENSO.

In this study we investigate the climate response to the direct radiative effects of semi-empirical fine-mode aerosol without dust and salt (C. E. Chung et al., 2016). Dust and sea salt are not included so that our aerosol direct radiative effect predominantly represents the anthropogenic aerosol direct radiative effect (i.e., smaller, fine-mode particles). Indirect aerosol effects, which are likely important, are not included here. We use semi-empirical aerosol radiative effects to bypass the aforementioned uncertainty in absorbing aerosols in most models, including likely underestimation of biomass aerosols. Simulations are conducted using both a dynamical ocean as well as fixed sea surface temperatures (fSST) using two atmospheric versions of the Community Earth System Model (CESM) (Hurrell et al., 2013). Our simulations show that aerosol direct radiative effects can trigger a La Niña-like climate response in the tropical Pacific, which we relate to African biomass burning aerosol. These conclusions are also supported with CAM5 simulations using default prognostic aerosols, which include aerosol indirect effects, as well as aerosol-meteorology coupling. This paper is organized as follows: Section 2 describes our methodology, including our models, observations and aerosol direct radiative effects. Results are presented in Section 3 and a Discussion and Conclusion follows in Section 4.

2 Methodology

2.1 Semi-empirical aerosol direct radiative effects

Two general approaches are used to understand aerosol impacts on the climate system. In bottom-up approaches, the physical properties of the aerosol are specified through aerosol and precursor emissions. Aerosol radiative effects can then be quantified using a global model by inferring optical and cloud active properties. In contrast, top-down approaches involve prescribing aerosol optical properties based on a combination of observations and models. Several sources of uncertainty are involved with traditional bottom-up aerosol simulations, including emissions, transport, vertical distribution and removal (Textor et al., 2006; Bond et al., 2013; Allen & Landuyt, 2014; Park & Allen, 2015). To bypass some of these uncertainties, we use the top-down approach by prescribing a monthly varying climatology of semi-empirical fine mode aerosol direct radiative effects without dust and sea salt (C. E. Chung et al., 2016) into CESM. Our simulations do not include aerosol cloud microphysical (indirect) effects.

Our semi-empirical direct aerosol radiative effect (C. E. Chung et al., 2016) is based on the approach of C. E. Chung et al. (2005) and K. Lee and Chung (2013). Satellite aerosol optical depth (AOD) from Moderate Resolution Imaging Spectroradiometer (MODIS) and Multi-angle Imaging SpectroRadiometer (MISR) is nudged towards AErosol RObotic NETwork (AERONET) AOD to obtain globally reliable AOD from 2001-2010. The AOD Angstrom exponent is also derived by adjusting the satellite data towards AERONET data. Fine-mode aerosol optical depth (fAOD) at 500 nm is obtained by using AERONET fAOD and total AOD to derive fine-mode fraction (FMF). AOD Angstrom exponent data is converted into FMF data, which is then nudged towards AERONET FMF data to derive reliable FMF and fAOD over the globe. Observational data gaps−which are primarily confined to polar regions−are filled by Goddard Chemistry Aerosol Radiation and Transport (GOCART) model. Aerosol optical properties, the single-scattering albedo (SSA) and asymmetry parameter (ASY) for the total aerosol are derived by nudging GOCART simulated values towards the AERONET data. GOCART accurately simulates most of the prominent AOD features in the satellite observations, within a factor of two for aerosol source and outflow areas (Chin et al., 2002). However, several GOCART biases have been identified, including an underestimation of aerosol extinction over India, overestimation of aerosol extinction in dust source regions, and overestimation of aerosol aloft over mid-latitude transport regions (Yu et al., 2010). Aerosol vertical profiles are obtained from the space-born Cloud-Aerosol Lidar with Orthogonal Polarization (CALIOP) (Liu et al., 2009; Winker et al., 2013). The direct aerosol effect for each month is obtained by incorporating the integrated global aerosol data into the Monte-Carlo Aerosol Cloud Radiation (MACR) model (Podgorny et al., 2000; Choi & Chung, 2014).

Sensitivity tests were performed to quantify the uncertainty (primarily due to AOD and SSA) in the observationally constrained fine-mode aerosol direct radiative effect used here (C. E. Chung et al., 2016). Based on modifying BC AOD and BC/organic aerosol (OA) SSA, fine-mode aerosols yield atmospheric absorption ranging from 3.63 W m^{-2} (least absorbing case) to 4.08 W m^{-2} (most absorbing case). This implies an uncertainty range of about ± 0.25 W m^{-2}. Additional information pertaining to the semi-empirical fine-mode direct aerosol radiative effect is located in the Supplement.

Figure 1 shows the annual mean atmospheric solar absorption (F_{ATM}) and reduction in surface solar radiation (F_{SFC}) for semi-empirical fine-mode aerosol direct effect without dust and sea salt. We note that all quoted magnitudes of the semi-empirical aerosol data, including F_{ATM} and F_{SFC} represent a present-day "aerosol direct radiative effect" (DRE), and not a traditionally defined aerosol radiative forcing. An aerosol forcing is estimated as the difference between present day and preindustrial aerosol radiative effects. Large uncertainty exists in preindustrial aerosol effects and this was not estimated by C. E. Chung et al. (2016). The global annual average F_{ATM} and reduction in surface solar radiation F_{SFC} is +3.64 W m^{-2} and −3.75 W m^{-2}, respectively. These estimates are several times larger than anthropogenic aerosol forcing estimated from models (which compare present day to preindustrial radiative effects) (Myhre et al., 2013), which are 0.75 W m^{-2} for F_{ATM} and −1.02 W m^{-2} for F_{SFC}. Some of this difference is related to comparing a DRE to a direct radiative forcing, as the latter will have smaller values since the effect of preindustrial aerosols is removed. The former, however, quantifies the DRE of all present-day aerosols, and will therefore be larger. However, since we are focused on fine-mode aerosol without dust and salt (which are mostly anthropogenic), this effect is likely small. Despite this disparity between definitions, semi-empirical fine-mode aerosol direct effect without dust and sea salt still contains considerable F_{ATM} (and F_{SFC}). This difference is consistent with model underestimation of absorbing aerosol, including black carbon optical properties and emissions, as well as omission of absorbing brown carbon (Ramanathan & Carmichael, 2008; Koch et al., 2009; C. E. Chung et al., 2012; Bond et al., 2013; Cohen & Wang, 2014; Myhre & Samset, 2015). Figure 1 shows large atmospheric heating over several regions, including southeast Asia and India due to fossil fuel and biofuel combustion, as well central Africa due to biomass burning (box in Fig. 1).

Figure 1 also shows the vertical profile of the global mean atmospheric heating rate, as well as that for the Africa region (boxed region in Fig 1a), defined as 15°W-30°E and 20°S to 10°N. The global profile peaks in the lower-troposphere, near 900 hPa, and then decays to zero near 450 hPa. Although aerosol simulations generally reproduce a similar spatial distribution of F_{SFC} and F_{ATM}, their vertical aerosol heating profile is more uniform, with relatively large heating that extends through the upper troposphere (Stjern et al., 2017; Allen et al., 2019). Atmospheric heating is quite large over the Africa region (2-4x larger than the global mean), implying large solar absorption due to biomass burning aerosol. The profile is elevated relative to the global mean profile, peaking around 700 hPa and then rapidly decaying to zero near 450 hPa. Several recent field campaigns have focused on improved understanding of absorbing aerosol off the coast of southern Africa, including Observations of Aerosols above Clouds and their interactions (ORACLES) (Zuidema et al., 2016) and Layered Atlantic Smoke Interactions with Clouds (LASIC) (Zuidema et al., 2018). The vertical heating profile in Fig. 1 is consistent with these surface and aircraft lidar observations, with smoke transport over the southeastern Atlantic mainly occurring between 2-4 km (800-600 hPa) (Mallet et al., 2019; Pistone et al., 2019).

The global annual mean top-of-the-atmosphere (TOA) aerosol DRE is −0.11 W m^{-2}, which is within the IPCC uncertainty range for aerosol direct forcing at -0.35 ± 0.5 Wm^{-2} (Boucher et al., 2013). We reiterate that this is an "aerosol direct radiative effect", and represents the present day direct aerosol radiative effects (no comparison to preindustrial aerosol direct radiative effects). Black carbon (the main warming aerosol) as well as sulfate and nitrate aerosol are known to be more anthropogenic than organic aerosol (Bond et al., 2013). If the anthropogenic fraction of black carbon is similar to that of nitrate and sulfate aerosol, the aerosol direct radiative forcing becomes less negative than the aerosol radiative effect of -0.11 W m^{-2} (C. E. Chung et al., 2016).

Several regions exhibit a positive net TOA aerosol direct effect, including much of the African continent and the tropical southeast Atlantic Ocean. Over the Africa region, we estimate a relatively large annual mean positive TOA direct radiative effect of 3.1 W m^{-2}. Tosca et al. (2013) scaled (i.e., increased) CAM5's AOD to match satellite observations, and estimate a biomass burning aerosol direct radiative effect near south Africa of about 4-5 W m^{-2}, which is similar to our value. Over a similar region, however, AeroCom models yield an August through September (when south African biomass burning emissions are largest) aerosol direct forcing of -0.03 W m^{-2}, but with a large range from -1.16 to 1.62 W m^{-2}(Stier et al., 2013; Zuidema et al., 2016). Our corresponding aerosol effect remains larger than model estimates, at 4.9 W m^{-2}. As previously noted, however, models may underestimate aerosol absorption, including biomass burning aerosol (Shindell et al., 2013).

Based on satellite observations, Feng and Christopher (2015) estimate a southeastern Atlantic averaged instantaneous direct radiative effect of $\sim$37 W m^{-2} for August 2006. A significant positive DRE is also estimated from several other studies, including de Graaf et al. (2012, 2014) who estimate an August 2006 DRE of $\sim$23 W m^{-2} near the southern African coast. More recently, Mallet et al. (2019) simulate a positive September 2016 TOA direct radiative effect of about 6 W m^{-2} over the southeastern Atlantic. This positive DRE is due, in part, to the predominance of marine stratocumulus clouds in the southeast Atlantic and the elevated atmospheric heating profile, which enhances absorption of solar radiation by absorbing aerosol above the cloud layer (Chand et al., 2009; Jiang et al., 2016). These studies illustrate the large absorption of solar radiation due to biomass burning aerosol off the coast of southeastern Africa.

Although we use semi-empirical aerosol direct radiative effect without dust and salt in an attempt to reduce model uncertainties associated with bottom-up approaches, our methodology has several caveats. This includes the observed aerosol optical depth and reliance on simulated optical properties, as well as uncertainty related to the discrimination between fine and coarse mode aerosol. We note that in reality, biomass burning can produce coarse-mode aerosol, but we have not analyzed coarse mode aerosol in this work. Additional caveats include lack of consistency between the aerosol radiative effect and simulated meteorology. For example, Randles et al. (2013) found that removing the feedback of meteorology on aerosol distributions can significantly impact the response depending on the parameter, region, and season considered. The largest effect of removing coupling is to enhance the aerosol optical depth globally over the oceans. We also explicitly acknowledge that our approach does not account for precipitation-aerosol interactions. As shown in Allen and Landuyt (2014) enhanced convection is associated with more convective precipitation, enhanced wet removal, and less BC below 500 hPa. However, more convective mass flux, particularly above 500 hPa, yields more BC aloft due to enhanced convective lofting. Although this result is based on idealized simulations with CAM5, similar conclusions were found using observations and reanalysis data (Park & Allen, 2015). Thus, although enhanced convection may reduce aerosol below 500 hPa (due to enhanced wet removal), it may increase it above 500 hPa (due to enhanced convective lofting).

2.2 Community Earth System Model

This study uses the National Center for Atmospheric Research (NCAR) Community Earth System Model (CESM) version 1.2.2.1. To help evaluate the robustness of the climate response, we use different versions of CESM's atmosphere model, including version 4 (CAM4) (Neale, Richter, et al., 2010) and version 5 (CAM5) (Neale, Gettelman, et al., 2010). Ideally, to better evaluate the robustness of the response, multiple climate models from different organizations should be used. Both CAM4 and CAM5 have a horizontal resolution of 1.9°x2.5°; CAM4 has 25 vertical layers and CAM5 has 30. Their main shared physical parameterization is the Zhang-McFarlane deep convection scheme (bulk mass flux with CAPE closure) (Zhang & McFarlane, 1995). CAM4 uses a shallow convection scheme that involves three-level adjustment of moist static energy (Hack, 1994) and a prognostic single-moment microphysics scheme, including diagnostic cloud fraction (Rasch & Kristjánsson, 1998). CAM5 uses a mass flux scheme with convective inhibition closure for shallow convection (Park & Bretherton, 2009) and a prognostic double moment microphysics scheme (Morrison & Gettelman, 2008) with ice supersaturation (Gettelman et al., 2010) and a diagnostic cloud fraction scheme for cloud microphysics and macrophysics. These two models also have different radiative transfer schemes. The rapid radiative transfer model (RRTMG) provides the radiative transfer calculations in CAM5, which is an accelerated and modified version of the correlated k-distribution model, RRTM (Mlawer et al., 1997; Clough et al., 2005; Iacono et al., 2008). The calculation of shortwave radiation in CAM4 is based on a δ-Eddington approximation (Joseph et al., 1976; Coakley et al., 1983; Briegleb, 1992). All CESM simulations use the Parallel Ocean Program version 2 (POP2) ocean model, which is based on the POP version 2.1 from the Los Alamos National Laboratory (R. Smith et al., 2010)

2.3 CESM Experimental Design

We conduct CESM experiments with the fully coupled atmosphere-ocean configuration (CAM4-coupled and CAM5-coupled; Table 1). These simulations are initialized using 1850 preindustrial forcings (e.g., greenhouse gases) and boundary conditions, as well as a previously spun-up preindustrial ocean, and are integrated for 100 years. Output from last 50 years is used for our analyses, when the models have reached near-equilibrium. The choice of conducting 100 year simulations, and analyzing the last 50 years, is justified based on the fact no significant trend in TOA net radiation exists over the last 50 years (implying the model has reached near-equilibrium). Furthermore, we initially conducted a few of our coupled ocean-atmosphere simulations over a longer time period−150 years, as opposed to the 100 years we have settled on. Similar responses exist over years 50-99, as well as from years 100-149 (not shown). Thus, we believe our simulations have reached near-equilibrium in years 50-99.

Fixed SST (fSST) simulations are also conducted (CAM4-fSST and CAM5-fSST; Table 1), where the model is driven by a repeating monthly climatology of SSTs. These CAM4/5-fSST simulations are integrated for 20 years, the last 15 of which is used for our analyses.

Monthly semi-empirical fine mode aerosols without dust and sea salt (atmospheric heating rate and surface solar radiation reduction) from C. E. Chung et al. (2016) (see also Section 2.1) are interpolated to CESM's horizontal resolution and incorporated into its radiation module. The atmospheric heating rate is vertically interpolated to each model's hybrid pressure levels. Although the aerosol direct effect is almost independent of solar zenith angle (θ) when the angle is small, the aerosol direct effect approaches zero as θ approaches 90°. Thus, the added aerosol radiative effect is multiplied by a scaling factor that depends on zenith angle(C. E. Chung, 2006). The climate response is estimated as the difference between the simulation with semi-empirical fine mode aerosols without dust and sea salt, and a corresponding control run that lacks observationally constrained fine mode aerosol direct radiative effects without dust and sea salt.

Simulations are conducted with both the CAM4 and CAM5 atmosphere model. In the case of the CAM4 model, which only includes aerosol direct effects, the radiative effects of the default aerosols are neglected by removing them from the list of radiatively active species. With CAM5, which includes both direct and indirect aerosol effects, the radiative effects of the default aerosols cannot be simply neglected, as cloud microphysical processes depend upon aerosols. Thus, CAM5 simulations use prescribed (as opposed to prognostic) modal aerosols (MAM3). Although this represents a double counting of aerosol effects in the observationally-constrained CAM5 simulation, we have verified that the response eliminates the bulk of the radiative effects due to the default prescribed aerosols (which will be similar in observationally constrained and control simulations). For example, the percent change in the burden of each aerosol species is <1%. These changes are not identical to zero because the prescribed CAM5 modal aerosol implementation does not use mixing ratio values that have been time interpolated from monthly mean values. Instead, the mixing ratio values are obtained by random sampling of the time interpolated log normal distribution of each prescribed species.

In addition to conducting coupled ocean-atmosphere simulations with global semi-empirical fine mode aerosol direct radiative effect without dust and sea salt, we also conduct analogous simulations, but driven by semi-empirical fine mode aerosol direct radiative effects without dust and sea salt over the Africa region alone (box in Fig. 1a; CAM4-coupled Africa and CAM5-coupled Africa). This is accomplished by setting the reduction in surface solar radiation and atmospheric solar heating to zero outside the Africa region. These experiments ("CAM4/5-coupled Africa") allow us to isolate the role of African aerosol−which is primarily biomass burning aerosol−in driving the La Niña-like teleconnection. Moreover, to address the dependency of our results to the relatively large amount of atmospheric heating in our semi-empirical fine mode aerosol direct radiative effect, we conduct analogous CAM4-coupled Africa sensitivity experiments driven by 50 and 20% of the semi-empirical aerosol direct radiative effect over the Africa region (CAM4-coupled Africa 50% and CAM4-coupled Africa 20%, respectively). As in the default Africa simulations, the direct aerosol radiative effect is set to zero outside the Africa region. Thus, these reduced aerosol radiative effect simulations feature 50 and 20% of the reduction in surface solar radiation and atmospheric solar heating over the Africa region. This decreases the corresponding August through September TOA direct aerosol radiative effect from 4.9 W m^{-2} to 2.5 and 0.98 W m^{-2}, respectively. The latter value is within the range of AeroCom model estimates of aerosol forcing (−1.16 to 1.62 W m^{-2}) (Stier et al., 2013; Zuidema et al., 2016). Moreover, the vertical profile of the atmospheric heating rate scaled by 20% and 50% over the Africa region shows better correspondence with that simulated from CMIP6 2xFIRE experiments (Fig. 1d; Section 2.4).

Finally, we also conduct CAM5 coupled simulations using prognostic aerosols (MAM3), which feature a doubling of 1850 black carbon fire emissions over the Africa region (CAM5-2xAFBC). These simulations are compared to an analogous control simulation that lacks a doubling of 1850 BC fire emissions over the Africa region. These simulations include aerosol indirect effects, as well as aerosol-meteorology coupling. CAM5-2xAFBC yields a vertical profile of atmospheric heating similar to that obtained in CMIP6 2xFIRE experiments (Fig. 1d).

2.4 Coupled Model Intercomparison Project version 6 Models

To complement our CESM simulations, we also analyze Coupled Model Intercomparison Project version 6 (CMIP6) simulations from the Aerosol Chemistry Model Intercomparison Project (AerChemMIP) (Collins et al., 2017). Specifically, we analyze the difference between two fixed SST simulations. The control simulation ("piClim-control") features fixed preindustrial aerosol emissions and precursor gases. The experiment ("piClim-2xfire") is identical, but biomass burning/fire emissions including NO_x, BC, OC, CO, and VOCs are doubled. Three models are available including CNRM-ESM2-1, MIROC6, and UKESM1-0-LL. Both CNRM-ESM2-1 and MIROC6 have 30 simulation years and UKESM1-0-LL has 45 simulation years. As these are fixed SST experiments, they only yield the "rapid adjustments", and not the full climate response. The difference between the CMIP6 experiment and control simulations is referred to as "2xFIRE".

CMIP6 2xFIRE simulations allow us to evaluate the impact of biomass burning aerosol in non-CESM models, and therefore allow determination of how robust our CESM results are. We also note that these CMIP6 simulations include aerosol-meteorology coupling, aerosol indirect effects, and potential feedbacks between atmospheric circulation and fire aerosol emissions. We reiterate that these CMIP6 simulations are fixed SSTs, and thus are not expected to capture the African biomass aerosol teleconnection to the tropical Pacific (since atmosphere-ocean coupling and resulting feedbacks are not present). Nonetheless, they allow us to quantify the local atmospheric response (in the Atlantic) to African biomass aerosol in models with different parameterizations and with a more realistic representation of aerosol processes, including meteorological feedbacks.

This Atlantic response−including anomalous ascent and upper level divergence−represents the first step in our proposed African biomass burning aerosol teleconnection to the tropical Pacific. As will be discussed below, CMIP6 2xFIRE simulations generally yield (2 of 3 models) a similar atmospheric response in the Atlantic as compared to CESM driven by semi-empirical fine-mode aerosol direct radiative effects without dust and sea salt (including our CAM4- and CAM5-fSST experiments). CMIP6 2xFIRE results therefore support our conclusions with CESM.

2.5 Observations

We use 1997-2018 0.25°x0.25° biomass burning emissions from the Global Fire Emissions Database (GFED) version 4s (van der Werf et al., 2017) (2017 and 2018 are preliminary data). GFED4s uses satellite information on fire activity, including MODIS and the Visible and Infrared Scanner (VIRS), and vegetation productivity to estimate gridded monthly fire emissions. The modeling system is based on the Carnegie-Ames-Stanford Approach (CASA) biogeochemical model (Potter et al., 1993), which has several modifications from the previous version and uses higher quality input datasets. Several significant upgrades exist in GFED4s, including new burned area estimates with contributions from small fires and a revised fuel consumption parameterization optimized with field observations. We also use the 1750-2015 CMIP6 reconstructed biomass burning emission estimates, which merges the satellite record with several existing proxies, and uses the average of six models from the Fire Model Intercomparison Project (FireMIP) protocol to estimate emissions (van Marle et al., 2017). GFED4s is used as an anchor point for all proxies and model results from 1997-2015.

Observed SST data comes from the Kaplan SST data set (Kaplan et al., 1998), which is derived from the United Kingdom Met Office SST data and uses statistical techniques to fill data gaps. SST data is on a 5°x5° grid and consists of monthly anomalies from 1856-present. Anomalies are based on the 1951-1980 time period. We use observed precipitation data rom the Global Historical Climatological Network (GHCN) version 2 (Peterson & Vose, 1997), which is based on over 20,000 stations worldwide that have been quality controlled and bias corrected. ENSO is characterized by the Southern Oscillation Index (SOI), which is a standardized index based on the observed sea level pressure differences between Tahiti and Darwin, Australia (Trenberth & Caron, 2000). The negative phase of the SOI represents below-normal air pressure at Tahiti and above-normal air pressure at Darwin (i.e., El Niño). Positive (negative) SOI values are indicative of La Niña (El Niño).

Dynamical variables (e.g., winds) come from the Modern-Era Retrospective analysis for Research and Applications version 2 (MERRA2) (Gelaro et al., 2017). MERRA2 spans 1980 to present and is available at several spatial resolutions. We download the 0.625°x0.5° resolution and bilinearly interpolate to a 5°x5° resolution. MERRA2 assimilates observation types not available to its predecessor (e.g., GPS data), and includes updates to the Goddard Earth Observing System (GEOS) model and analysis scheme. Additional advances in MERRA2 are the assimilation of aerosol observations (Randles et al., 2017), several improvements to the representation of the stratosphere including ozone, improved representations of the cryosphere, and the reduction of some spurious trends and jumps related to changes in the observing system.

3 Results

3.1 Fully coupled CESM simulations

3.1.1 Surface Temperature and Precipitation

Figure 2 shows the global annual mean surface temperature response to semi-empirical fine mode aerosol direct radiative effect without dust and salt for CAM4- and CAM5-coupled simulations. The global annual mean change in surface temperature is 0.28 K for CAM4-coupled and 0.39 K for CAM5-coupled, both significant at the 99% confidence level. Thus, unlike most aerosol simulations (Wilcox et al., 2013; Rotstayn, Collier, Shindell, & Boucher, 2015), our semi-empirical fine-mode aerosol direct radiative effect leads to surface warming, consistent with the relatively large amount of atmospheric heating (Fig. 1). We also reiterate that our aerosol radiative effect lacks aerosol indirect effects, which likely cool the climate system with a RF of -0.45 (-1.2 to 0.0) W m^{-2} (Myhre et al., 2013). Most of the warming occurs in the Arctic, consistent with high-latitude warming amplification due to ice-albedo feedbacks (Stjern et al., 2019). CAM5-coupled, however, also shows considerable warming over much of the global ocean. A notable lack of warming occurs over much of Asia, with cooling near India and China. Moreover, both models show an Atlantic Meridional Mode (AMM) (Chiang & Vimont, 2004) like SST pattern (negative polarity) in the tropical Atlantic, with cooling of the north tropical Atlantic, and warming of the south tropical Atlantic (particularly along the west African coast near the Gulf of Guinea). CAM4-coupled also yields cooling throughout the central and eastern tropical Pacific, which resembles a La Niña-like SST pattern. Although CAM5-coupled does not show this cooling, there is a noticeable lack of significant warming in the eastern tropical Pacific.

Figure 2 also shows the global annual mean precipitation response. The global annual mean change in precipitation is -0.037 mm day^{-1} for CAM4-coupled and -0.024 mm day^{-1} for CAM5-coupled, both significant at the 90% confidence level. Although a decrease in global mean precipitation in response to aerosols is similar to prior studies (Ramanathan et al., 2001; Liepert et al., 2004; Wilcox et al., 2013; Samset et al., 2016), this decrease is interesting in light of the global mean surface warming. As our semi-empirical aerosol direct radiative effect has a relatively large amount of atmospheric heating, several analyses have shown that the precipitation response to absorbing aerosol depends on its vertical profile. Precipitation generally increases when absorbing aerosol is located closer to the surface, but decreases when it is located higher in the atmosphere (Ming et al., 2010; Zarzycki & Bond, 2010; Ban-Weiss et al., 2012; Pendergrass & Hartmann, 2012). Similar to the temperature dipole pattern in the tropical Atlantic, a similar pattern exists for precipitation, where positive (negative) temperature responses correspond to positive (negative) precipitation responses. Moreover, both models show a significant precipitation decrease in the central and eastern tropical Pacific, with weaker precipitation increases in the western tropical Pacific. This tropical Pacific precipitation response is again La Niña-like, and is most pronounced in CAM4-coupled.

3.1.2 Atmospheric Dynamics

Figure 3 shows the annual mean sea level pressure (SLP) and surface wind response for both models. Anomalous low pressure occurs in the southeastern tropical Atlantic in both models, with anomalous high pressure in the northwestern tropical Atlantic. Consistent with these SLP responses, the surface wind response features a northwesterly/westerly flow in the north tropical Atlantic that cuts across the equator and converges near the Gulf of Guinea (where the decrease in SLP exists). Similar to the AMM, the strengthened northeast trade winds likely promote cooling of the north tropical Atlantic SSTs through the wind-evaporation-SST (WES) feedback (Chiang & Vimont, 2004). The SST warming near the Gulf of Guinea is consistent with the positive net aerosol direct radiative effect (Fig. 1).

The large amount of aerosol atmospheric heating off the west coast of Africa destabilizes the atmosphere and leads to anomalous upper level (200 hPa) ascent and divergence (Fig. 3). This corresponds to the decrease in SLP, and the increase in precipitation and cloud cover near the Gulf of Guinea. Similar results are obtained with the surface and 200 hPa velocity potential (Supplementary Figure 1), with both models showing surface convergence near the west coast of Africa and divergence aloft. The rising air off the west African coast reinforces the rising branch of the tropical Atlantic Walker circulation near Africa (Figure 4).

The enhanced rising motion is compensated by sinking motion in several regions, including off-equatorial descent in the Atlantic near 30N/S. Stronger sinking motion occurs along the equator, near the western tropical Atlantic (near Brazil) and in the eastern tropical Pacific, which reinforces the sinking branch of the tropical Pacific Walker circulation (near 120W; Fig. 4). Tropical Pacific easterly trade winds at the surface are also enhanced (Fig. 3). Surface air converges in the western tropical Pacific (Supplementary Figure 1), which is associated with enhanced ascent near the ascending branch of the tropical Pacific Walker circulation (near 140E; Fig. 4), particularly in CAM4-coupled. Similar results are obtained with the surface and 200 hPa velocity potential (Supplementary Figure 1), with upper level (surface) convergence (divergence) over the eastern tropical Pacific. The Bjerknes positive feedback, in which the the easterly surface wind stress enhances the zonal SST gradient across the tropical Pacific, acts to amplify these wind and SST anomalies, resulting in intensification of the tropical Pacific Walker circulation and the development of a La Niña-like response. Consistent with these changes in the tropical Pacific Walker circulation, precipitation is reduced (enhanced) over the eastern/central (western) tropical Pacific (Fig. 2). Moreover, a tropical Pacific Rossby wave response occurs in both models (Supplementary Figure 2), with counterclockwise (clockwise) rotation in the Northern (Southern) Hemisphere eastern tropical Pacific (a Rossby wave response of opposite orientation also exists in the tropical Atlantic).

These responses are very similar to the Atlantic Niño teleconnection to the tropical Pacific (Keenlyside & Latif, 2007; Rodríguez-Fonseca et al., 2009; Ding et al., 2012; Frauen & Dommenget, 2012; Keenlyside et al., 2013). Atlantic Niño strengthens the Walker circulation, including the ascending branch over the Atlantic and the descending branch over the central Pacific (Wang et al., 2009; Ding et al., 2012; Martín-Rey et al., 2012; Kucharski et al., 2016). On longer time scales, recent warming of Atlantic SSTs has also been shown to yield a similar teleconnection to the Pacific, including intensification of the Pacific trade winds (England et al., 2014) and Walker circulation, and eastern Pacific SST cooling (Kucharski et al., 2011; McGregor et al., 2014; X. Li et al., 2012).

3.1.3 Ocean Response

A La Niña-like subsurface response also exists in the ocean for both models, with a stronger response in CAM4-coupled. Consistent with the surface wind response, westward (eastward) equatorial oceanic zonal current anomalies exist throughout the upper Pacific ocean (∼100 m depth) westward (eastward) of ∼220E (Supplementary Figure 3). The enhanced westward flow enhances the climatological equatorial surface current. Eastward oceanic zonal current anomalies exist deeper in the ocean, which again represents strengthening of the climatological subsurface zonal current (the Equatorial Undercurrent). These changes are reminiscent of a La Niña like response. The cross section of the equatorial potential temperature in the Pacific also shows western tropical Pacific ocean warming down to ∼300 m, and cooling in the eastern tropical Pacific (Supplementary Figure 3). These changes are consistent with the wind stress anomalies, and represent an increase the east-west thermocline slope, with deepening in the west and shoaling in the east. The shallower thermocline in the east promotes SST cooling, and cooler SST anomalies further produce more westward wind stress, reinforcing these wind and temperature responses.

3.2 Fixed sea surface temperature simulations

We also conduct analogous experiments but with fixed sea surface temperatures (fSST), which uses a repeating cycle of monthly climatological SSTs (CAM4-fSST and CAM5-fSST). These simulations also feature a repeating cycle of monthly climatological sea ice. These simulations lack ocean-atmosphere coupling, and only represent the "rapid adjustment" to semi-empirical fine-mode aerosol direct radiative effect without dust and sea salt. Consistent with fixed SSTs, much smaller changes in surface temperature occur (Supplementary Figure 4). Continents generally cool, particularly regions with strong aerosol direct radiative effect (Fig. 1), including central Africa and southeast Asia. The Arctic warms as before, but this warming is much weaker, consistent with the lack of ice-albedo feedbacks (and fixed SSTs). Also similar to, but weaker than the coupled simulations, is an increase in precipitation off the west coast of Africa. Precipitation decreases also occur in the western tropical Atlantic (near Brazil) and in the Indian Ocean (stronger than in the coupled simulations). However, a negligible precipitation response exists in the tropical Pacific.

Figure 5 shows the the dynamical response in the fSST simulations. Similar dynamical changes between the coupled and fSST simulations occur in the Atlantic, but they are again weaker in fSST simulations. This includes the surface convergence and upper level divergence off the coast of western Africa (see also Supplementary Figure 5), as well as the related ascent. Negligible dynamical responses occur in the tropical Pacific. This includes the 200 hPa convergence (divergence) over the eastern (western) tropical Pacific and the associated changes in vertical velocity (i.e., Walker circulation). CAM4-fSST, however, continues to show a stronger signal than CAM5-fSST. Thus, the fSST simulations capture the dynamical response in the tropical Atlantic, but it is weaker than in the coupled simulations. The teleconnection to the Pacific, however, is negligible in fSST simulations. Although this may be related to the weaker response in the Atlantic, it is likely mostly due to the lack of ocean-atmosphere coupling.

3.3 Fully coupled simulations for Africa

We also conduct experiments with the fully coupled atmosphere-ocean configuration, but forced with semi-empirical fine-mode aerosol direct radiative effect without dust and salt over the Africa region alone (CAM4-coupled Africa and CAM5-coupled Africa). The Africa region is defined as 15°W-30°E and 20°S to 10°N (box in Fig. 1a). The results are very similar to the fully coupled simulations driven by the global semi-empirical aerosol direct radiative effect, particularly in the tropics. Figure 6 shows the temperature and precipitation responses for the Africa-only aerosol direct radiative effect simulations in CAM4 and CAM5. We note that CAM4-coupled Africa yields a surprisingly large amount of Arctic warming, particularly in the north Atlantic, despite no direct forcing in this region. Why specifically the Arctic warms is beyond the scope of this study, but it might be related to changes in ocean heat transport, related to the Atlantic Meridional Overturning Circulation. Warming of the Arctic is not necessarily unexpected, as localized forcing can have significant remote impacts on climate. Specifically, the Arctic may be particularly sensitivity to remote aerosol emissions (Shindell & Faluvegi, 2009; Acosta Navarro et al., 2016; Lewinschal et al., 2019; Westervelt et al., 2019).

Similar to the global simulations, a similar AMM-like pattern exists in the tropical Atlantic. More importantly, a La Niña-like tropical Pacific SST response exists, particularly in CAM4-coupled Africa. The tropical precipitation response is also similar to the global aerosol simulations, including increased precipitation off the coast of western Africa and decreased precipitation in the western tropical Atlantic (near Brazil). There are also La Niña-like decreases (increases) in central/eastern (western) tropical Pacific precipitation, particularly in CAM4-coupled Africa.

The dynamical responses in the Atlantic are also reproduced in the Africa-only aerosol simulations (Figure 7). This includes surface (upper level) convergence (divergence) off the coast of western Africa, as well as anomalous ascent and sea level pressure reductions, including similar surface wind responses (see also Supplementary Figure 6). The tropical Atlantic Walker circulation is again strengthened, as is the corresponding Pacific Walker circulation (Figure 8) including enhanced descent (ascent) in the central/eastern (western) tropical Pacific. Furthermore, a tropical Pacific Rossby wave response occurs (Supplementary Figure 7). The subsurface ocean response is also similar to the global aerosol simulations (Supplementary Figure 8). Thus, Africa aerosol only simulations reproduce the tropical response, including the teleconnection to the tropical Pacific. These simulations confirm that atmospheric aerosol over Africa—which is mostly due to biomass burning—can drive a teleconnection between the tropical Atlantic and Pacific, resulting in a La Niña-like response in the tropical Pacific.

To address the dependency of our results to the relatively large amount of atmospheric heating in our semi-empirical fine mode aerosol direct radiative effect, we conduct analogous CAM4 Africa sensitivity tests driven by 20% and 50% of the semi-empirical aerosol direct radiative effect over the Africa region (Fig. 1d; CAM4-coupled Africa 20% and CAM4-coupled Africa 50%, respectively). As in CAM4-coupled Africa, the direct aerosol radiative effect is set to zero outside the Africa region. These simulations show a similar, but weaker response, including significant anomalous ascent and upper level divergence off the coast of west Africa, strengthening of the Walker circulation, and a La Niña-like teleconnection to the tropical Pacific (Figures 9-10). Thus, our results are not dependent on the relatively large amount of atmospheric heating in our semi-empirical fine mode aerosol direct radiative effect.

Figure 11 shows the most important dynamical responses in our CAM5 coupled simulation using prognostic aerosols (MAM3), which features a doubling of 1850 black carbon fire emissions over the Africa region (CAM5-2xAFBC). CAM5-2xAFBC also includes aerosol indirect effects, as well as aerosol-meteorology coupling. Similar to the above simulations with semi-empirical aerosol radiative effects, CAM5-2xAFBC shows an increase in upper-level ascent and divergence, as well as precipitation, off the west coast of Africa. Furthermore, in the tropical Pacific, CAM5-2xAFBC shows a La-Niña-like response, including decreased (increased) precipitation in the central/eastern (western) tropical Pacific. The corresponding upper-level vertical velocity and divergence responses are also consistent, including anomalous descent (ascent) in the central/eastern (western) tropical Pacific. Thus, CAM5-2xAFBC supports our conclusions, including the dynamical response to Africa biomass aerosols in the Atlantic, and the teleconnection to the tropical Pacific.

3.4 CMIP6 2xFIRE simulations

Unfortunately, most CMIP6 models lack the relevant diagnostics to calculate the 2xFIRE TOA RF. The lone model that included these diagnostics, CNRM-ESM2-1, yields an annual (August-September) 2xFIRE TOA RF over our Africa region (box in Fig. 1a) of -0.61 (-0.80) W m^{-2}. The August-September value is on the low end of AeroCom models, but falls within the AeroCom range of -1.16 to 1.62 W m^{-2}. Models archived the solar heating rate diagnostic, which shows the structure of the CMIP6 2xFIRE vertical heating profile over the Africa region resembles our semi-empirical heating (e.g., maximum near 700 hPa; Fig. 1), but it is weaker in magnitude, particularly in CNRM-ESM2-1 and MIROC6, where it peaks at ∼0.07 K day^{-1} (versus our 0.44 K day^{-1}). UKESM1-0-LL shows much larger heating over the Africa region, peaking at ∼0.18 K day^{-1}, and in better agreement to semi-empirical fine mode aerosol direct heating (but still about 50% as large). We note, however, that the CMIP6 2xFIRE heating profiles over the Africa region are similar to our sensitivity tests with 20% (for CNRM-ESM2-1 and MIROC6) and 50% (for UKESM1-0-LL) of the semi-empirical fine mode aerosol direct radiative effect (Fig. 1d). The large CMIP6 intermodel spread in biomass-induced heating over the Africa region also reinforces the notion that significant uncertainty remains in bottom-up model simulations of biomass burning.

We focus on the annual mean change in aerosol optical depth (AOD) and absorption aerosol optical depth (AAOD) at 550 nm. CMIP6 2xFIRE simulations shows large increases in both quantities over much of the African continent, including the tropical Atlantic ocean (Supplementary Figure 9). Averaged over our Africa region (box in Fig. 1a), AOD (AAOD) increases by 0.04, 0.09 and 0.14 (0.0037, 0.0048, and 0.025) for CNRM-ESM2-1, MIROC6 and UKESM1-0-LL, respectively. Thus, even with similar fire emission perturbations, CMIP6 models exhibit a large range in AOD and in particular, AAOD response. This further illustrates the large uncertainty in bottom-up aerosol simulations.

In response to doubling fire emissions, two of the three models show a response off the coast of Africa that resembles our CESM simulations. This includes anomalous ascent and upper level divergence, increased cloud cover and precipitation, and decreased sea level pressure near the Gulf of Guinea (Fig. 12; Supplementary Figure 10). UKESM1-0-LL shows the largest response, which is consistent with the larger increase in AOD and in particular, AAOD and associated atmospheric heating. Reasons for the lack of a response in MIROC6 are unclear. Interestingly, despite the relatively large negative TOA RF over the Africa region, CNRM-ESM2-1 simulates the responses off the coast of Africa (albeit weaker than in our fSST simulations). This suggests the atmospheric heating and its vertical location are likely the more important factors in driving the Atlantic climate responses. With considerably less atmospheric heating over the Africa region, relative to semi-empirical aerosol direct radiative effect, this suggests the Africa climate response occurs with substantially less heating than exists in our semi-empirical aerosol simulations (consistent with CAM4-coupled Africa 50% and 20%, as well as CAM5-2xAFBC).

We note that CMIP6 2xFIRE simulations, like our fSST simulations, do not yield a strong teleconnection to the tropical Pacific, implying the importance of surface temperature changes and atmosphere-ocean coupling to this teleconnection. Thus, our CESM simulations, as well as CMIP6 2xFIRE experiments, support the possible role of African biomass burning emissions in initiating the first stage of the teleconnection, including increased ascent and upper level divergence near the Gulf of Guinea (i.e., intensified Atlantic Walker circulation).

3.5 Observations

Observations also support a relationship between south African biomass burning and ENSO, particularly during boreal fall (September, October, November, SON). As the largest emitter of biomass burning aerosols, southern Africa contributes ∼30% of global biomass burning aerosol by mass (van der Werf et al., 2010). From July though October, these aerosols are transported by the atmospheric circulation over the southeastern Atlantic Ocean (Adebiyi & Zuidema, 2016).

Here, we focus on the 22-year time period from 1997-2018, when satellite estimates of biomass burning emissions exist. The (detrended) SON correlation between GFED4s south African biomass burning emissions and the SOI is 0.66 (significant at the 99% confidence level). This indicates high (low) SON south African fire years are associated with

La Niña (El Niño). Figure 13 shows the corresponding spatial correlations between Kaplan SSTs and south African biomass burning emissions. High south African biomass burning emissions are associated with a La Niña-like SST pattern in the tropical Pacific, with colder (warmer) SSTs in the central and eastern (western) tropical Pacific. Although weaker, this relationship (particularly the cooling in the central/eastern tropical Pacific) exists over a longer time period. This is illustrated using CMIP6 reconstructed south African biomass burning emissions and Kaplan SSTs from 1950-2015 (Fig. 13). We note that correlations between north African biomass burning and the SOI are weaker and not significant (e.g., SON correlation of 0.26). During December-February, which corresponds to the season of maximum north African biomass burning emissions, the correlation is also non-significant (and negative) at -0.13.

A lead-lag (detrended) correlation analysis suggests that ENSO is the causality of the south African biomass burning-La Niña relationship. Generally, ENSO conditions start to develop between March through June, reaching peak intensity during December-April (Deser et al., 2010). The 1997-2018 correlation between MAM SOI and SON south African biomass burning emissions from GFED4s is 0.39. Using JJA SOI and SON south African biomass burning emissions, this correlation increases to 0.64. Thus, La Niña (El Niño) conditions tend to precede large (small) south African biomass burning emissions in SON. This is presumably due to decreased precipitation and drying, as a negative correlation exists between both JJA and SON SOI and SON south African GHCN precipitation at -0.38 and -0.33, respectively (the former correlation is significant at the 90% confidence level). However, precipitation and burned area relations are complex, as enhanced precipitation can increase burned area through increased productivity (more fuel available for burning), or limit burned area by shortening the dry season (van der Werf et al., 2008). Nonetheless, this result is consistent with Andela and van der Werf (2014), who showed that much of the upward trend in south African biomass burning from 2001-2012 was driven by the El Niño to La Niña transition.

Although ENSO appears to initiate this relationship, there could be a positive feedback whereby high south African biomass burning emissions trigger the model simulated dynamical response off the coast of west Africa, further promoting the development of La Niña. This is illustrated with a composite analysis, which is based on the difference of the three highest south African biomass burning SON years minus the three lowest south African biomass burning SON years. Not surprisingly, the three highest (lowest) south African biomass burning SON years usually correspond to moderate to strong La Niña (El Niño) events in 2010, 2011 and 2008 (2002, 2013, 1997). The choice of three highest and three lowest south African biomass burning years corresponds to $\pm$ 1-standard deviation from the 1997-2018 mean GFED4s south African biomass burning emissions. Figure 14 shows that high south African SON fire years (relative to low SON fire years) feature an increase in upper-level divergence and vertical velocity, precipitation, cloud cover, and decreases in sea-level pressure in the Gulf of Guinea. Similar results exist based on raw observations, including decreased Hadley Centre SLP (Allan & Ansell, 2006) and High Resolution Infrared Radiation Sounder (HIRS) outgoing longwave radiation (H.-T. Lee et al., 2007) and increased Global Precipitation Climatology Project (GPCP) precipitation (Adler et al., 2003) near the Gulf of Guinea (Supplementary Figure 11). A similar but weaker signal exists if we analyze the high fire SON years only (not shown).

We have also calculated 1997-2018 SON correlations between GFED4s south African biomass burning emissions and MERRA2 atmospheric variables (Figure 15). Time series are first detrended prior to calculation of the correlation coefficient. Significance is calculated based on a t-test using the formula $t = r/[(1-r^2)/(N-2)]^{0.5}$, where r is the correlation coefficient and N is the number of years (22). This correlation analysis−which focuses on the Atlantic−shows results that are similar to our composite analysis. That is, high SON south Africa fire years are associated with an increase in upper-level divergence and vertical velocity, precipitation, and cloud cover near the Gulf of Guinea.

Although isolating a south African biomass burning and ENSO signal from observations alone is difficult, a significant relationship exists during boreal fall. Although ENSO appears to initiate (i.e., lead) changes in SON south African biomass burning emissions, with La Niña conditions preceding high SON south African biomass burning emissions, high SON south African biomass burning emissions are associated with dynamical changes off the coast of west Africa that resemble our model simulations.

Thus, we suggest high south African biomass burning emissions may feedback on the developing La Niña, further supporting its intensification. This is also supported by observations, as the SOI increases from JJA to SON in each of the three highest south African biomass burning SON years. During 2010 (the highest south African biomass burning SON fire year), the SOI increases from 1.9 in JJA to 3.2 in SON. Similarly, during 2011 (second highest south African biomass burning SON fire year), the SOI increases from 0.5 in JJA to 1.71 in SON and during 2008 (third highest south African biomass burning SON fire year), the corresponding SOI increase is from 0.69 to 2.34. Although it is not possible to attribute this La Niña intensification directly to south African biomass burning emissions, these results suggest a positive feedback may exist.

4 Discussion and Conclusion

Significant uncertainty remains in aerosol direct (and indirect) radiative effects, and in turn the impacts on the climate system. In an effort to circumvent some of the traditional uncertainties, we adopt a top-down approach by incorporating semi-empirical fine mode aerosol direct radiative effect without dust and salt into two climate models. Our results yield a robust circulation response in the tropics. In the tropical Atlantic, aerosol heating destabilizes the atmosphere and triggers enhanced ascent and upper level divergence off the coast of western Africa. This strengthens the Walker circulation, including the ascending branch over the tropical Atlantic as well as the descending branch over the tropical central Pacific. The enhanced surface divergence and easterly trade winds in the latter region shallows the equatorial thermocline, triggering coupled ocean-atmosphere processes that promote the development of a Pacific La Niña. Similar coupled ocean-atmosphere simulations with Africa-only semi-empirical aerosol direct radiative effect reproduces these responses. Thus, our simulations suggest African biomass burning is capable of remotely impacting the tropical Pacific.

These responses are very similar to the Atlantic Niño teleconnection to the tropical Pacific. Several studies have shown that Atlantic Niño variability influences ENSO, with Atlantic Niño SST variations preceding opposite signed SST anomalies in the central and eastern equatorial Pacific by 2-3 seasons (Keenlyside & Latif, 2007; Rodríguez-Fonseca et al., 2009; Ding et al., 2012; Frauen & Dommenget, 2012; Keenlyside et al., 2013). Atlantic Niño strengthens the Walker circulation, including the ascending branch over the Atlantic and the descending branch over the central Pacific (Wang et al., 2009; Ding et al., 2012; Martín-Rey et al., 2012; Kucharski et al., 2016). The sinking motion in the central/eastern tropical Pacific induces easterly surface wind anomalies just to the west (Polo et al., 2015; X. Li et al., 2012). This wind anomaly contributes to a pile up of water in the western equatorial Pacific, triggering a perturbation in the depth of the oceanic thermocline. These perturbations propagate eastward as upwelling Kelvin-waves. As the Kelvin wave propagates, the eastern Pacific becomes cooler (warmer) through thermocline feedbacks and the Bjerknes feedback (X. Li et al., 2012; Kucharski et al., 2016). On longer time scales, recent warming of Atlantic SSTs has also been shown to yield a similar teleconnection to the Pacific, including intensification of the Pacific trade winds (England et al., 2014) and Walker circulation, and eastern Pacific SST cooling (Kucharski et al., 2011; McGregor et al., 2014; X. Li et al., 2012).

Although we use semi-empirical fine-mode aerosol direct radiative effect without dust and sea salt in an attempt to reduce model uncertainties associated with bottom-up approaches (Ramanathan & Carmichael, 2008; Koch et al., 2009; Ming et al., 2010; Zarzycki & Bond, 2010; C. E. Chung et al., 2012; Ban-Weiss et al., 2012; Bond et al., 2013; Allen & Landuyt, 2014; Cohen & Wang, 2014; Myhre & Samset, 2015; Samset & Myhre, 2015)−including likely underestimation of biomass aerosol (Kaiser et al., 2012; Tosca et al., 2013; Shindell et al., 2013)−our methodology may be limited by several uncertainties. This includes the observed aerosol optical depth and reliance on simulated optical properties. Our approach also lacks aerosol-meteorology coupling. We also note that our semi-empirical fine-mode aerosol direct radiative effect contains considerable atmospheric heating, several times larger than most models (Myhre et al., 2013). However, CAM4 sensitivity tests with reduced semi-empirical fine-mode aerosol direct radiative effect over the Africa region also produces a significant (but weaker) La Niña-like teleconnection. This suggests our results are not dependent on the relatively large amount of atmospheric heating in our semi-empirical aerosol data set.

Our primary simulations (driven by semi-empirical aerosol radiative effects) consider only aerosol direct and semi-direct effects, but biomass burning aerosols entrained into the southeastern Atlantic stratocumulus (the microphysical aerosol "indirect" effect) may play a dominant role in determining the total TOA radiative forcing (Lu et al., 2018). The importance of biomass burning aerosol indirect effects is consistent with several other studies (Ward et al., 2012; Grandey et al., 2016; Jiang et al., 2016; Landry et al., 2017). In Grandey et al. (2016), for example, CAM5 simulations driven by interannually varying fire emissions constrained by GFED4s yielded a global mean net radiative effect of -1.0 W m^{-2}, dominated by the cloud shortwave response to organic carbon aerosol. However, our CAM5-2xAFBC simulation, which includes prognostic MAM3 aerosols and thus aerosol indirect effects (and aerosol-meteorology coupling), supports our conclusions.

Furthermore, CMIP6 fixed SST simulations with doubled fire emissions also reproduce the dynamical response in the tropical Atlantic. These models use different parameterizations than CESM, and also include a sophisticated treatment of aerosols, including aerosol indirect effects and aerosol-meteorology coupling. This increases the robustness to our CESM responses in the Atlantic. Although CMIP6 simulations lack a teleconnection to the tropical Pacific, this is likely due to lack of ocean-atmosphere feedbacks, as our semi-empirical fine-mode aerosol fixed SST simulations also lack a remote response to the tropical Pacific. Similar to our results, Tosca et al. (2013) show that fire aerosols yield a reduction in central and eastern tropical Pacific precipitation (and sea surface temperatures). Their response, however spans most of the tropical Pacific. Although south Africa is dominated by a decrease in precipitation (particularly over the continent), there is a weak precipitation increase off the coast, which is also qualitatively similar to our results.

Observations support a relationship between south African biomass burning and ENSO, particularly during boreal fall (SON). Although ENSO appears to lead the relationship, as in Andela and van der Werf (2014), we find observational evidence that south African biomass burning emissions may yield a dynamical response in the tropical Atlantic similar to model simulations. Thus, although our work is subject to several caveats, we suggest a possible two-way feedback between ENSO and south African biomass burning, with La Niña promoting more south African SON biomass burning emissions, which may then strengthen the developing La Niña. Additional coupled ocean-atmosphere simulations using multiple models with sophisticated aerosol schemes should be performed to further evaluate the robustness of this response.

Acknowledgments

This study was funded by NSF award AGS-1455682. The authors declare no competing financial interests. The semi-empirical aerosol direct radiative effect used in this study

can be downloaded from 4TU.ResearchData at `https://doi.org/10.4121/uuid:29d8464a-ef96-496c-8c11-3f18132e7466`.

References

Acosta Navarro, J. C., Varma, V., Riipinen, I., Seland, Ø., Kirkevåg, A., Struthers, H., ... Ekman, A. M. L. (2016). Amplification of arctic warming by past air pollution reductions in europe. *Nature Geoscience*, *9*(4), 277–281, doi: 10.1038/ngeo2673.

Adebiyi, A. A., & Zuidema, P. (2016). The role of the southern African easterly jet in modifying the southeast Atlantic aerosol and cloud environments. *Quart. J. Royal Meteor. Soc.*, *142*, 1574-1589, doi: 10.1002/qj.2765.

Adler, R., Huffman, G. J., Chang, A., R.Ferraro, & et al. (2003). The version-2 global precipitation climatology project (GPCP) monthly precipitation analysis (1979-present). *J. Hydrometeor.*, *4*(6), 1147-1167.

Allan, R. J., & Ansell, T. J. (2006). A new globally complete monthly histroical mean sea level pressure data set (HadSLP2): 1850-2004. *J. Climate*, *19*, 5816-5842.

Allen, R. J. (2015). A 21st century northward tropical precipitation shift caused by future anthropogenic aerosol reductions. *Journal of Geophysical Research: Atmospheres*, *120*(18), 9087-9102, doi: 10.1002/2015JD023623.

Allen, R. J., & Ajoku, O. (2016). Future aerosol reduction and widening of the nothern tropical belt. *J. Geophys. Res.*, 1-22, doi: 10.1002/2016JD024803.

Allen, R. J., Amiri-Farahani, A., Lamarque, J.-F., Smith, C., Shindell, D., Hassan, T., & Chung, C. E. (2019). Observationally-constrained aerosol-cloud semi-direct effects. *npj Climate and Atmospheric Science*.

Allen, R. J., Evan, A. T., & Booth, B. B. B. (2015). Interhemispheric aerosol radiative forcing and tropical precipitation shifts during the late twentieth century. *Journal of Climate*, *28*(20), 8219-8246, doi: 10.1175/JCLI-D-15-0148.1.

Allen, R. J., & Landuyt, W. (2014). The vertical distribution of black carbon in CMIP5 models: Comparison to observations and the importance of convective transport. *Journal of Geophysical Research: Atmospheres*, *119*(8), 4808-4835, 10.1002/2014JD021595.

Allen, R. J., Norris, J. R., & Kovilakam, M. (2014). Influence of anthropogenic aerosols and the Pacific Decadal Oscillation of tropical belt width. *Nature Geosci.*, *7*, 270-274.

Allen, R. J., & Sherwood, S. C. (2011). The impact of natural versus anthropogenic aerosols on atmospheric circulation in the Community Atmosphere Model. *Climate Dyn.*, *36*, 1959-1978, doi: 10.1007/s00382-010-0898-8.

Allen, R. J., Sherwood, S. C., Norris, J. R., & Zender, C. S. (2012a). The equilibrium response to idealized thermal forcings in a comprehensive GCM: Implications for recent tropical expansion. *Atmos. Chem. Phys.*, *12*, 4795-4816, doi: 10.5194/acp-12-4795-2012.

Allen, R. J., Sherwood, S. C., Norris, J. R., & Zender, C. S. (2012b). Recent Northern Hemisphere tropical expansion primarily driven by black carbon and tropospheric ozone. *Nature*, *485*, 350-354, doi: 10.1038/nature11097.

Andela, N., & van der Werf, G. R. (2014). Recent trends in African fires driven by cropland expansion and El Niño to La Niña transition. *Nature Climate Change*, *4*(9), 791–795, doi: 10.1038/nclimate2313.

Ban-Weiss, G. A., Cao, L., Bala, G., & Caldeira, K. (2012). Dependence of climate forcing and response on the altitude of black carbon aerosols. *Climate Dyn.*, *38*, 897-911, doi: 10.1007/s00382-011-1052-y.

Biasutti, M., & Giannini, A. (2006). Robust Sahel drying in response to late 20th century forcings. *Geophysical Research Letters*, *33*(11), doi: 10.1029/2006GL026067.

Bollasina, M. A., Ming, Y., & Ramaswamy, V. (2011). Anthropogenic Aerosols and the Weakening of the South Asian Summer Monsoon. *Science*, *334*(6055), 502-505, doi: 10.1126/science.1204994.

Bond, T. C., Bhardwaj, E., Dong, R., Jogani, R., Jung, S., Roden, C., ... Trautmann, N. M. (2007). Historical emissions of black and organic carbon aerosol from energy related combustion, 1850-2000. *Glob. Biogeochem. Cyc.*, *21*(GB2018), doi:10.1029/2006GB002840.

Bond, T. C., Doherty, S. J., Hahey, D. W., & et al. (2013). Bounding the role of black carbon in the climate system: A scientific assessment. *J. Geophys. Res.*, *118*, 5380-5552, doi:10.1002/jgrd.50171.

Booth, B. B. B., Dunstone, N. J., Halloran, P. R., Andrews, T., & Bellouin, N. (2012). Aerosols implicated as a prime driver of twentieth-century North Atlantic climate variability. *Nature*, *484*(7393), 228–232.

Boucher, O., Randall, D., Artaxo, P., Bretherton, C., Feingold, G., Forster, P., ... Zhang, X. (2013). *Clouds and Aerosols. In: Climate Change 2013: The Physical Science Basis. Contribution of Working Group I to the Fifth Assessment Report of the Intergovernmental Panel on Climate Change [Stocker, T.F., D. Qin, G.-K. Plattner, M. Tignor, S.K. Allen, J. Boschung, A. Nauels, Y. Xia, V. Bex and P.M. Midgley (eds.)]* (Tech. Rep.). Cambridge University Press, Cambridge, United Kingdom and New York, NY, USA.

Briegleb, B. P. (1992). Delta-eddington approximation for solar radiation in the NCAR Community Climate Model. *J. Geophys. Res.-Atmos.*, *97*, 7603-7612, doi: 10.1029/92JD00291.

Chand, D., Wood, R., Anderson, T. L., Satheesh, S. K., & Charlson, R. J. (2009). Satellite-derived direct radiative effect of aerosols dependent on cloud cover. *Nature Geosci.*, *2*, 181-184.

Chiang, J. C. H., & Vimont, D. J. (2004). Analogous Pacific and Atlantic Meridional Modes of Tropical Atmosphere–Ocean Variability. *Journal of Climate*, *17*(21), 4143–4158, doi: 10.1175/JCLI4953.1.

Chin, M., Ginoux, P., Kinne, S., Torres, O., Holben, B. N., Duncan, B. N., ... Nakajima, T. (2002). Tropospheric aerosol optical thickness from the GOCART model and comparisons with satellite and sunphotometer measurements. *J. Atmos. Sci.*, *59*, 461-483.

Choi, J.-O., & Chung, C. E. (2014). Sensitivity of aerosol direct radiative forcing to aerosol vertical profile. *Tellus B*, *66*, 24376, doi: 10.3402/tellusb.v66.24376,.

Chung, C., & Ramanathan, V. (2006). Weakening of the North Indian SST gradients and the monsoon rainfall in India and the Sahel. *J. Climate*, *19*, 2036-2045.

Chung, C. E. (2006). Steady vs. fluctuating aerosol radiative forcing in a climate model. *J. Korean. Meteor. Soc.*, *42*(6), 411-417.

Chung, C. E., Chu, J.-E., Lee, Y., van Noije, T., Jeoung, H., Ha, K.-J., & Marks, M. (2016). Global fine-mode aerosol radiative effect, as constrained by comprehensive observations. *Atmospheric Chemistry and Physics*, *16*(13), 8071-8080, 10.5194/acp-16-8071-2016.

Chung, C. E., Ramanathan, V., & Decremer, D. (2012). Observationally constrained estimates of carbonaceous aerosol radiative forcing. *Proceedings of the National Academy of Sciences*, *109*(29), 11624–11629, doi: 10.1073/pnas.1203707109.

Chung, C. E., Ramanathan, V., Kim, D., & Podgorny, I. A. (2005). Global anthropogenic aerosol direct forcing derived from satellite and ground-based observations. *J. Geophys. Res.*, *110*, D24207, doi:10.1029/2005JD006356.

Clough, S. A., Shephard, M. W., Mlawer, E. J., Delamere, J. S., Iacono, M. J., Cady-Pereira, K., ... Brown, P. D. (2005). Atmospheric radiative transfer modeling: A summary of the AER codes. *J. Quant. Spect. Rad. Transfer*, *91*, 233-244, doi:10.1016/j.jqsrt.2004.05.058.

Coakley, J. A., Cess, R. D., & Yurevich, F. B. (1983). The effect of tropospheric aerosols on the Earth's radiation budget: A paramterization for climate models. *J. Atmos. Sci.*, *40*, 116-138, doi: 10.1175/1520-0469(1983)040¡0116:TEOTAO¿2.0.CO;2.

Cohen, J. B., & Wang, C. (2014). Estimating global black carbon emissions using a top-down Kalman Filter approach. *Journal of Geophysical Research: Atmospheres*, *119*(1), 307-323, 10.1002/2013JD019912.

Collins, W. J., Lamarque, J.-F., Schulz, M., Boucher, O., Eyring, V., Hegglin, M. I., … Smith, S. J. (2017). AerChemMIP: quantifying the effects of chemistry and aerosols in CMIP6. *Geoscientific Model Development*, *10*(2), 585-607, doi: 10.5194/gmd-10-585-2017.

de Graaf, M., Bellouin, N., Tilstra, L. G., Haywood, J., & Stammes, P. (2014). Aerosol direct radiative effect of smoke over clouds over the southeast atlantic ocean from 2006 to 2009. *Geophysical Research Letters*, *41*(21), 7723-7730, doi: 10.1002/2014GL061103.

de Graaf, M., Tilstra, L. G., Wang, P., & Stammes, P. (2012). Retrieval of the aerosol direct radiative effect over clouds from spaceborne spectrometry. *Journal of Geophysical Research: Atmospheres*, *117*(D7), doi: 10.1029/2011JD017160.

Deser, C., Alexander, M. A., Xie, S.-P., & Phillips, A. S. (2010). Sea surface temperature variability: patterns and mechanisms. *Annu. Rev. Mar. Sci.*, *2*, 114-143, doi: 10.1146/annurev-marine-120408-151453.

Ding, H., Keenlyside, N. S., & Latif, M. (2012). Impact of the Equatorial Atlantic on the El Niño Southern Oscillation. *Climate Dynamics*, *38*(9), 1965–1972, doi: 10.1007/s00382-011-1097-y.

England, M. H., McGregor, S., Spence, P., Meehl, G. A., Timmermann, A., Cai, W., … Santoso, A. (2014). Recent intensification of wind-driven circulation in the Pacific and the ongoing warming hiatus. *Nature Climate Change*, *4*, 222 EP, doi: 10.1038/nclimate2106.

Feng, N., & Christopher, S. A. (2015). Measurement-based estimates of direct radiative effects of absorbing aerosols above clouds. *Journal of Geophysical Research: Atmospheres*, *120*(14), 6908-6921, doi: 10.1002/2015JD023252.

Frauen, C., & Dommenget, D. (2012). Influences of the tropical Indian and Atlantic Oceans on the predictability of ENSO. *Geophysical Research Letters*, *39*(2), doi: 10.1029/2011GL050520.

Gelaro, R., McCarty, W., Suárez, M. J., Todling, R., Molod, A., Takacs, L., … Zhao, B. (2017). The Modern-Era Retrospective Analysis for Research and Applications, Version 2 (MERRA-2). *Journal of Climate*, *30*(14), 5419-5454, doi: 10.1175/JCLI-D-16-0758.1.

Gettelman, A., Liu, X., Ghan, S. J., Morrison, H., Park, S., Conley, A. J., … Li, J. L. F. (2010). Global simulations of ice nucleation and ice supersaturation with an improved cloud scheme in the Community Atmosphere Model. *J. Geophys. Res*, *115*, D18216, doi:10.1029/2009JD013797.

Grandey, B. S., Lee, H.-H., & Wang, C. (2016). Radiative effects of interannually varying vs. interannually invariant aerosol emissions from fires. *Atmospheric Chemistry and Physics*, *16*(22), 14495–14513, doi: 10.5194/acp-16-14495-2016.

Guo, L., Turner, A. G., & Highwood, E. J. (2016). Local and Remote Impacts of Aerosol Species on Indian Summer Monsoon Rainfall in a GCM. *Journal of Climate*, *29*(19), 6937-6955, doi: 10.1175/JCLI-D-15-0728.1.

Hack, J. (1994). Parameterization of moist convection in the National Center for Atmospheric Research Community Climate model (CCM2). *J. Geophys. Res.*, *99*, 5551-5568.

Hurrell, J. W., Holland, M. M., Gent, P. R., Ghan, S., Kay, J. E., Kushner, P. J., … Marshall, S. (2013). The community earth system model: A framework for collaborative research. *Bulletin of the American Meteorological Society*, *94*(9), 1339-1360, doi: 10.1175/BAMS-D-12-00121.1.

Hwang, Y.-T., Frierson, D. M. W., & Kang, S. M. (2013). Anthropogenic sulfate aerosol and the southward shift of tropical precipitation in the late 20th century. *Geophysical Research Letters*, *40*(11), 2845-2850, doi: 10.1002/grl.50502.

Iacono, M. J., Delamere, J. S., Mlawer, E. J., Shephard, M. W., Clough, S. A., & Collins, W. D. (2008). Radiative forcing by long-lived greenhouse gases: Calculations with the AER radiative transfer models. *J. Geophys. Res.-Atmos.*, *113*, D13103, doi: 10.1029/2008JD009944.

Jiang, Y., Lu, Z., Liu, X., Qian, Y., Zhang, K., Wang, Y., & Yang, X.-Q. (2016). Impacts of global open-fire aerosols on direct radiative, cloud and surface-albedo effects simulated with cam5. *Atmospheric Chemistry and Physics*, *16*(23), 14805–14824, doi: 10.5194/acp-16-14805-2016.

Joseph, J. H., Wiscombe, W. J., & Weinman, J. A. (1976). The delta-Eddington approximation for radiative flux transfer. *J. Atmos. Sci.*, *33*, 2452-2459, doi: 10.1175/1520-0469(1976)033¡2452:TDEAFR¿2.0.CO;2.

Kaiser, J. W., Heil, A., Andreae, M. O., Benedetti, A., Chubarova, N., Jones, L., … van der Werf, G. R. (2012). Biomass burning emissions estimated with a global fire assimilation system based on observed fire radiative power. *Biogeosciences*, *9*(1), 527–554, doi: 10.5194/bg-9-527-2012.

Kaplan, A., Cane, M. A., Kushnir, Y., Clement, A. C., Blumenthal, M. B., & Rajagopalan, B. (1998). Analyses of global sea surface temperature 1856–1991. *Journal of Geophysical Research: Oceans*, *103*(C9), 18567-18589, doi: 10.1029/97JC01736.

Keenlyside, N. S., Ding, H., & Latif, M. (2013). Potential of equatorial Atlantic variability to enhance El Niño prediction. *Geophysical Research Letters*, *40*(10), 2278-2283, doi: 10.1002/grl.50362.

Keenlyside, N. S., & Latif, M. (2007). Understanding equatorial Atlantic interannual variability. *Journal of Climate*, *20*(1), 131-142, doi: 10.1175/JCLI3992.1.

Koch, D., Schulz, M., Kinne, S., McNaughton, C., Spackman, J. R., Balkanski, Y., … Zhao, Y. (2009). Evaluation of black carbon estimations in global aerosol models. *Atmos. Chem. Phys.*, *9*(22), 9001–9026.

Kovilakam, M., & Mahajan, S. (2015). Black carbon aerosol-induced Northern Hemisphere tropical expansion. *Geophysical Research Letters*, *42*, 4964-4972, doi:10.1002/2015GL064559.

Kristjansson, J. E., Iversen, T., Kirkevag, A., Seland, O., & Debernard, J. (2005). Response of the climate system to aerosol direct and indirect forcing: Role of cloud feedbacks. *J. Geophys. Res.*, *110*, D24206, doi:10.1029/2005JD006299.

Kucharski, F., Kang, I.-S., Farneti, R., & Feudale, L. (2011). Tropical Pacific response to 20th century Atlantic warming. *Geophysical Research Letters*, *38*(3), doi: 10.1029/2010GL046248.

Kucharski, F., Parvin, A., Rodriguez-Fonseca, B., Farneti, R., Martin-Ray, M., Polo, I., … Mechoso, C. R. (2016). The teleconnection of the Tropical Atlantic to Indo-Pacific sea surface temperatures on inter-annual to centennial time scales: A review of recent findings. *Atmosphere*, *7*(29), doi: 10.3390/atmos7020029.

Landry, J.-S., Partanen, A.-I., & Matthews, H. D. (2017). Carbon cycle and climate effects of forcing from fire-emitted aerosols. *Environmental Research Letters*, *12*(2), 025002, doi: 10.1088/1748-9326/aa51de.

Lee, H.-T., Gruber, A., Ellingson, R. G., & Laszlo, I. (2007). Development of the HIRS Outgoing Longwave Radiation Climate Dataset. *Journal of Atmospheric and Oceanic Technology*, *24*(12), 2029-2047, doi: 10.1175/2007JTECHA989.1.

Lee, K., & Chung, C. E. (2013). Observationally-constrained estimates of global fine-mode AOD. *Atmospheric Chemistry and Physics*, *13*(5), 2907–2921, 10.5194/acp-13-2907-2013.

Lewinschal, A., Ekman, A. M. L., Hansson, H.-C., Sand, M., Berntsen, T. K., & Langner, J. (2019). Local and remote temperature response of regional so2 emissions. *Atmospheric Chemistry and Physics*, *19*(4), 2385–2403, doi:

10.5194/acp-19-2385-2019.

Lewinschal, A., Ekman, A. M. L., & Kornich, H. (2013). The role of precipitation in aerosol-induced changes in northern hemisphere wintertime stationary waves. *Climate Dynamics*, *41*, 647-661.

Li, X., Xie, S.-P., Gille, S. T., & Yoo, C. (2012). Atlantic-induced pan-tropical climate change over the past three decades. *Nature Climate Change*, *6*, 275 EP, doi: 10.1038/nclimate2840.

Li, Z., Lau, W. K.-M., Ramanathan, V., Wu, G., Ding, Y., Manoj, M. G., ... Brasseur, G. P. (2016). Aerosol and monsoon climate interactions over Asia. *Reviews of Geophysics*, *54*(4), 866-929, doi: 10.1002/2015RG000500.

Liepert, B. G., Feichter, J., Lohmann, U., & Roeckner, E. (2004). Can aerosols spin down the water cycle in a warmer and moister world? *Geophys. Res. Lett.*, *31*, L06207, doi: 10.1029/2003GL019060.

Liu, Z., Vaughan, M., Winker, D., Kittaka, C., Getzewich, B., Kuehn, R., ... Hostetler, C. (2009). The CALIPSO Lidar Cloud and Aerosol Discrimination: Version 2 Algorithm and Initial Assessment of Performance. *Journal of Atmospheric and Oceanic Technology*, *26*(7), 1198-1213, 10.1175/2009JTECHA1229.1.

Lou, S., Yang, Y., Wang, H., Lu, J., Smith, S. J., Liu, F., & Rasch, P. J. (2019). Black Carbon Increases Frequency of Extreme ENSO Events. *Journal of Climate*, *32*(23), 8323-8333, doi: 10.1175/JCLI-D-19-0549.1.

Lu, Z., Liu, X., Zhang, Z., Zhao, C., Meyer, K., Rajapakshe, C., ... Penner, J. E. (2018). Biomass smoke from southern Africa can significantly enhance the brightness of stratocumulus over the southeastern Atlantic Ocean. *Proceedings of the National Academy of Sciences*, *115*(12), 2924–2929,doi: 10.1073/pnas.1713703115.

Mallet, M., Nabat, P., Zuidema, P., Redemann, J., Sayer, A. M., Stengel, M., ... Formenti, P. (2019). Simulation of the transport, vertical distribution, optical properties and radiative impact of smoke aerosols with the ALADIN regional climate model during the ORACLES-2016 and LASIC experiments. *Atmospheric Chemistry and Physics*, *19*(7), 4963–4990, doi: 10.5194/acp-19-4963-2019.

Martín-Rey, M., Polo, I., Rodríguez-Fonseca, B., & Kucharski, F. (2012). Changes in the interannual variability of the tropical Pacific as a response to an equatorial Atlantic forcing. *Scientia Marina*, *76*(S2), 105-116, doi: 10.3989/scimar.03610.19A.

McGregor, S., Timmermann, A., Stuecker, M. F., England, M. H., Merrifield, M., Jin, F.-F., & Chikamoto, Y. (2014). Recent Walker circulation strengthening and Pacific cooling amplified by Atlantic warming. *Nature Climate Change*, *4*, 888 EP, doi: 10.1038/nclimate2330.

Meehl, G. A., Arblaster, J. M., & Collins, W. D. (2008). Effects of black carbon aerosols on the Indian monsoon. *J. Climate*, *21*, 2869-2882.

Ming, Y., & Ramaswamy, V. (2009). Nonlinear climate and hydrological responses to aerosol effects. *Journal of Climate*, *22*(6), 13290-1339, doi: 10.1175/2008JCLI2362.1.

Ming, Y., Ramaswamy, V., & Persad, G. (2010). Two opposing effects of absorbing aerosols on global-mean precipitation. *Geophys. Res. Lett.*, *37*, L13701, doi: 10.1029/2010GL042895.

Mlawer, E. J., Taubman, S. J., Brown, P. D., Iacono, M. J., & Clough, S. A. (1997). Radiative transfer for inhomogeneous atmospheres: RRTM, a validated correlated-k model for the longwave. *J. Geophys. Res.-Atmos.*, *102*, 16663-16682, doi: 10.1029/97JD00237.

Morrison, H., & Gettelman, A. (2008). A new two-moment bulk stratiform cloud microphysics scheme in the Community Atmosphere Model, version 3 (CAM3), Part I: Description and numerical tests. *J. Climate*, *21*, 3642-3659, doi:

10.1175/2008JCLI2105.1.

Myhre, G., & Samset, B. H. (2015). Standard climate models radiation codes underestimate black carbon radiative forcing. *Atmospheric Chemistry and Physics*, *15*(5), 2883-2888, 10.5194/acp-15-2883-2015.

Myhre, G., Shindell, D., Bréon, F.-M., Collins, W., Fuglestvedt, J., Huang, J., ... Zhang, H. (2013). *Anthropogenic and Natural Radiative Forcing. In: Climate Change 2013: The Physical Science Basis. Contribution of Working Group I to the Fifth Assessment Report of the Intergovernmental Panel on Climate Change [Stocker, T.F., D. Qin, G.-K. Plattner, M. Tignor, S.K. Allen, J. Boschung, A. Nauels, Y. Xia, V. Bex and P.M. Midgley (eds.)]* (Tech. Rep.). Cambridge University Press, Cambridge, United Kingdom and New York, NY, USA.

Neale, R. B., Gettelman, A., Park, S., & et al. (2010). *Description of the NCAR Community Atmosphere Model (CAM 5.0)* (Tech. Rep. Nos. NCAR/TN-486+STR). Boulder, CO, 268 pp.: National Center for Atmospheric Research.

Neale, R. B., Richter, J. H., Conley, A. J., Park, S., Lauritzen, P. H., Gettelman, A., ... Lin, S.-J. (2010). *Description of the NCAR Community Atmosphere Model (CAM 4.0)* (Tech. Rep. Nos. NCAR/TN-???+STR). Boulder, CO, 194 pp.: National Center for Atmospheric Research.

Park, S., & Allen, R. J. (2015). Understanding influences of convective transport and removal processes on aerosol vertical distribution. *Geophysical Research Letters*, *42*(23), 10,438-10,444, 10.1002/2015GL066175.

Park, S., & Bretherton, C. S. (2009). The University of Washington shallow convection and moist turbulence schemes and their impact of climate simulations with the Community Atmosphere Model. *J. Climate*, *22*, 3449-3469, doi:10.1175/2008JCLI2557.1.

Pendergrass, A. G., & Hartmann, D. L. (2012). Global-mean precipitation and black carbon in AR4 simulations. *Geophysical Research Letters*, *39*(1), doi: 10.1029/2011GL050067.

Peterson, T. C., & Vose, R. S. (1997). An overview of the global historical climatological network temperature database. *Bull. Amer. Meteor. Soc.*, *78*, 2837-2849.

Pistone, K., Redemann, J., Doherty, S., Zuidema, P., Burton, S., Cairns, B., ... Xu, F. (2019). Intercomparison of biomass burning aerosol optical properties from in situ and remote-sensing instruments in ORACLES-2016. *Atmospheric Chemistry and Physics*, *19*(14), 9181–9208, doi: 10.5194/acp-19-9181-2019.

Podgorny, I. A., Conant, W. C., Ramanathan, V., & Satheesh, S. K. (2000). Aerosol modulation of atmospheric and solar heating over the tropical Indian Ocean. *Tellus, Ser. B*, *52*, 947-958, doi: 10.3402/tellusb.v52i3.17077.

Polo, I., Martin-Rey, M., Rodriguez-Fonseca, B., Kucharski, F., & Mechoso, C. R. (2015). Processes in the Pacific La Niña onset triggered by the Atlantic Niño. *Climate Dynamics*, *44*(1), 115–131, doi: 10.1007/s00382-014-2354-7.

Polson, D., Bollasina, M., Hegerl, G. C., & Wilcox, L. J. (2014). Decreased monsoon precipitation in the Northern Hemisphere due to anthropogenic aerosols. *Geophysical Research Letters*, *41*(16), 6023-6029, doi: 10.1002/2014GL060811.

Potter, C. S., Randerson, J. T., Field, C. B., Matson, P. A., Vitousek, P. M., Mooney, H. A., & Klooster, S. A. (1993). Terrestrial ecosystem production: A process model based on global satellite and surface data. *Global Biogeochemical Cycles*, *7*(4), 811-841, doi: 10.1029/93GB02725.

Ramanathan, V., & Carmichael, G. (2008). Global and regional climate changes due to black carbon. *Nature Geosci.*, *1*, 221-227.

Ramanathan, V., Chung, C., Kim, D., Bettge, T., Buja, L., Kiehl, J. T., ... Sikka, D. R. (2005). Atmospheric brown clouds: Impacts on South Asian climate and hydrological cycle. *Proc. Natl. Acad. Sci.*, *102*, 5326-5333.

Ramanathan, V., Crutzen, P. J., Lelieveld, J., Mitra, A. P., & et al. (2001). Indian

Ocean Experiment: An integrated analysis of the climate forcing and effects of the great Indo-Asian haze. *J. Geophys. Res.*, *106*(D22), 28,371-28,398.

Randles, C. A., Colarco, P. R., & Silva, A. (2013). Direct and semi-direct aerosol effects in the NASA GEOS-5 AGCM: aerosol-climate interactions due to prognostic versus prescribed aerosols. *Journal of Geophysical Research: Atmospheres*, *118*(1), 149-169, 10.1029/2012JD018388.

Randles, C. A., da Silva, A. M., Buchard, V., Colarco, P. R., Darmenov, A., Govindaraju, R., ... Flynn, C. J. (2017). The MERRA-2 Aerosol Reanalysis, 1980 Onward. Part I: System Description and Data Assimilation Evaluation. *Journal of Climate*, *30*(17), 6823-6850, doi: 10.1175/JCLI-D-16-0609.1.

Randles, C. A., & Ramaswamy, V. (2010). Direct and semi-direct impacts of absorbing biomass burning aerosol on the climate of southern Africa: a Geophysical Fluid Dynamics Laboratory GCM sensitivity study. *Atmospheric Chemistry and Physics*, *10*(20), 9819-9831, doi: 10.5194/acp-10-9819-2010.

Rasch, P. J., & Kristjánsson, J. E. (1998). A comparison of the CCM3 model climate using diagnosed and predicted condensate parameterizations. *J. Climate*, *11*, 1587-1614.

Rodríguez-Fonseca, B., Polo, I., García-Serrano, J., Losada, T., Mohino, E., Mechoso, C. R., & Kucharski, F. (2009). Are Atlantic Ninos enhancing Pacific ENSO events in recent decades? *Geophysical Research Letters*, *36*(20), doi: 10.1029/2009GL040048.

Rotstayn, L. D., Collier, M. A., & Luo, J.-J. (2015). Effects of declining aerosols on projections of zonally averaged tropical precipitation. *Environmental Research Letters*, *10*(5), 044018, doi: 10.1088/1748-9326/10/4/044018.

Rotstayn, L. D., Collier, M. A., Shindell, D. T., & Boucher, O. (2015). Why does aerosol forcing control historical global-mean surface temperature change in cmip5 models? *Journal of Climate*, *28*(17), 6608-6625, doi: 10.1175/JCLI-D-14-00712.1.

Rotstayn, L. D., & Lohmann, U. (2002). Tropical rainfall trends and the indirect aerosol effect. *J. Climate*, *15*, 2103-2116.

Sakaeda, N., Wood, R., & Rasch, P. J. (2011). Direct and semidirect aerosol effects of southern African biomass burning aerosol. *J. Geophys. Res.*, *116*, D12205, doi:10.1029/2010JD015540.

Samset, B. H., & Myhre, G. (2015). Climate response to externally mixed black carbon as a function of altitude. *Journal of Geophysical Research: Atmospheres*, *120*(7), 2913-2927, 10.1002/2014JD022849.

Samset, B. H., Myhre, G., Forster, P. M., Hodnebrog, Ø., Andrews, T., Faluvegi, G., ... Voulgarakis, A. (2016). Fast and slow precipitation responses to individual climate forcers: A PDRMIP multimodel study. *Geophysical Research Letters*, *43*(6), 2782-2791, 10.1002/2016GL068064.

Shen, Z., & Ming, Y. (2018). The influence of aerosol absorption on the extratropical circulation. *Journal of Climate*, *31*(15), 5961-5975, doi: 10.1175/JCLI-D-17-0839.1.

Shindell, D. T., & Faluvegi, G. (2009). Climate response to regional radiative forcing during the twentieth century. *Nature Geosci.*, *2*, doi:10.1038/NGEO473.

Shindell, D. T., Lamarque, J.-F., Schulz, M., Flanner, M., Jiao, C., Chin, M., ... Lo, F. (2013). Radiative forcing in the ACCMIP historical and future climate simulations. *Atmospheric Chemistry and Physics*, *13*(6), 2939–2974, doi:10.5194/acp-13-2939-2013.

Shindell, D. T., Voulgarakis, A., Faluvegi, G., & Milly, G. (2012). Precipitation response to regional radiative forcing. *Atmospheric Chemistry and Physics*, *12*(15), 6969–6982, doi: 10.5194/acp-12-6969-2012.

Smith, R., Jones, P., Briegleb, B., Bryan, F., Danabasoglu, G., Dennis, J., ... Yeager, S. (2010). *The Parallel Ocean Program (POP) Reference Manual: Ocean Component of the Community Climate System Model (CCSM) and Community*

Earth System Model (CESM) (Tech. Rep. No. LAUR-10-01853). Los Alamos National Laboratory.

Smith, S., Andres, R., Conception, E., & Lurz, J. (2004). *Historical sulfur dioxide emissions 1850-2000: Methods and results* (Tech. Rep. No. PNNL-14537). Joint Global Change Research Institute.

Stier, P., Schutgens, N. A. J., Bellouin, N., Bian, H., Boucher, O., Chin, M., ... Zhou, C. (2013). Host model uncertainties in aerosol radiative forcing estimates: results from the AeroCom Prescribed intercomparison study. *Atmospheric Chemistry and Physics*, *13*(6), 3245–3270, doi: 10.5194/acp-13-3245-2013.

Stjern, C. W., Lund, M. T., Samset, B. H., Myhre, G., Forster, P. M., Andrews, T., ... Voulgarakis, A. (2019). Arctic amplification response to individual climate drivers. *Journal of Geophysical Research: Atmospheres*, *124*(13), 6698-6717, doi: 10.1029/2018JD029726.

Stjern, C. W., Samset, B. H., Myhre, G., Forster, P. M., Hodnebrog, Ø., Andrews, T., ... Voulgarakis, A. (2017). Rapid adjustments cause weak surface temperature response to increased black carbon concentrations. *Journal of Geophysical Research: Atmospheres*, *122*(21), 11,462-11,481, doi: 10.1002/2017JD027326.

Takahashi, C., & Watanabe, M. (2016). Pacific trade winds accelerated by aerosol forcing over the past two decades. *Nature Climate Change*, *6*, 768 EP , doi: 10.1038/nclimate2996.

Tang, T., Shindell, D., Samset, B. H., Boucher, O., Forster, P. M., Hodnebrog, Ø., ... Takemura, T. (2018). Dynamical response of Mediterranean precipitation to greenhouse gases and aerosols. *Atmospheric Chemistry and Physics*, *18*(11), 8439-8452, doi: 10.5194/acp-18-8439-2018.

Textor, C., Schulz, M., Guibert, S., Kinne, S., Balkanski, Y., Bauer, S., ... Tie, X. (2006). Analysis and quantification of the diversities of aerosol life cycles within AeroCom. *Atmos. Chem. Phys.*, *6*, 1777–1813, doi: 10.5194/acp-6-1777-2006.

Tosca, M. G., Randerson, J. T., & Zender, C. S. (2013). Global impact of smoke aerosols from landscape fires on climate and the hadley circulation. *Atmospheric Chemistry and Physics*, *13*(10), 5227–5241, doi: 10.5194/acp-13-5227-2013.

Trenberth, K. E., & Caron, J. M. (2000). The Southern Oscillation Revisited: Sea Level Pressures, Surface Temperatures, and Precipitation. *Journal of Climate*, *13*(24), 4358-4365, doi: 10.1175/1520-0442(2000)013¡4358:TSORSL¿2.0.CO;2.

Undorf, S., Polson, D., Bollasina, M. A., Ming, Y., Schurer, A., & Hegerl, G. C. (2018). Detectable impact of local and remote anthropogenic aerosols on the 20th century changes of west african and south asian monsoon precipitation. *Journal of Geophysical Research: Atmospheres*, *123*(10), 4871-4889, doi: 10.1029/2017JD027711.

van der Werf, G. R., Randerson, J. T., Giglio, L., Collatz, G. J., Mu, M., Kasibhatla, P. S., ... van Leeuwen, T. T. (2010). Global fire emissions and the contribution of deforestation, savanna, forest, agricultural, and peat fires (1997-2009). *Atmos. Chem. Phys.*, *10*, 11707-11735, doi: 10.5194/acp-10-11707-2010.

van der Werf, G. R., Randerson, J. T., Giglio, L., Gobron, N., & Dolman, A. J. (2008). Climate controls on the variability of fires in the tropics and subtropics. *Global Biogeochemical Cycles*, *22*(3), doi: 10.1029/2007GB003122.

van der Werf, G. R., Randerson, J. T., Giglio, L., van Leeuwen, T. T., Chen, Y., Rogers, B. M., ... Kasibhatla, P. S. (2017). Global fire emissions estimates during 1997–2016. *Earth System Science Data*, *9*(2), 697–720, doi: 10.5194/essd-9-697-2017.

van Marle, M. J. E., Kloster, S., Magi, B. I., Marlon, J. R., Daniau, A.-L., Field,

R. D., . . . van der Werf, G. R. (2017). Historic global biomass burning emissions for CMIP6 (BB4CMIP) based on merging satellite observations with proxies and fire models (1750–2015). *Geoscientific Model Development*, *10*(9), 3329–3357, doi: 10.5194/gmd-10-3329-2017.

Wang, C., Kucharski, F., Barimalala, R., & Bracco, A. (2009). Teleconnections of the tropical atlantic to the tropical indian and pacific oceans: A review of recent findings. *Meteorologische Zeitschrift*, *18*(4), 445-454, doi: 10.1127/0941-2948/2009/0394.

Ward, D. S., Kloster, S., Mahowald, N. M., Rogers, B. M., Randerson, J. T., & Hess, P. G. (2012). The changing radiative forcing of fires: global model estimates for past, present and future. *Atmospheric Chemistry and Physics*, *12*(22), 10857–10886, doi: 10.5194/acp-12-10857-2012.

Westervelt, D. M., Conley, A. J., Fiore, A. M., Lamarque, J.-F., Shindell, D. T., Previdi, M., . . . Horowitz, L. W. (2018). Connecting regional aerosol emissions reductions to local and remote precipitation responses. *Atmospheric Chemistry and Physics*, *18*(16), 12461–12475, doi: 10.5194/acp-18-12461-2018.

Westervelt, D. M., Mascioli, N. R., Fiore, A. M., Conley, A. J., Lamarque, J.-F., Shindell, D. T., . . . Horowitz, L. W. (2019). Local and remote mean and extreme temperature response to regional aerosol emissions reductions. *Atmospheric Chemistry and Physics Discussions*, 1–33, doi: 10.5194/acp-2019-1096.

Wilcox, L. J., Dunstone, N., Lewinschal, A., Bollasina, M., Ekman, A. M. L., & Highwood, E. J. (2019). Mechanisms for a remote response to asian anthropogenic aerosol in boreal winter. *Atmospheric Chemistry and Physics*, *19*(14), 9081–9095, doi: 10.5194/acp-19-9081-2019.

Wilcox, L. J., Highwood, E. J., & Dunstone, N. J. (2013). The influence of anthropogenic aerosol on multi-decadal variations of historical global climate. *Environ. Res. Lett.*, *8*, doi:10.1088/1748-9326/8/2/024033.

Winker, D. M., Tackett, J. L., Getzewich, B. J., Liu, Z., Vaughan, M. A., & Rogers, R. R. (2013). The global 3-D distribution of tropospheric aerosols as characterized by CALIOP. *Atmospheric Chemistry and Physics*, *13*(6), 3345–3361, 10.5194/acp-13-3345-2013.

Yang, Y., Russell, L. M., Lou, S., Lamjiri, M. A., Liu, Y., Singh, B., & Ghan, S. J. (2016). Changes in Sea Salt Emissions Enhance ENSO Variability. *Journal of Climate*, *29*(23), 8575-8588, doi: 10.1175/JCLI-D-16-0237.1.

Yu, H., Chin, M., Winker, D. M., Omar, A. H., Liu, Z., Kittaka, C., & Diehl, T. (2010). Global view of aerosol vertical distributions from CALIPSO lidar measurements and GOCART simulations: Regional and seasonal variations. *Journal of Geophysical Research: Atmospheres*, *115*(D4), doi: 10.1029/2009JD013364.

Zarzycki, C. M., & Bond, T. C. (2010). How much can the vertical distribution of black carbon affect its global direct radiative forcing? *Geophysical Research Letters*, *37*(20), 10.1029/2010GL044555.

Zhang, G. J., & McFarlane, N. A. (1995). Sensitivity of climate simulations to the parameterization of cumulus convection in the canadian climate center general-circulation model. *Atmosphere-Ocean*, *33*, 407-446.

Zuidema, P., Redemann, J., Haywood, J., Wood, R., Piketh, S., Hipondoka, M., & Formenti, P. (2016). Smoke and clouds above the southeast atlantic: Upcoming field campaigns probe absorbing aerosol's impact on climate. *Bulletin of the American Meteorological Society*, *97*(7), 1131-1135, doi: 10.1175/BAMS-D-15-00082.1.

Zuidema, P., Sedlacek III, A. J., Flynn, C., Springston, S., Delgadillo, R., Zhang, J., . . . Muradyan, P. (2018). The Ascension Island boundary layer in the remote Southeast Atlantic is often smoky. *Geophysical Research Letters*, *45*(9), 4456-4465, doi: 10.1002/2017GL076926.

Table 1. CESM experiments conducted in this study. Listed below is the name of each experiment, the aerosol perturbation applied, and the ocean setup. These experiment names are also used to designate the corresponding response to the imposed aerosol perturbation, which is obtained by subtracting an identical control simulation that lacks semi-empirical fine mode aerosol direct radiative effects without dust and sea salt. We also conduct CAM5 coupled simulations using prognostic aerosols (MAM3), which feature a doubling of 1850 black carbon fire emissions over the Africa region.

Experiment Name	Semi-Empirical Fine Mode Aerosol Effect*	Ocean Setup
CAM4-coupled	Y, Global	dynamic ocean
CAM5-coupled	Y, Global	dynamic ocean
CAM4-coupled Africa	Y, Africa region	dynamic ocean
CAM5-coupled Africa	Y, Africa region	dynamic ocean
CAM4-coupled Africa 50%	Y, Africa region, scaled by 50%	dynamic ocean
CAM4-coupled Africa 20%	Y, Africa region, scaled by 20%	dynamic ocean
CAM4-fSST	Y, Global	fixed SSTs
CAM5-fSST	Y, Global	fixed SSTs
CAM5-2xAFBC	N, MAM3 2x1850 BC fire emissions Africa region	dynamic ocean

* All experiments except CAM5-2xAFBC are conduced with fine-mode aerosol direct radiaitve effects without dust and sea salt. Control simulations are identical, but lack the aerosol perturbation.

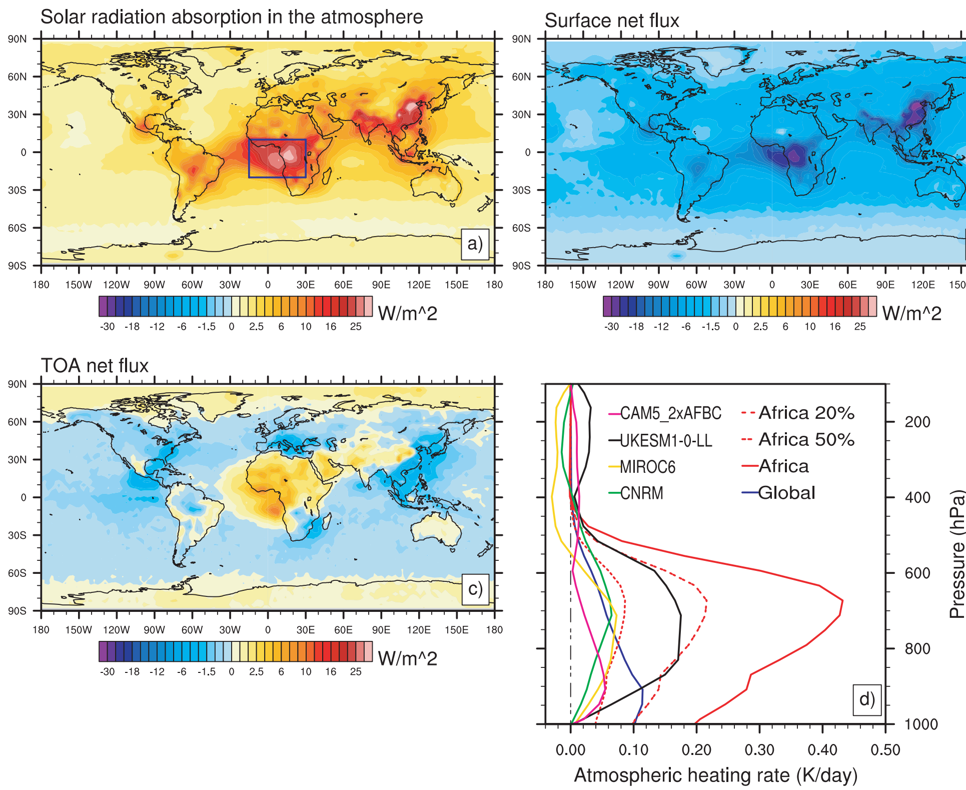

Figure 1. Annual mean semi-empirical fine mode aerosol direct radiative effects without dust and sea salt. Spatial maps of (a) atmospheric solar absorption, (b) reduction in surface solar radiation, and (c) top-of-the-atmosphere (TOA) aerosol direct radiative effect. The corresponding global annual mean values are +3.64 W m^{-2}, -3.75 W m^{-2} and -0.11 W m^{-2}, respectively. Semi-empirical aerosol direct radiative effect is estimated by C. E. Chung et al. (2016) using the MACR radiation model, and is subsequently inserted into CESM. (d) The vertical profile of atmospheric solar heating rate for the global mean (blue), the Africa region (red), Africa scaled by 50% (red dashed) and 20% (red dotted). The solar heating profile response over Africa from CMIP6 2xFIRE simulations, including CNRM-ESM2-1 (green), MIROC6 (gold) and UKESM1-0-LL (black), as well as that from CAM5-2xAFBC, is also included. The Africa region, defined as 15°W to 30°E and 20°S to 10°N, is designated by the box in (a). Panels with semi-empirical aerosol data show the aerosol direct radiative effect; CMIP6 and CAM5-2xAFBC results are based on the response. Units in (a-c) are W m^{-2} and K day^{-1} in (d).

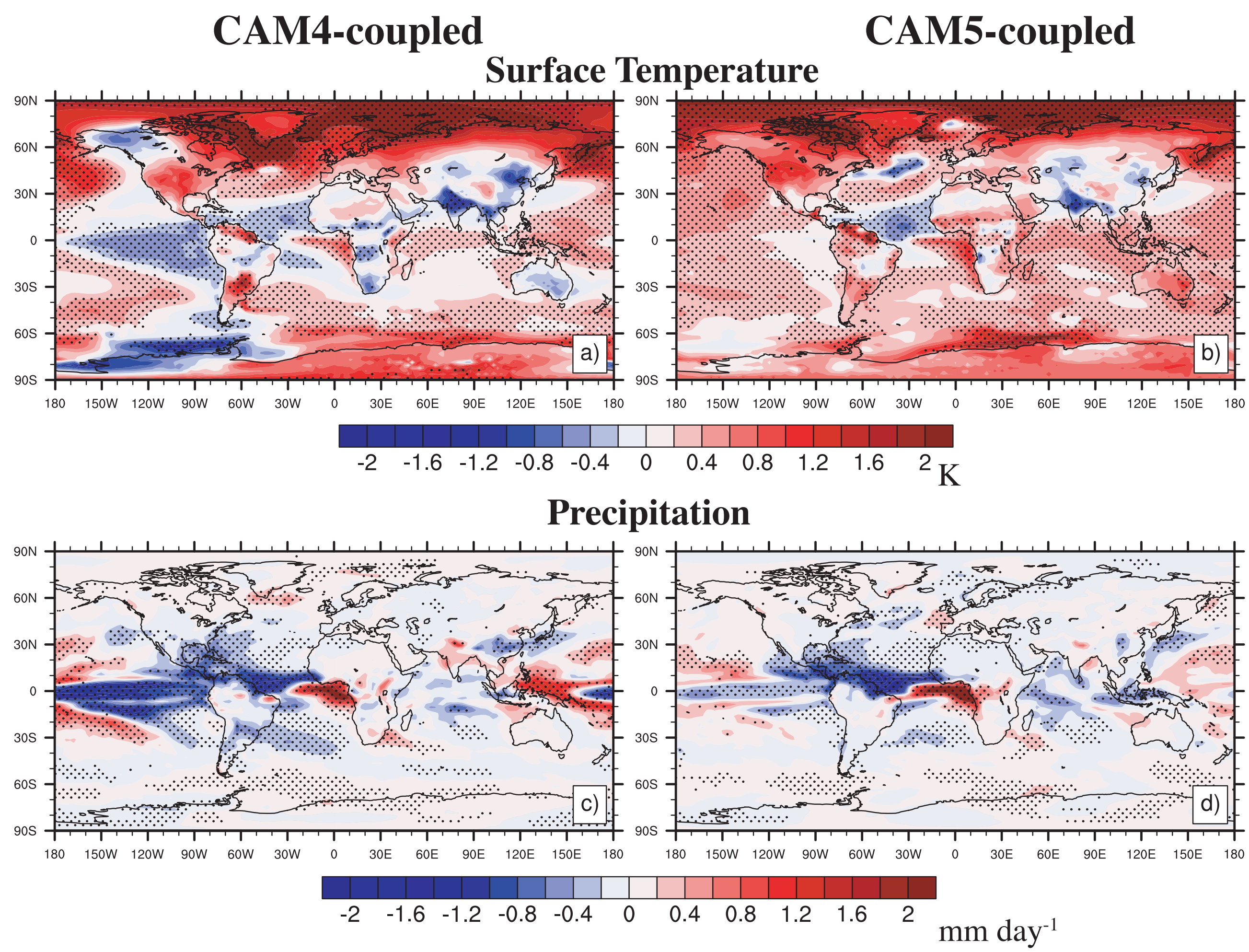

Figure 2. Annual mean (a,b) surface temperature and (c,d) precipitation response for (left panels) CAM4-coupled and (right panels) CAM5-coupled. These experiments show the climate response to global semi-empirical fine-mode aerosol direct radiative effect using coupled ocean-atmosphere simulations. Symbols denote significance at 90% confidence level, based on a t-test for the difference of means using the pooled variance. Temperature and precipitation units are K and mm day^{-1}, respectively. The global annual mean change in surface temperature is 0.28 K for CAM4-coupled and 0.39 K for CAM5-coupled, both significant at the 99% confidence level. The corresponding global annual mean change in precipitation is -0.037 and -0.024 mm day^{-1}, respectively (both significant at the 90% confidence level).

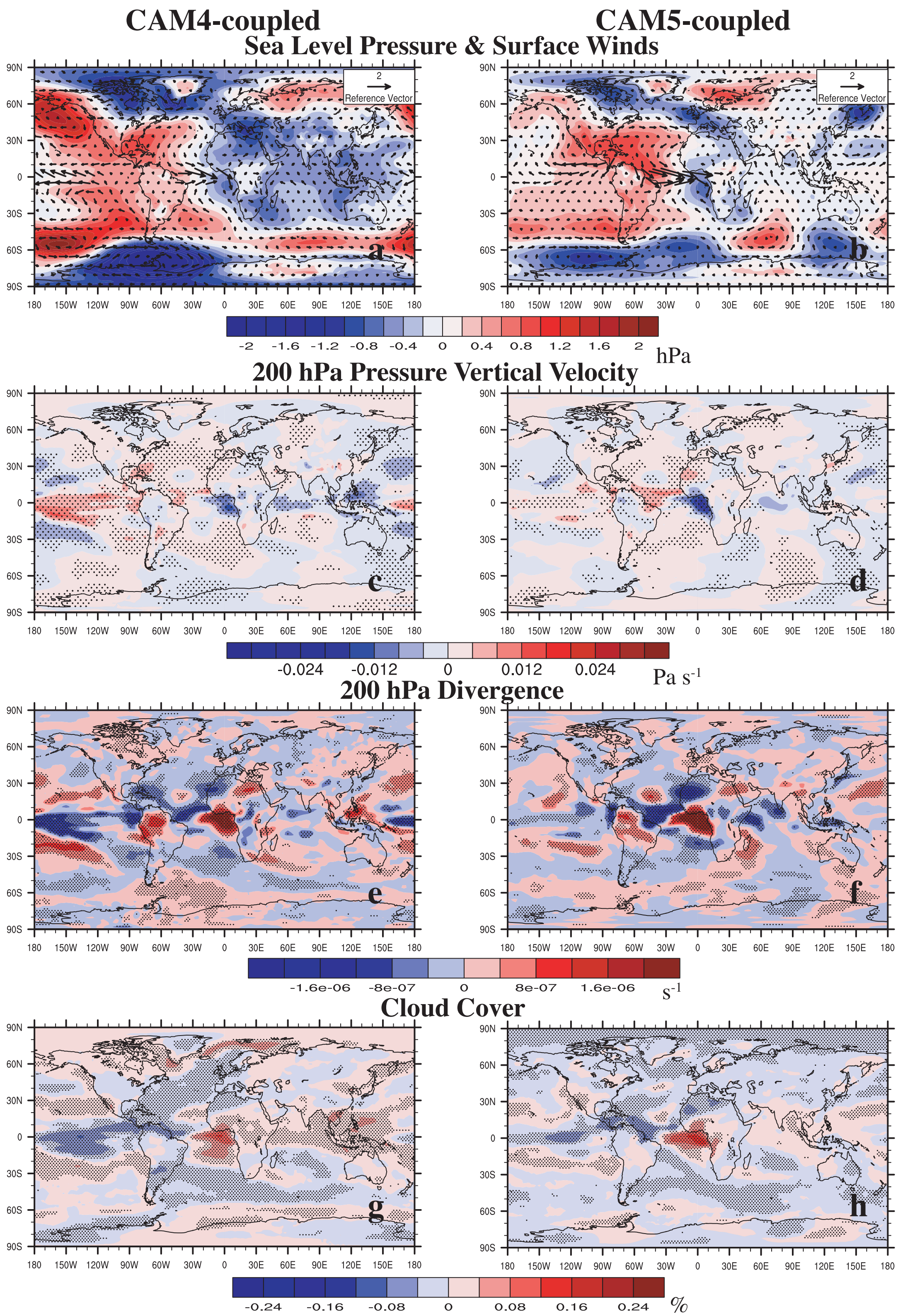

Figure 3. Annual mean dynamical responses including (a,b) sea level pressure (SLP) and surface winds; (c,d) 200 hPa pressure vertical velocity (Ω); (e,f) 200 hPa divergence; and (g,h) cloud cover for (left panels) CAM4-coupled and (right panels) CAM5-coupled. SLP and surface wind units in (a,b) are hPa and m s^{-1}, respectively. Ω, divergence, and cloud cover units are Pa s^{-1}, s^{-1} and %, respectively. These experiments show the climate response to global semi-empirical fine-mode aerosol direct radiative effect using coupled ocean-atmosphere simulations. Symbols denote significance at 90% confidence level, based on a t-test for the difference of means using the pooled variance.

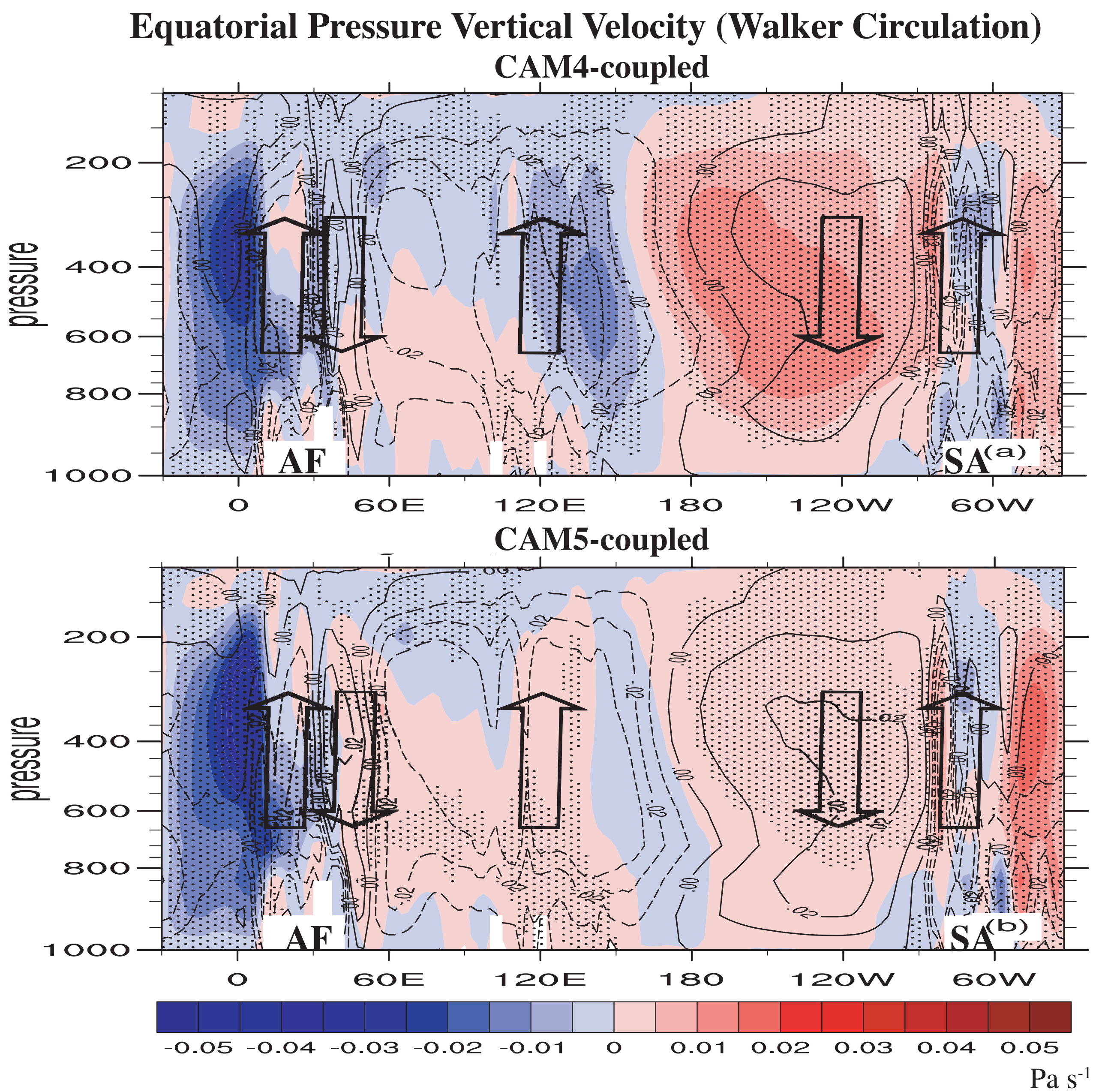

Figure 4. Annual mean vertical cross section of the pressure vertical velocity (Ω) response at the equator for (a) CAM4-coupled and (b) CAM5-coupled. These experiments show the climate response to global semi-empirical fine-mode aerosol direct radiative effect using coupled ocean-atmosphere simulations. Large black arrows represent the climatological Walker circulation in the Pacific and Atlantic. Symbols denote significance at 90% confidence level, based on a *t*-test for the difference of means using the pooled variance. Black contours show the climatological vertical velocity, with negative values (rising air) dashed. To help orient the viewer, Africa (AF) and South America (SA) are labeled. Units are Pa s^{-1}.

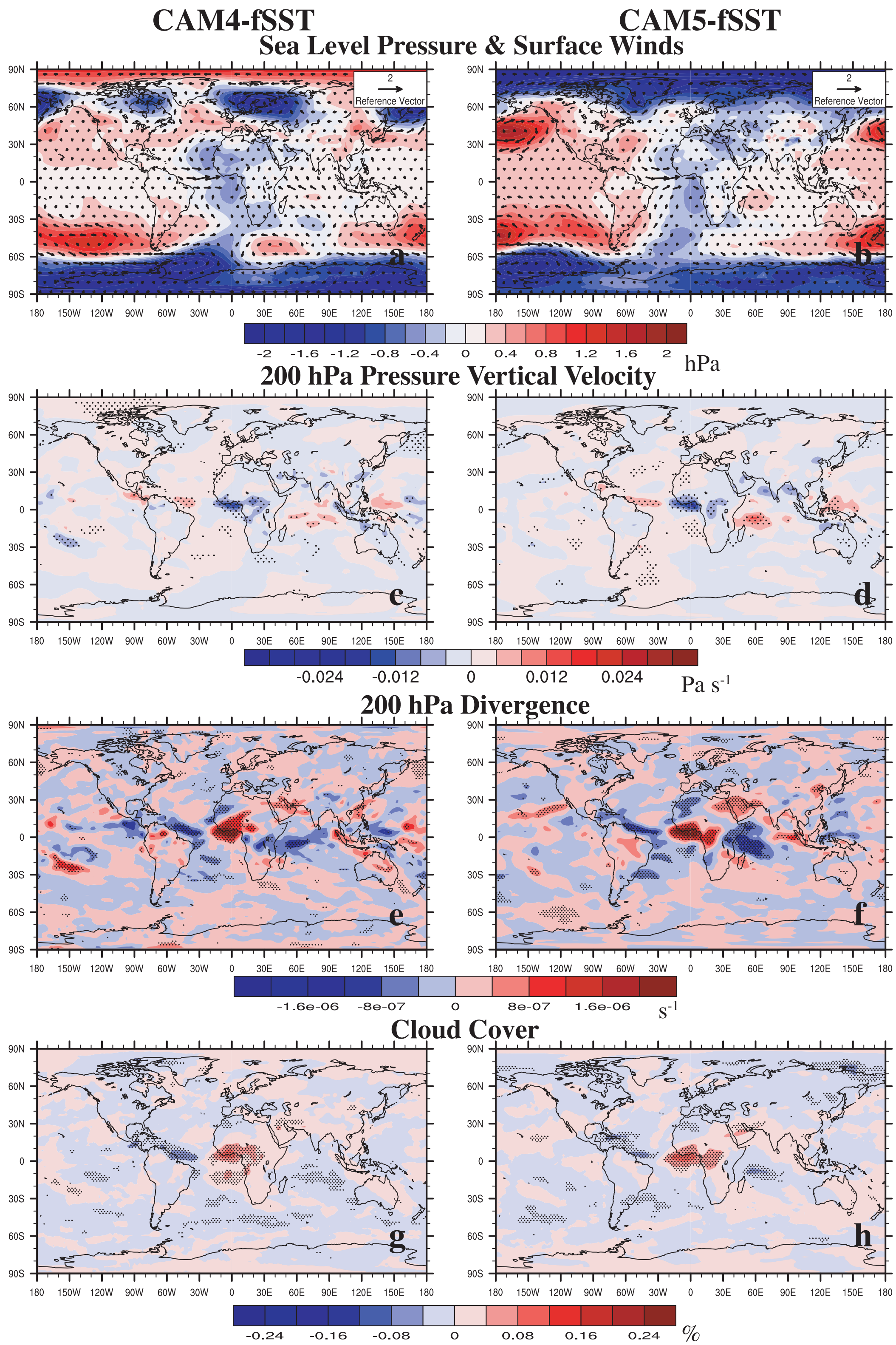

Figure 5. Annual mean dynamical responses including (a,b) sea level pressure (SLP) and surface winds; (c,d) 200 hPa pressure vertical velocity (Ω); (e,f) 200 hPa divergence; and (g,h) cloud cover for (left panels) CAM4-fSST and (right panels) CAM5-fSST. These experiments show the fast-response to global semi-empirical fine-mode aerosol direct radiative effect using fixed SSTs. SLP and surface wind units in (a,b) are hPa and m s^{-1}, respectively. Ω, divergence, and cloud cover units are Pa s^{-1}, s^{-1} and %, respectively. Symbols denote significance at 90% confidence level, based on a t-test for the difference of means using the pooled variance.

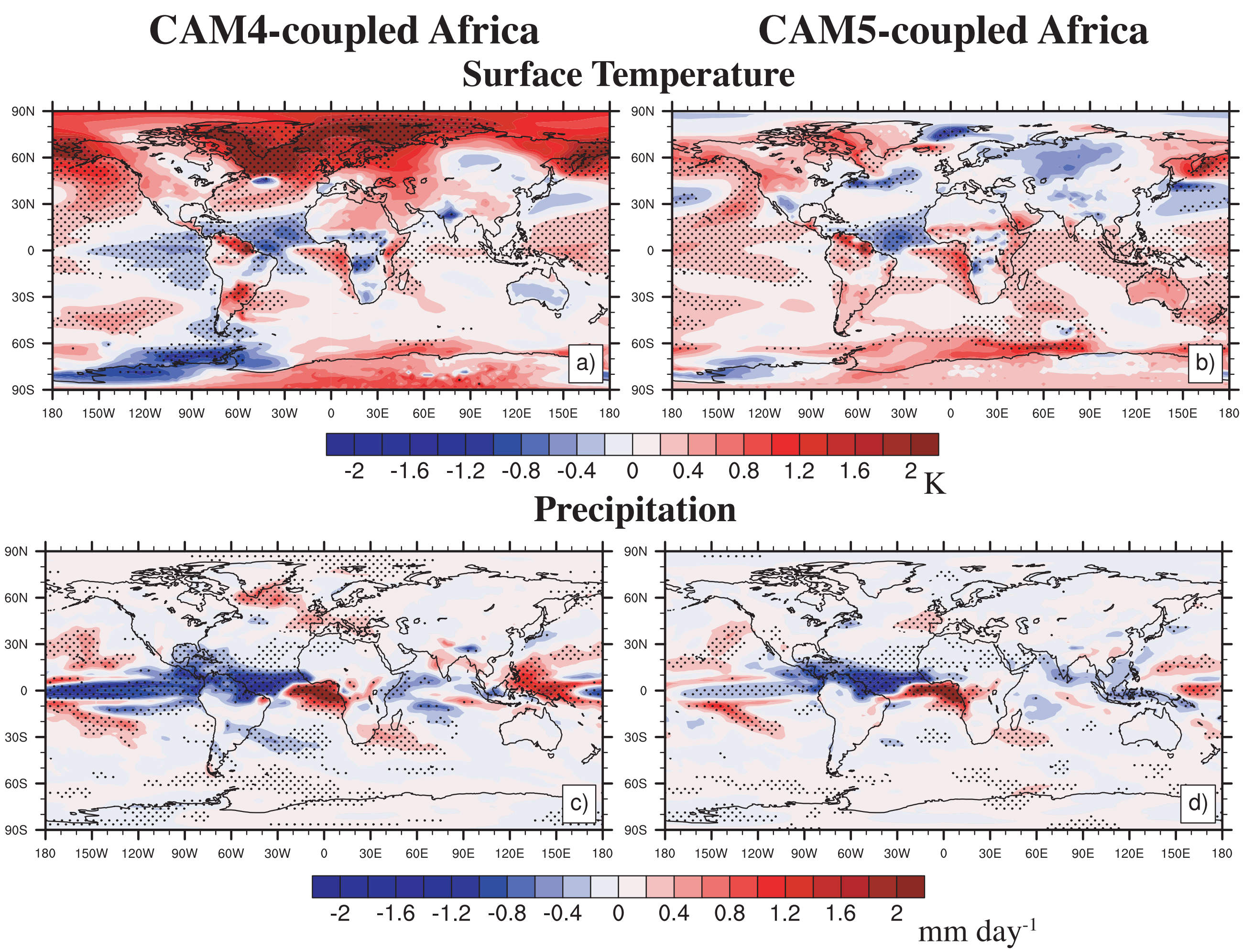

Figure 6. Annual mean (a,b) surface temperature and (c,d) precipitation response for (left panels) CAM4-coupled Africa and (right panels) CAM5-coupled Africa. These experiments show the climate response to semi-empirical fine-mode aerosol direct radiative effect without dust and sea salt over Africa only using coupled ocean-atmosphere simulations. Symbols denote significance at 90% confidence level, based on a *t*-test for the difference of means using the pooled variance. Temperature and precipitation units are K and mm day^{-1}, respectively. The global annual mean change in surface temperature is 0.23 K for CAM4-coupled Africa and 0.17 K for CAM5-coupled Africa, both significant at the 99% confidence level. The corresponding global annual mean change in precipitation is -0.034 and -0.037 mm day^{-1}, respectively (not significant at the 90% confidence level).

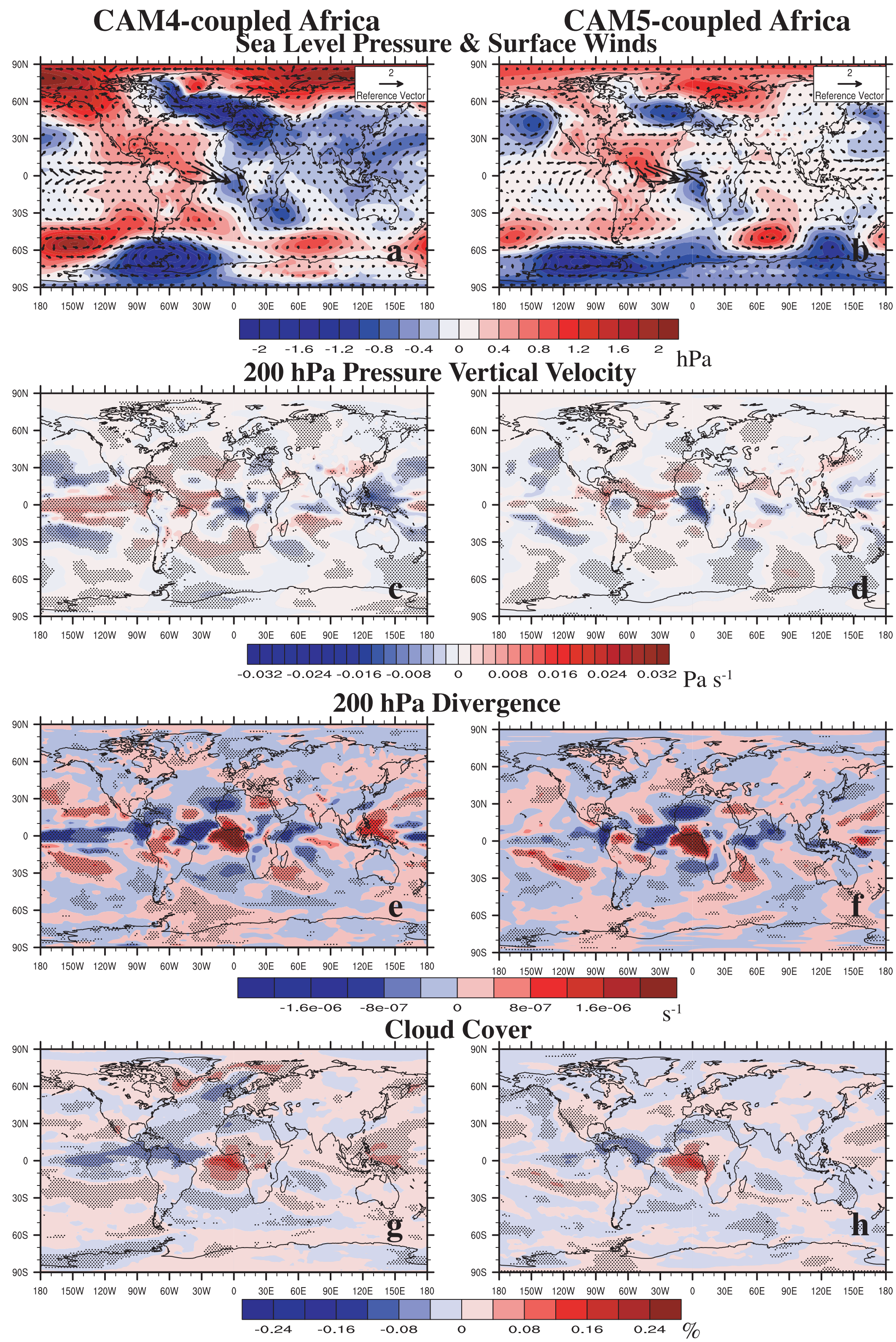

Figure 7. Annual mean dynamical responses including (a,b) sea level pressure (SLP) and surface winds; (c,d) 200 hPa pressure vertical velocity (Ω); (e,f) 200 hPa divergence; and (g,h) cloud cover for (left panels) CAM4-coupled Africa and (right panels) CAM5-coupled Africa. These experiments show the climate response to semi-empirical fine-mode aerosol direct radiative effect without dust and sea salt over Africa only using coupled ocean-atmosphere simulations. SLP and surface wind units in (a,b) are hPa and m s^{-1}, respectively. Ω, divergence, and cloud cover units are Pa s^{-1}, s^{-1} and %, respectively. Symbols denote significance at 90% confidence level, based on a t-test for the difference of means using the pooled variance.

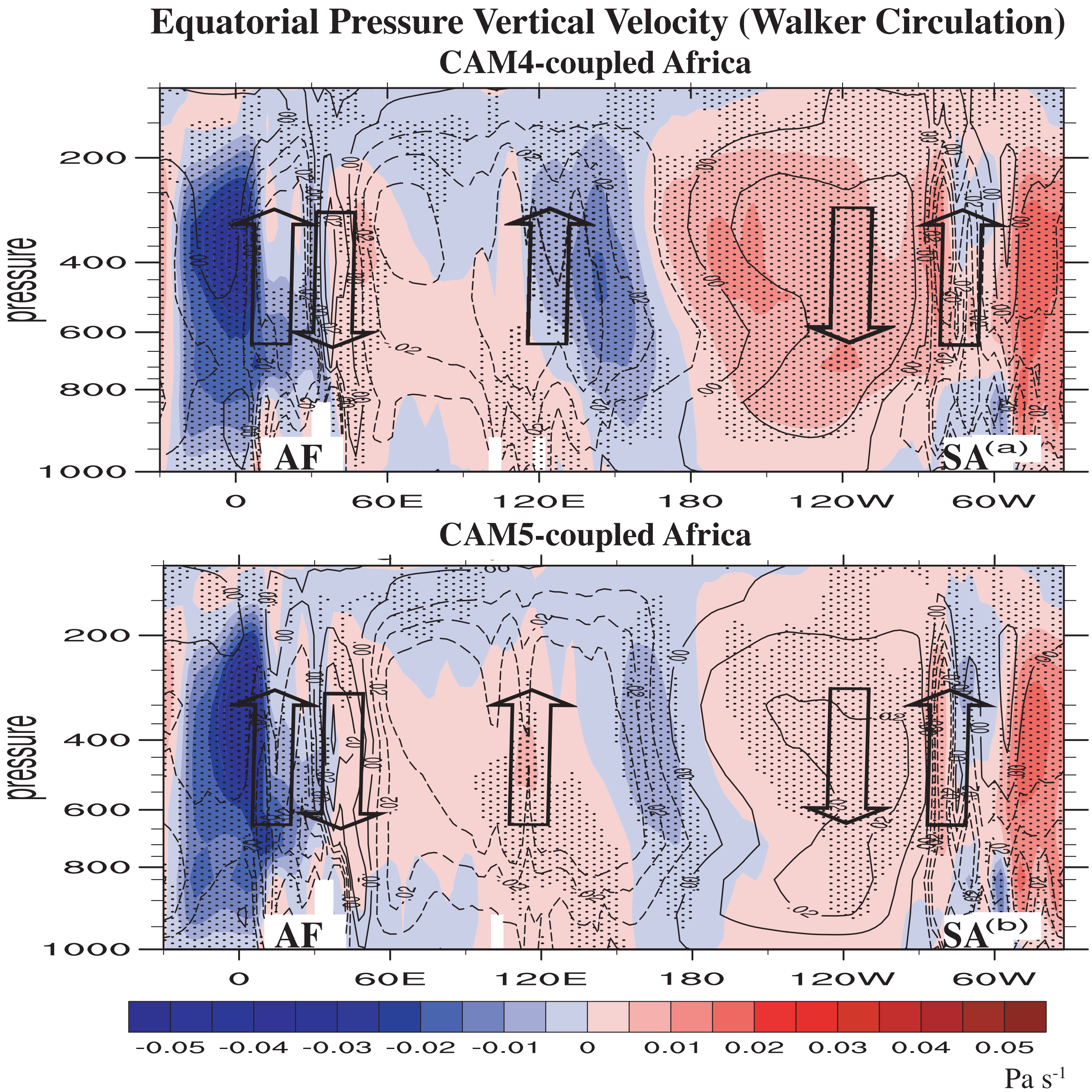

Figure 8. Annual mean vertical cross section of the pressure vertical velocity (Ω) response at the equator for (a) CAM4-coupled Africa and (b) CAM5-coupled Africa. These experiments show the climate response to semi-empirical fine-mode aerosol direct radiative effect without dust and sea salt over Africa only using coupled ocean-atmosphere simulations. Large black arrows represent the climatological Walker circulation in the Pacific and Atlantic. Symbols denote significance at 90% confidence level, based on a *t*-test for the difference of means using the pooled variance. Black contours show the climatological vertical velocity, with negative values (rising air) dashed. To help orient the viewer, Africa (AF) and South America (SA) are labeled. Units are Pa s^{-1}.

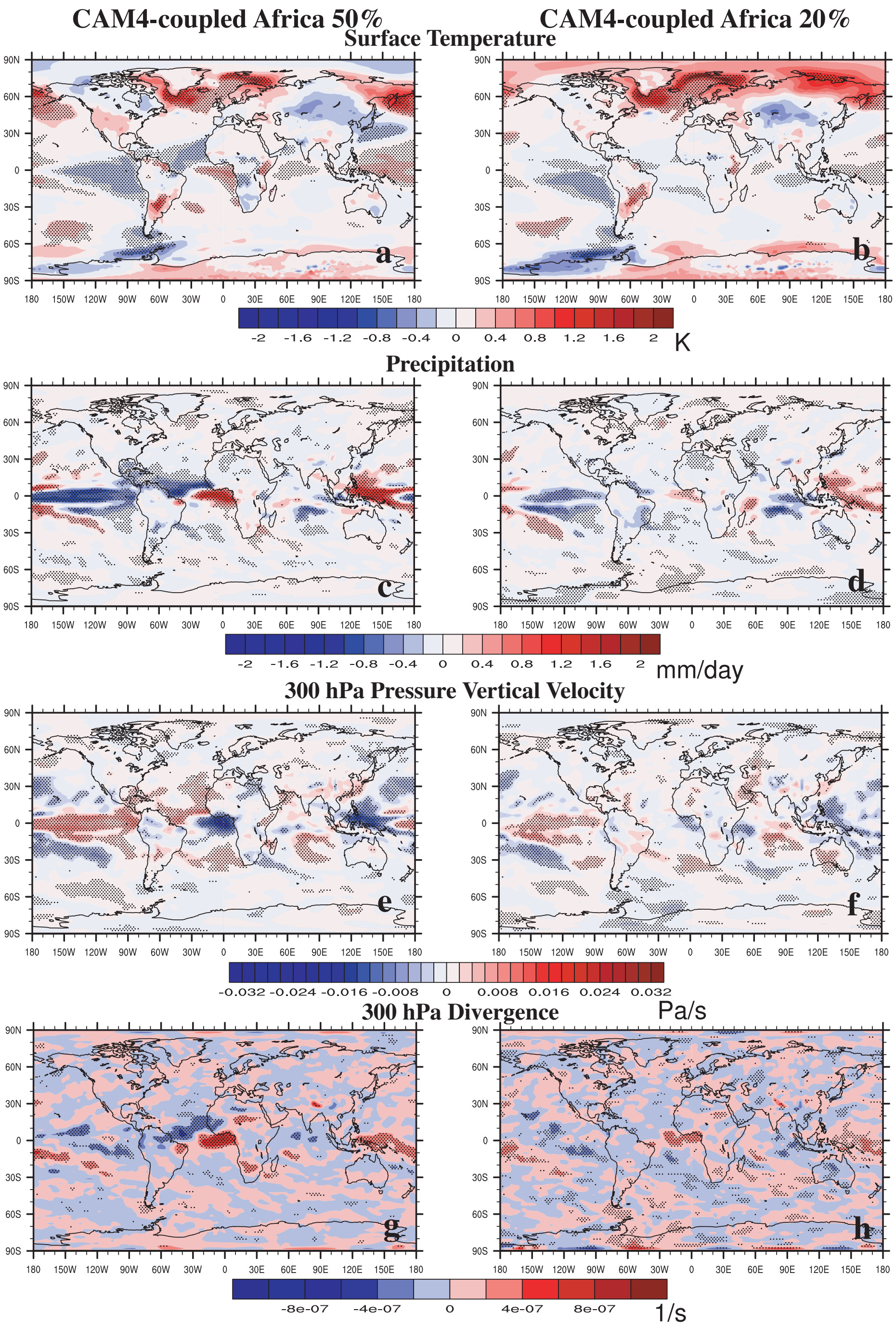

Figure 9. Annual mean (a,b) surface temperature; (c,d) precipitation; (e,f) 300 hPa pressure vertical velocity (Ω); and (g,h) 300 hPa divergence response for (left panels) CAM4-coupled Africa 50% and (right panels) CAM4-coupled Africa 20%. These experiments show the climate response to semi-empirical fine-mode aerosol direct radiative effect without dust and sea salt over Africa only scaled by 50% and 20%, respectively, using coupled ocean-atmosphere simulations. Symbols denote significance at 90% confidence level, based on a *t*-test for the difference of means using the pooled variance. Units are K, mm day^{-1}, Pa s^{-1} and s^{-1} for surface temperature, precipitation, Ω and divergence, respectively. The global annual mean change in surface temperature is 0.042 K for CAM4-coupled Africa 50% and 0.058 K for CAM4-coupled Africa 20% (not significant at the 90% confidence level). The corresponding global annual mean change in precipitation is −0.006 and −0.005 mm day^{-1}, respectively (not significant at the 90% confidence level).

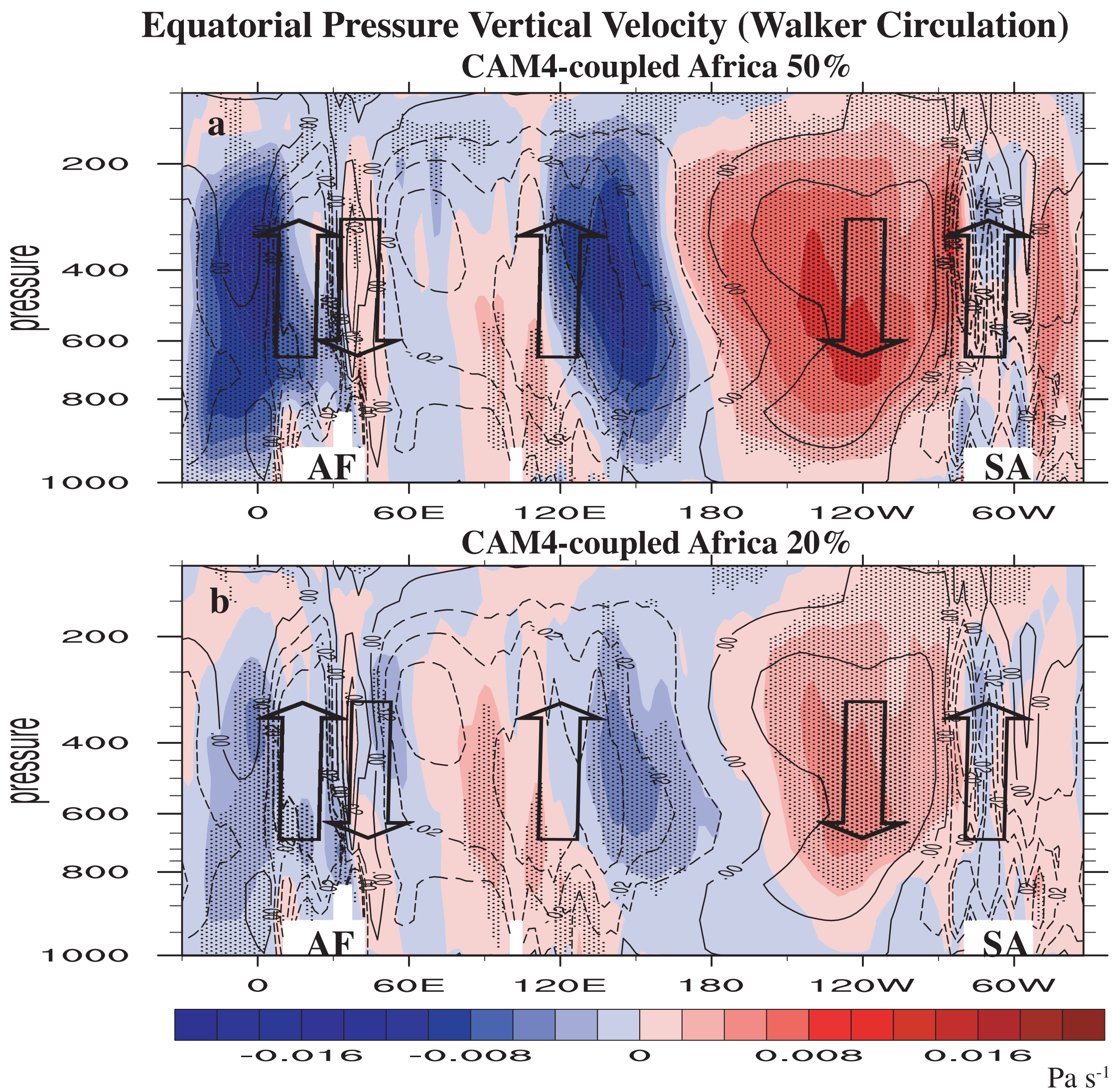

Figure 10. Annual mean vertical cross section of the pressure vertical velocity (Ω) response at the equator for (a) CAM4-coupled Africa 50% and (b) CAM4-coupled Africa 20%. These experiments show the climate response to semi-empirical fine-mode aerosol direct radiative effect without dust and sea salt over Africa only scaled by 50% and 20%, respectively, using coupled ocean-atmosphere simulations. Large black arrows represent the climatological Walker circulation in the Pacific and Atlantic. Symbols denote significance at 90% confidence level, based on a t-test for the difference of means using the pooled variance. Black contours show the climatological vertical velocity, with negative values (rising air) dashed. To help orient the viewer, Africa (AF) and South America (SA) are labeled. Units are Pa s^{-1}.

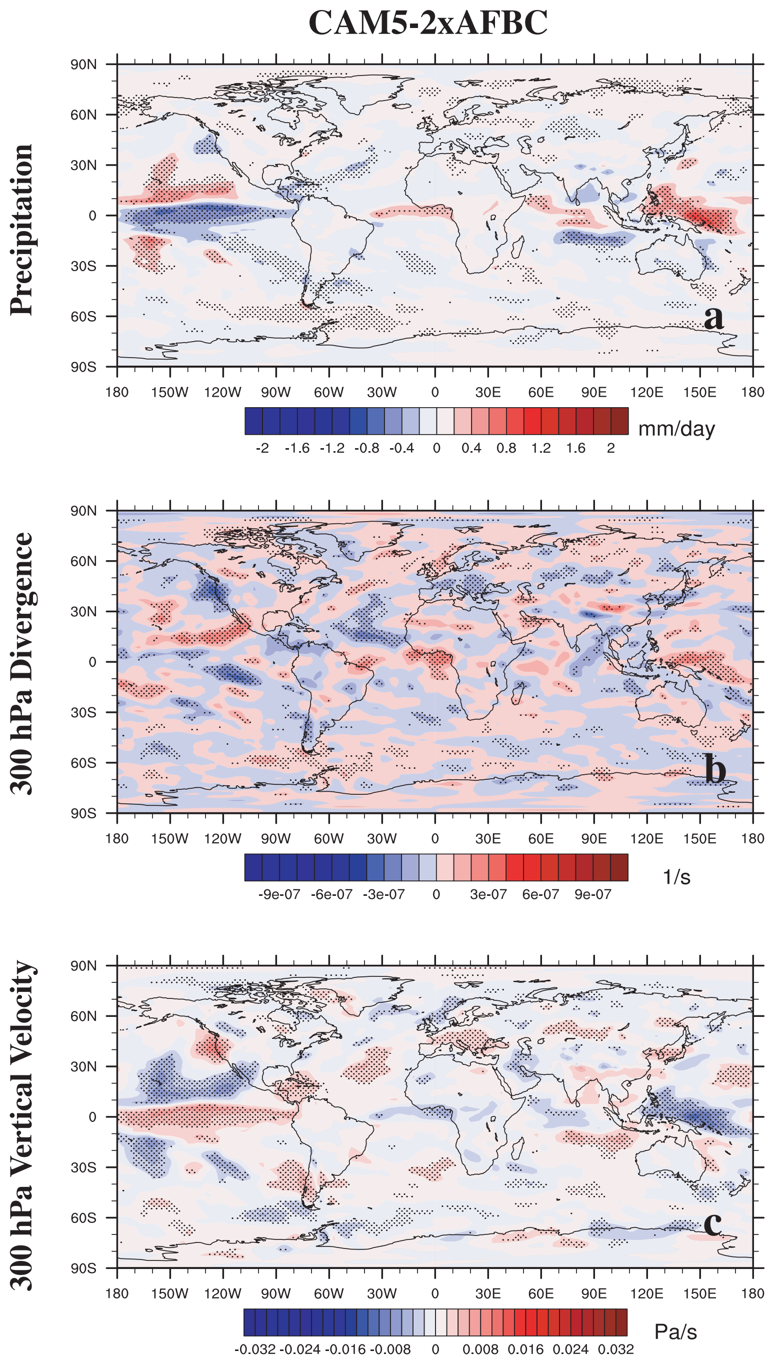

Figure 11. Annual mean (a) precipitation; (b) 300 hPa pressure vertical velocity (Ω); and (c) 300 hPa divergence response for CAM5-2xAFBC This experiment shows the climate response to doubling MAM3 1850 BC fire emissions over Africa, using a coupled ocean-atmosphere simulation. Symbols denote significance at 90% confidence level, based on a *t*-test for the difference of means using the pooled variance. Units are mm day^{-1}, s^{-1} and Pa s^{-1} for precipitation, divergence and Ω respectively.

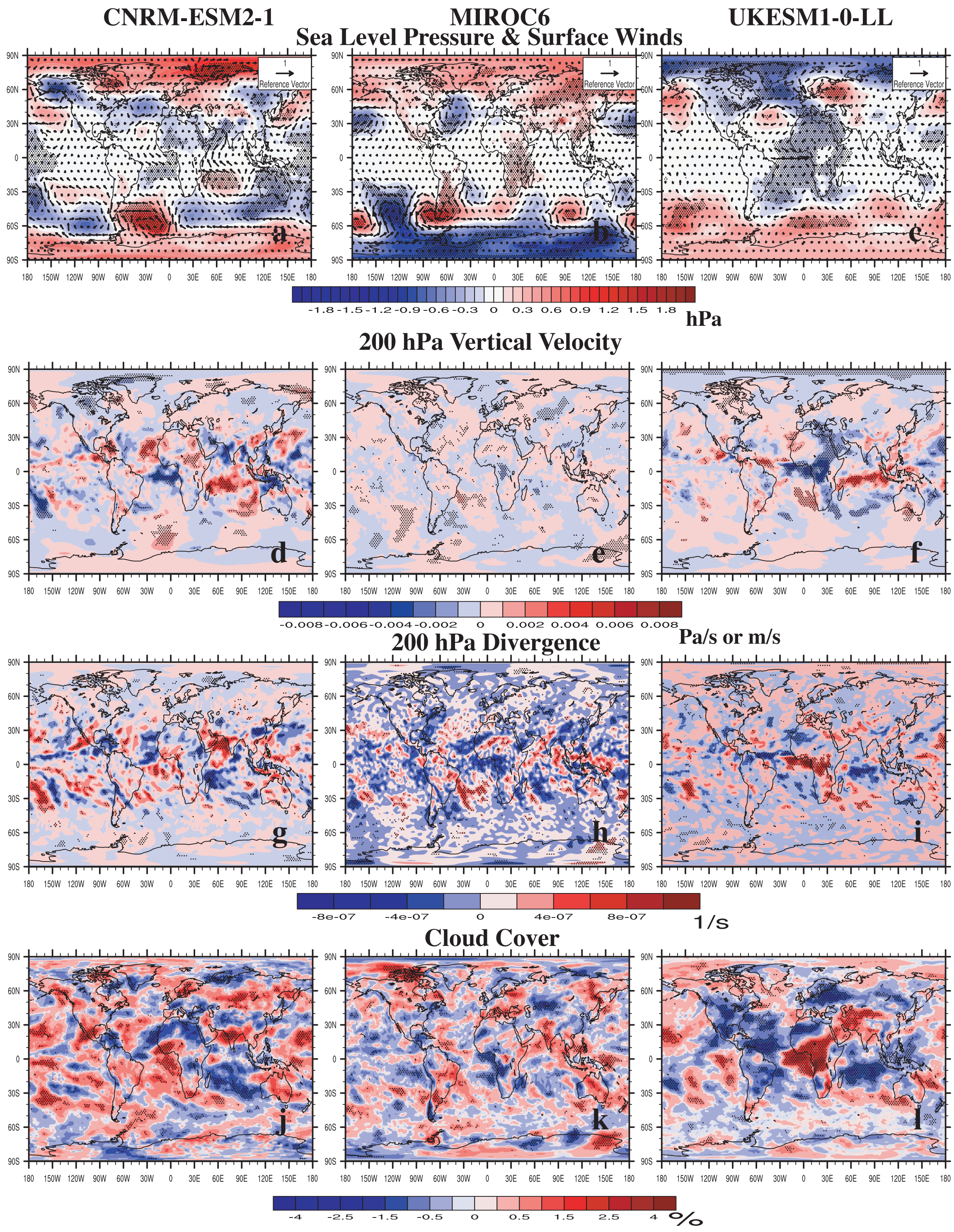

Figure 12. CMIP6 2xFIRE annual mean dynamical responses including (a-c) sea level pressure (SLP) and surface winds; (d-f) 200 hPa vertical velocity; (g-i) 200 hPa divergence; and (j-l) cloud cover for (left panels) CNRM-ESM2-1; (center panels) MIROC6; and (right panels) UKESM1-0-LL. As with all other figures, CNRM-ESM2-1 and UKESM1-0-LL vertical velocity is based on pressure vertical velocity, with units of Pa s^{-1}. However, MIROC6 vertical velocity is based on standard vertical velocity, with units of m s^{-1}. SLP and surface wind units in (a-c) are hPa and m s^{-1}, respectively. Divergence and cloud cover units are s^{-1}, and %, respectively. Symbols denote significance at 90% confidence level, based on a *t*-test for the difference of means using the pooled variance.

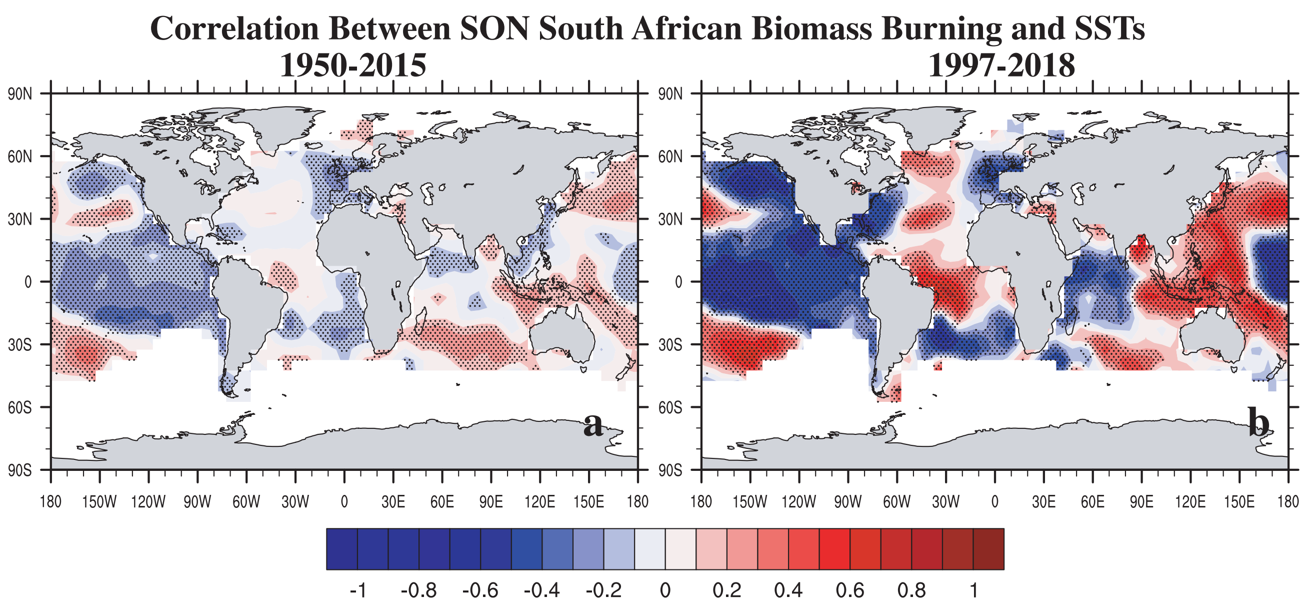

Figure 13. Detrended September-October-November (SON) spatial correlation map between south African biomass burning emissions and Kaplan sea surface temperatures (SSTs) for (a) 1950-2015 and (b) 1997-2018. GFED4s (CMIP6) data is used for 1997-2018 (1950-2015) biomass burning emissions. Symbols denote significance at 90% confidence level based on a t-test.

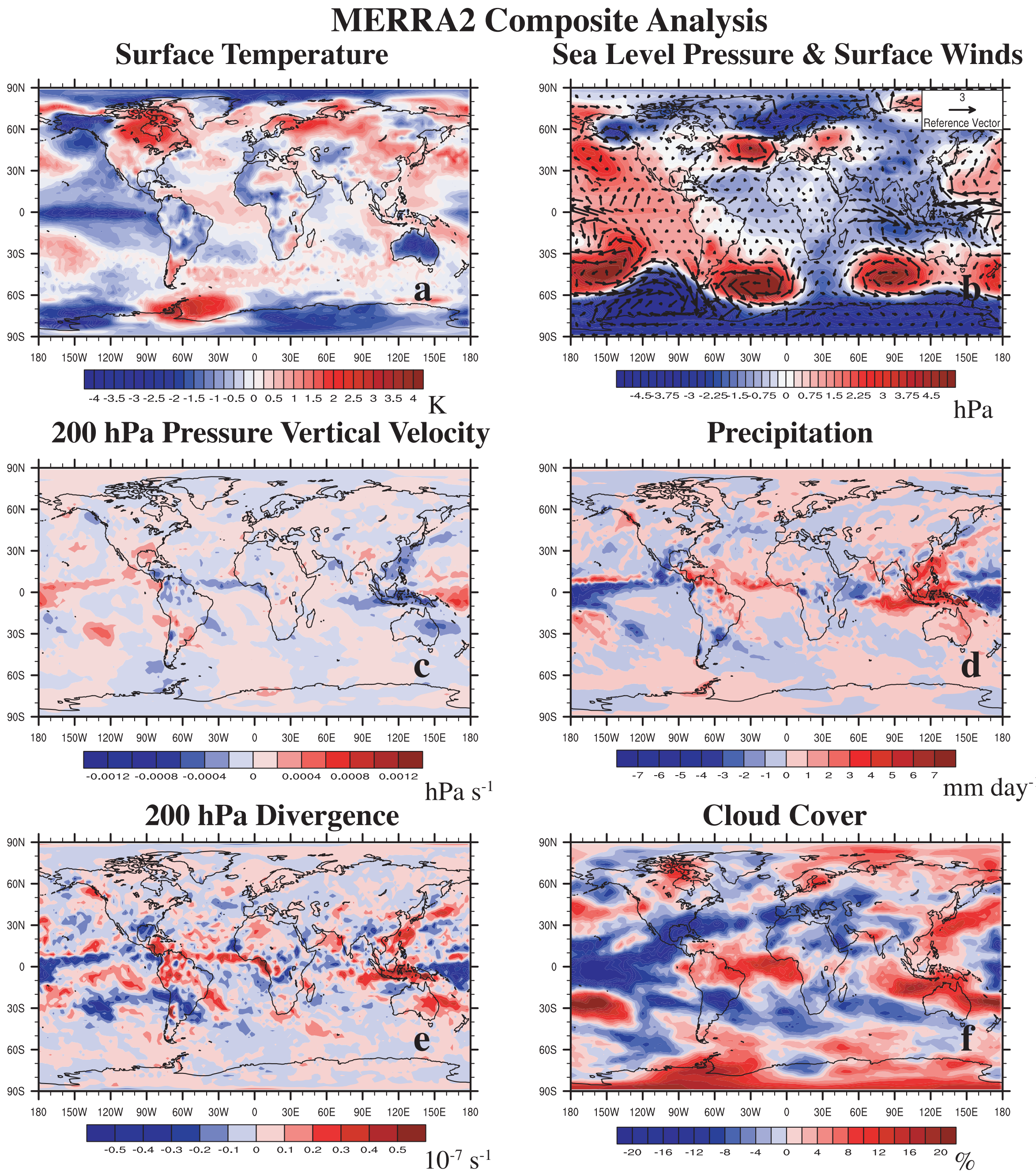

Figure 14. MERRA2 September-October-November (SON) composite analysis (high minus low fire years) of dynamical responses including (a) surface temperature; (b) sea level pressure (SLP) and surface winds; (c) 200 hPa pressure vertical velocity (Ω); (d) precipitation; (e) 200 hPa divergence; and (f) cloud cover. Analysis is based on 1997-2018 SON GFED4s south African biomass burning emissions. Surface temperature, SLP, surface winds, Ω, precipitation, divergence and cloud cover units are K, hPa, m s^{-1}, hPa s^{-1}, mm day^{-1}, 10^{-7} s^{-1}, and %, respectively.

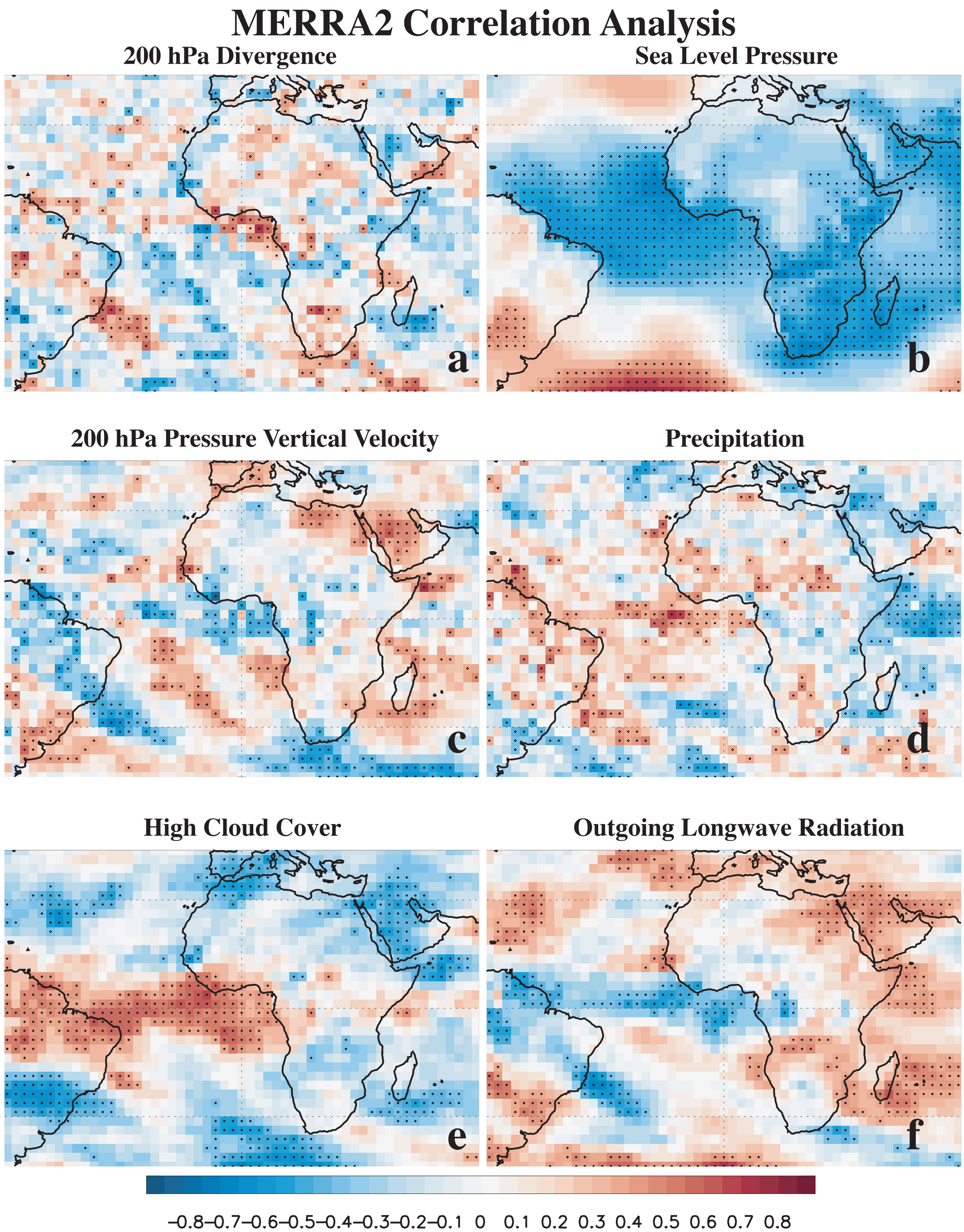

Figure 15. 1997-2018 September-October-November (SON) Atlantic correlations between GFED4s south African biomass burning emissions and MERRA2 (a) 200 hPa divergence; (b) sea level pressure (SLP); (c) 200 hPa pressure vertical velocity (Ω); (d) precipitation; (e) high cloud cover; and (f) outgoing longwave radiation. Black symbols denote correlations that are significant at the 90% confidence level based on a *t*-test. Time series are first detrended before calculation of the correlation. Units are dimensionless.

Figure 1.

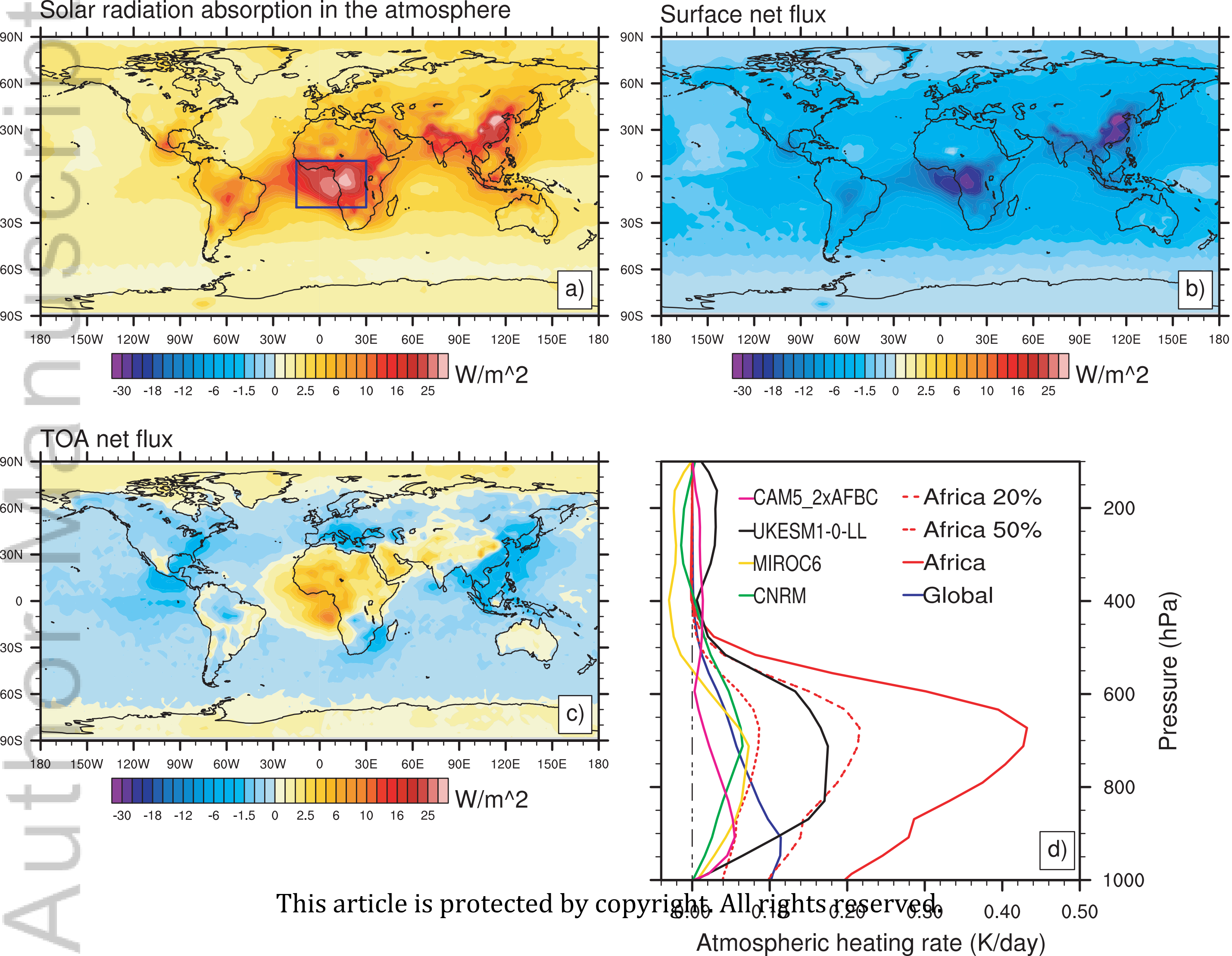

Solar radiation absorption in the atmosphere
a)
Surface net flux
b)
TOA net flux
c)
W/m^2
CAM5_2xAFBC
UKESM1-0-LL
MIROC6
CNRM
Africa 20%
Africa 50%
Africa
Global
d)
Pressure (hPa)
Atmospheric heating rate (K/day)

Figure 2.

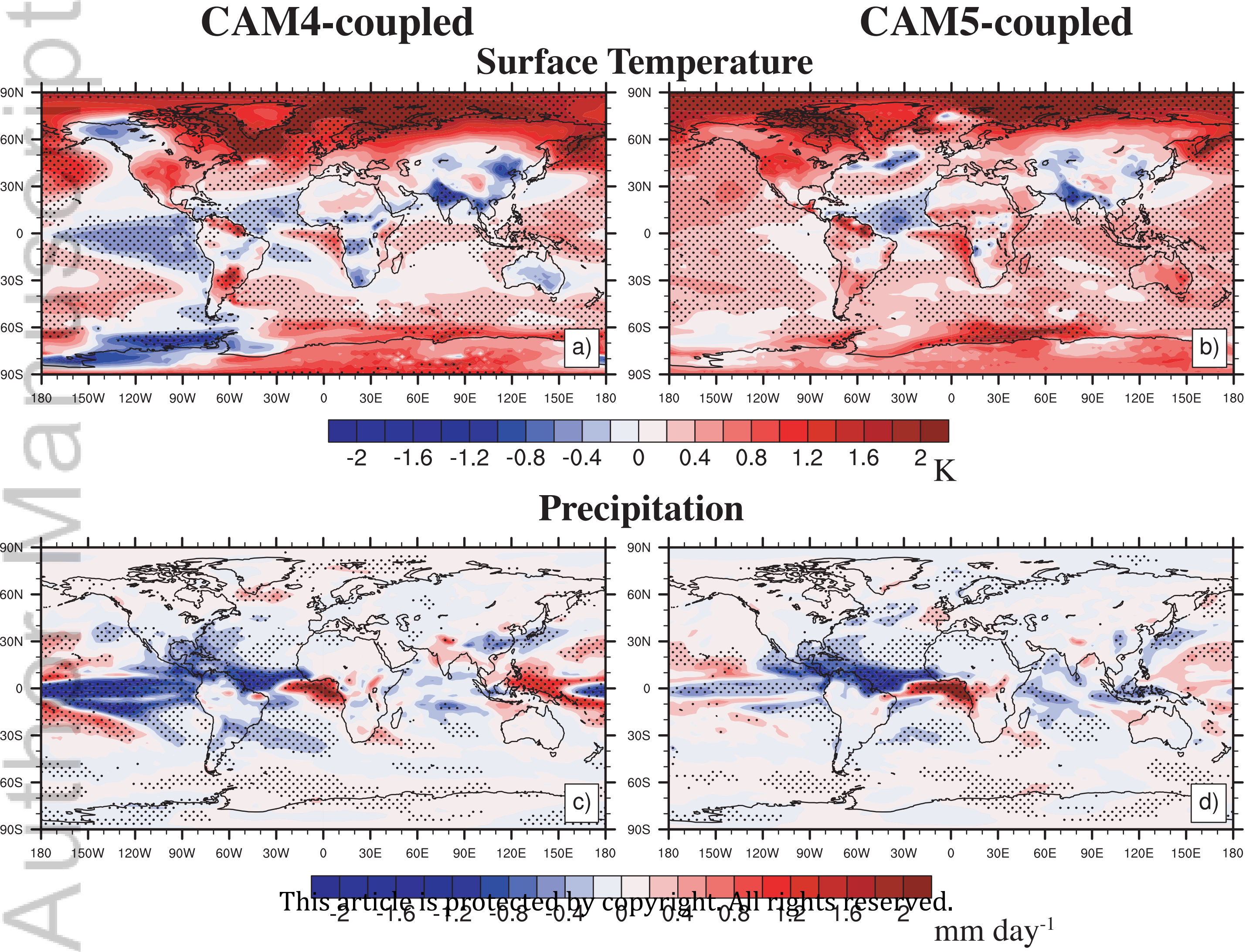
CAM4-coupled
CAM5-coupled
Surface Temperature
90N
60N
30N
0
30S
60S
90S
180
150W
120W
90W
60W
30W
0
30E
60E
90E
120E
150E
180
a)
b)
-2
-1.6
-1.2
-0.8
-0.4
0
0.4
0.8
1.2
1.6
2
K
Precipitation
c)
d)
mm day-1

Figure 3.

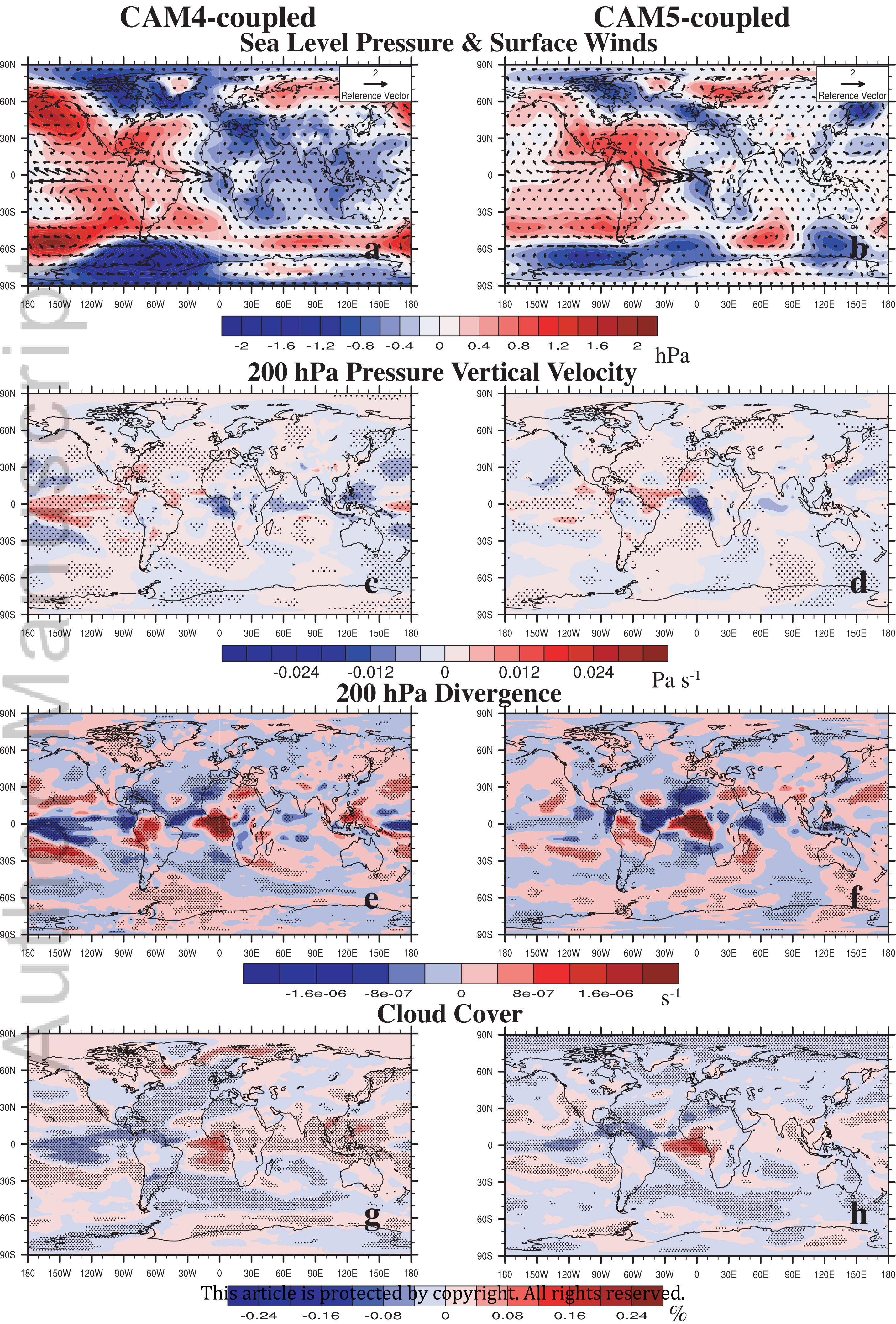

CAM4-coupled
CAM5-coupled
Sea Level Pressure & Surface Winds
Reference Vector
2
a
b
hPa
200 hPa Pressure Vertical Velocity
c
d
Pa s-1
200 hPa Divergence
e
f
s-1
Cloud Cover
g
h
%

Figure 4.

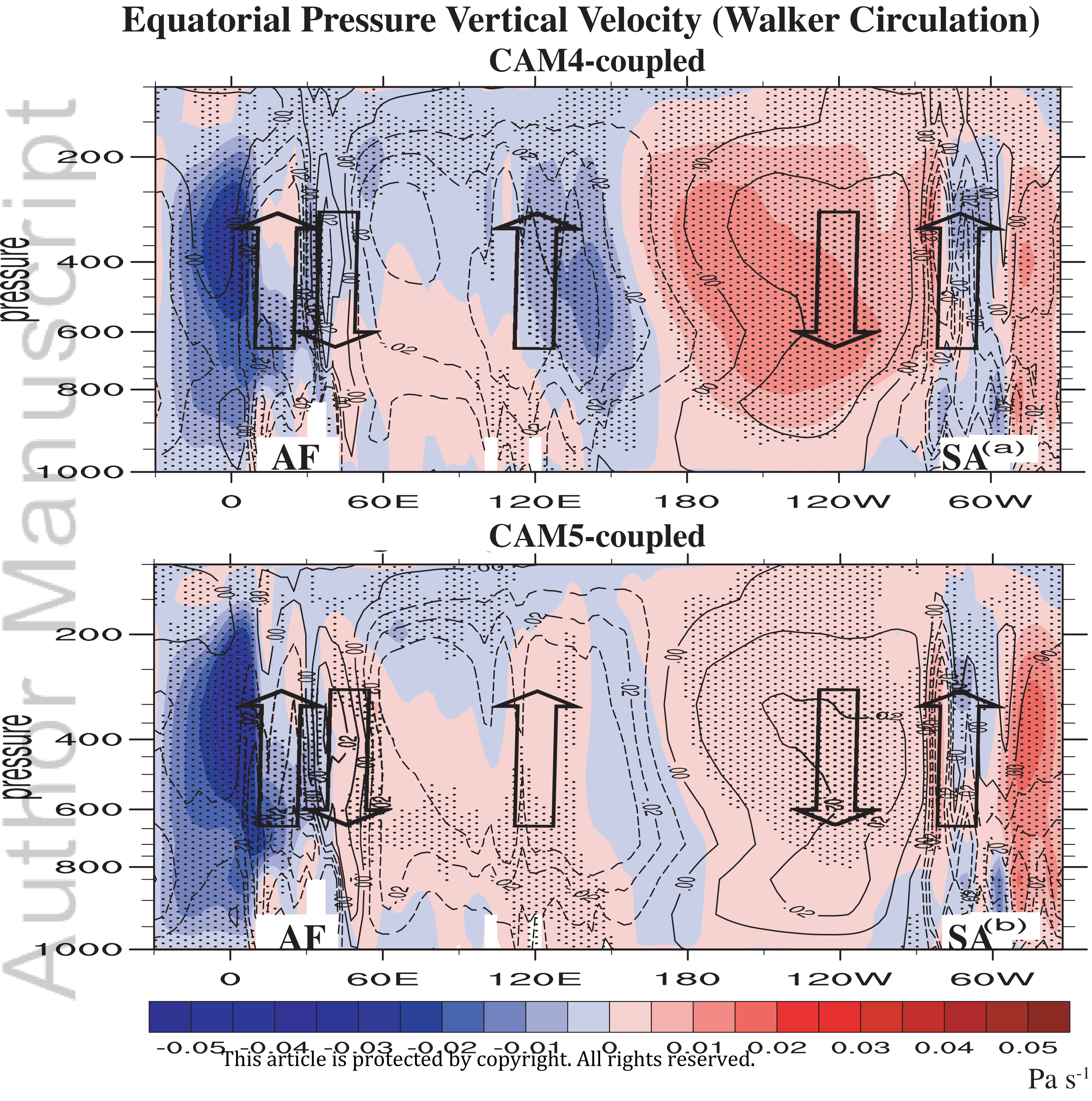
Equatorial Pressure Vertical Velocity (Walker Circulation)
CAM4-coupled
pressure
200
400
600
800
1000
0
60E
120E
180
120W
60W
AF
SA
(a)
CAM5-coupled
(b)
-0.05
-0.04
-0.03
-0.02
-0.01
0
0.01
0.02
0.03
0.04
0.05
Pa s-1

Figure 5.

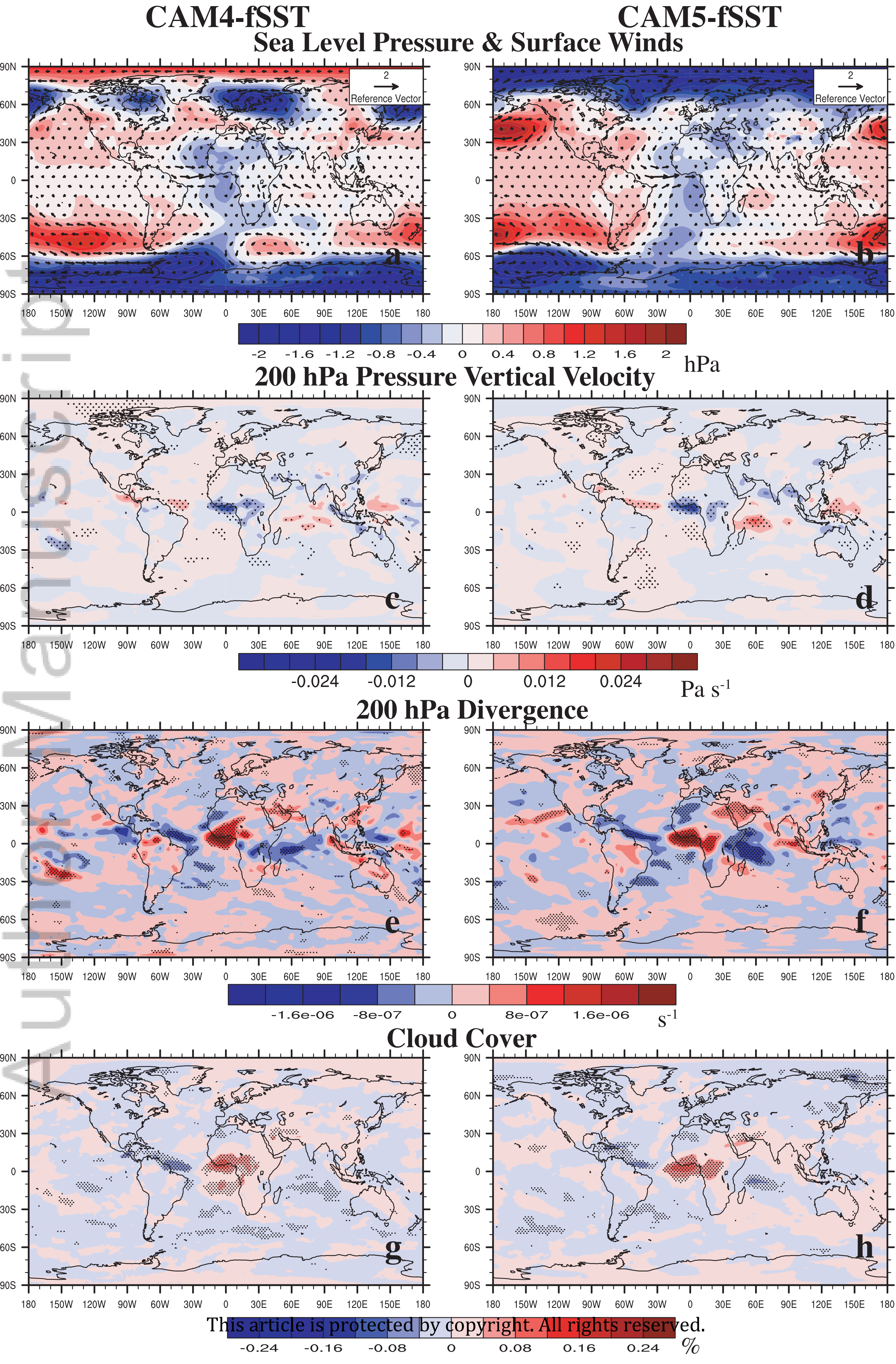

CAM4-fSST
CAM5-fSST
Sea Level Pressure & Surface Winds
2
Reference Vector
a
b
hPa
200 hPa Pressure Vertical Velocity
c
d
Pa s-1
200 hPa Divergence
e
f
s-1
Cloud Cover
g
h
%

Figure 6.

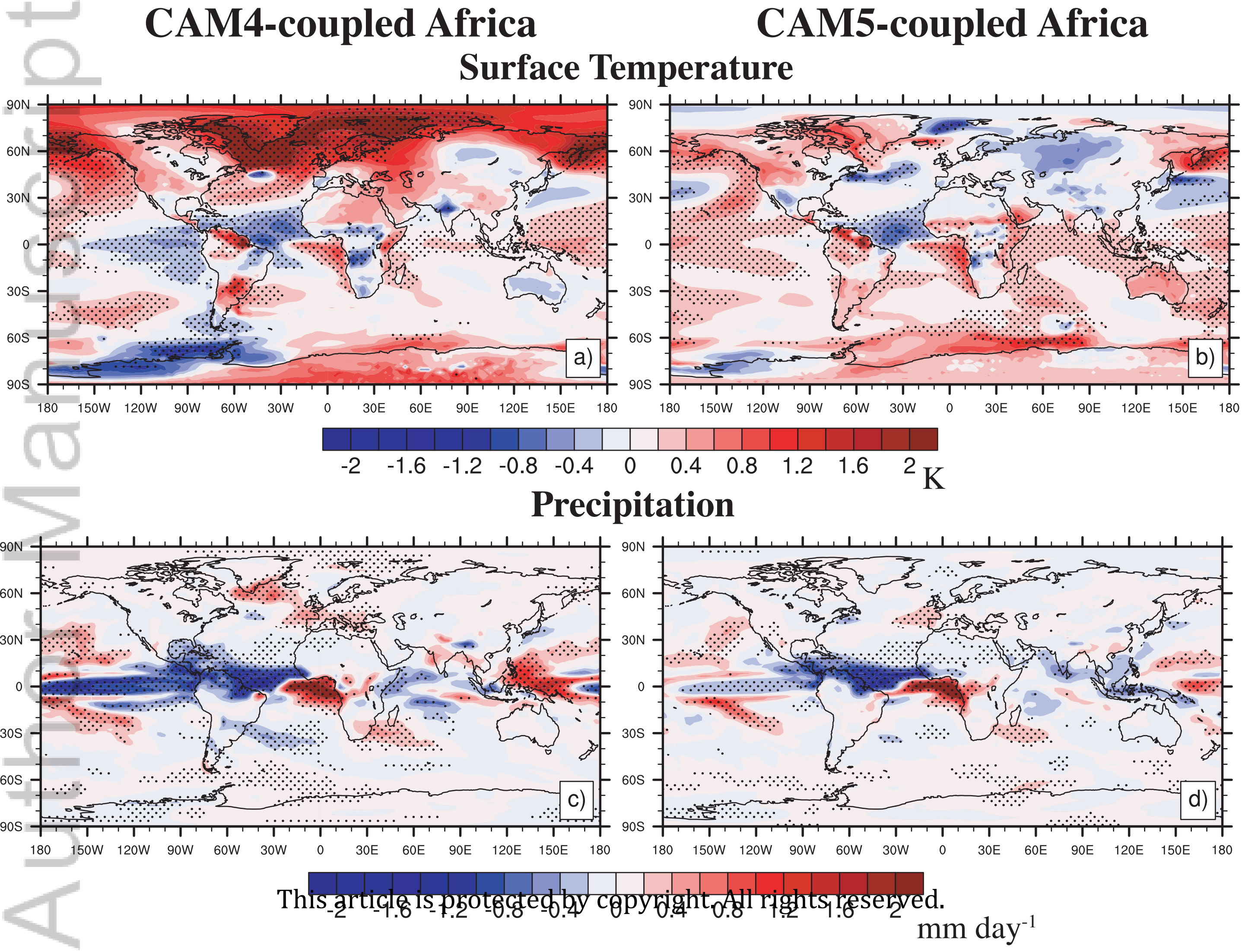
CAM4-coupled Africa
CAM5-coupled Africa
Surface Temperature
90N
60N
30N
0
30S
60S
90S
180
150W
120W
90W
60W
30W
0
30E
60E
90E
120E
150E
180
a)
b)
-2
-1.6
-1.2
-0.8
-0.4
0
0.4
0.8
1.2
1.6
2
K
Precipitation
c)
d)
mm day-1

Figure 7.

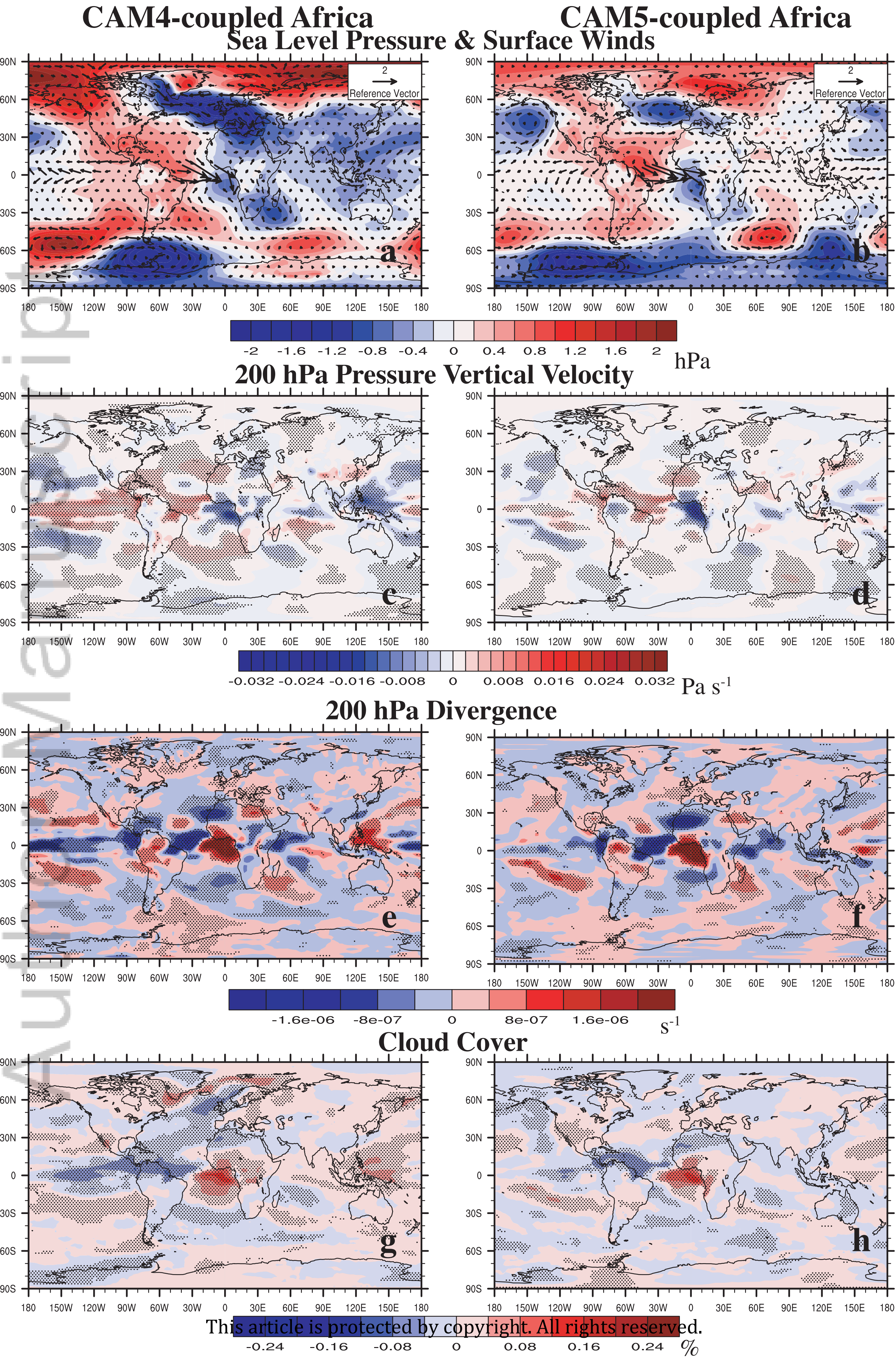

CAM4-coupled Africa
CAM5-coupled Africa
Sea Level Pressure & Surface Winds
2
Reference Vector
a
b
-2 -1.6 -1.2 -0.8 -0.4 0 0.4 0.8 1.2 1.6 2
hPa
200 hPa Pressure Vertical Velocity
c
d
-0.032 -0.024 -0.016 -0.008 0 0.008 0.016 0.024 0.032
Pa s-1
200 hPa Divergence
e
f
-1.6e-06 -8e-07 0 8e-07 1.6e-06
s-1
Cloud Cover
g
h
-0.24 -0.16 -0.08 0 0.08 0.16 0.24
%
90N 60N 30N 0 30S 60S 90S
180 150W 120W 90W 60W 30W 0 30E 60E 90E 120E 150E 180

Figure 8.

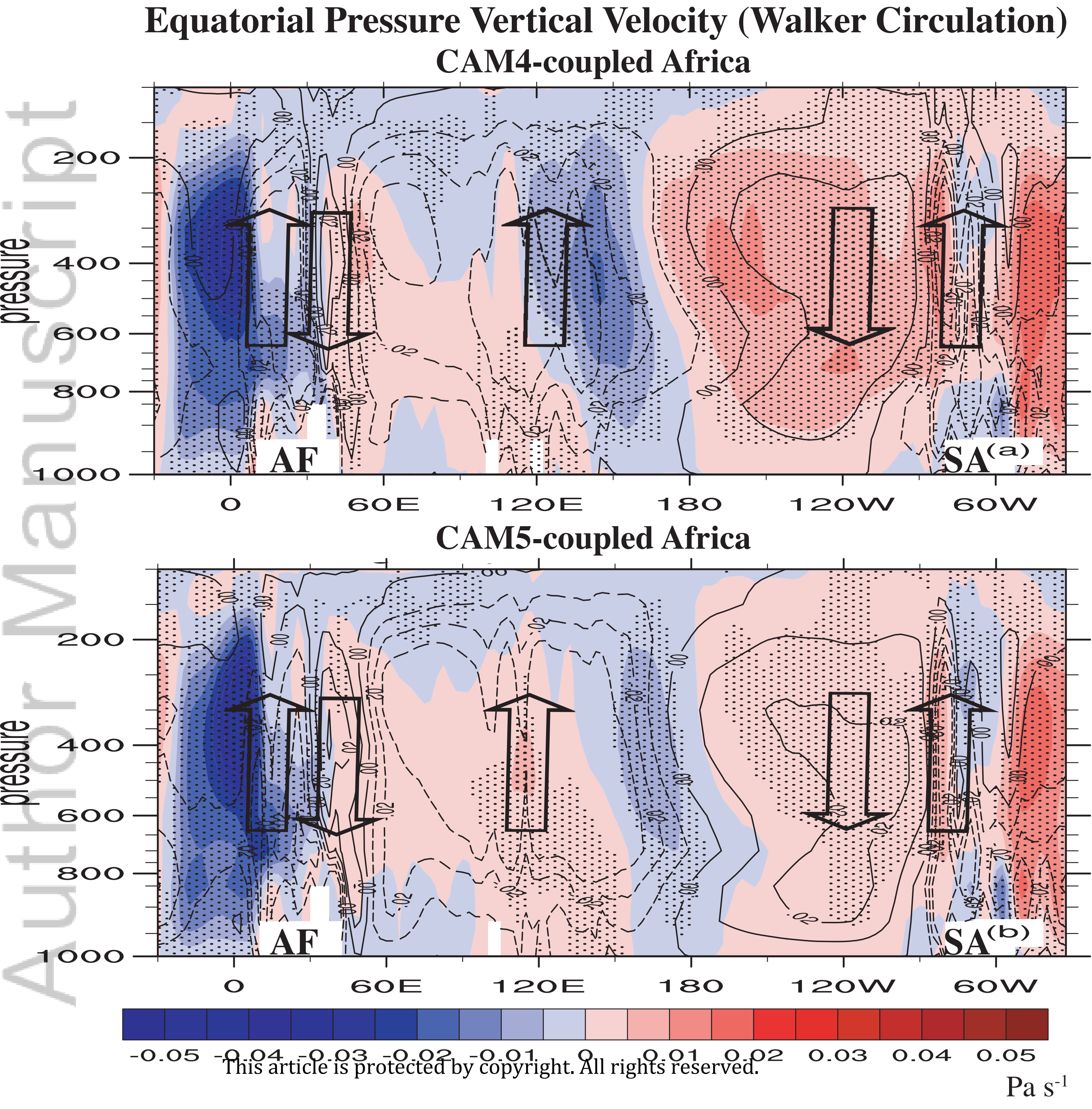

Equatorial Pressure Vertical Velocity (Walker Circulation)
CAM4-coupled Africa
pressure
200
400
600
800
1000
0
60E
120E
180
120W
60W
AF
SA(a)
CAM5-coupled Africa
AF
SA(b)
-0.05
-0.04
-0.03
-0.02
-0.01
0
0.01
0.02
0.03
0.04
0.05
Pa s-1

Figure 9.

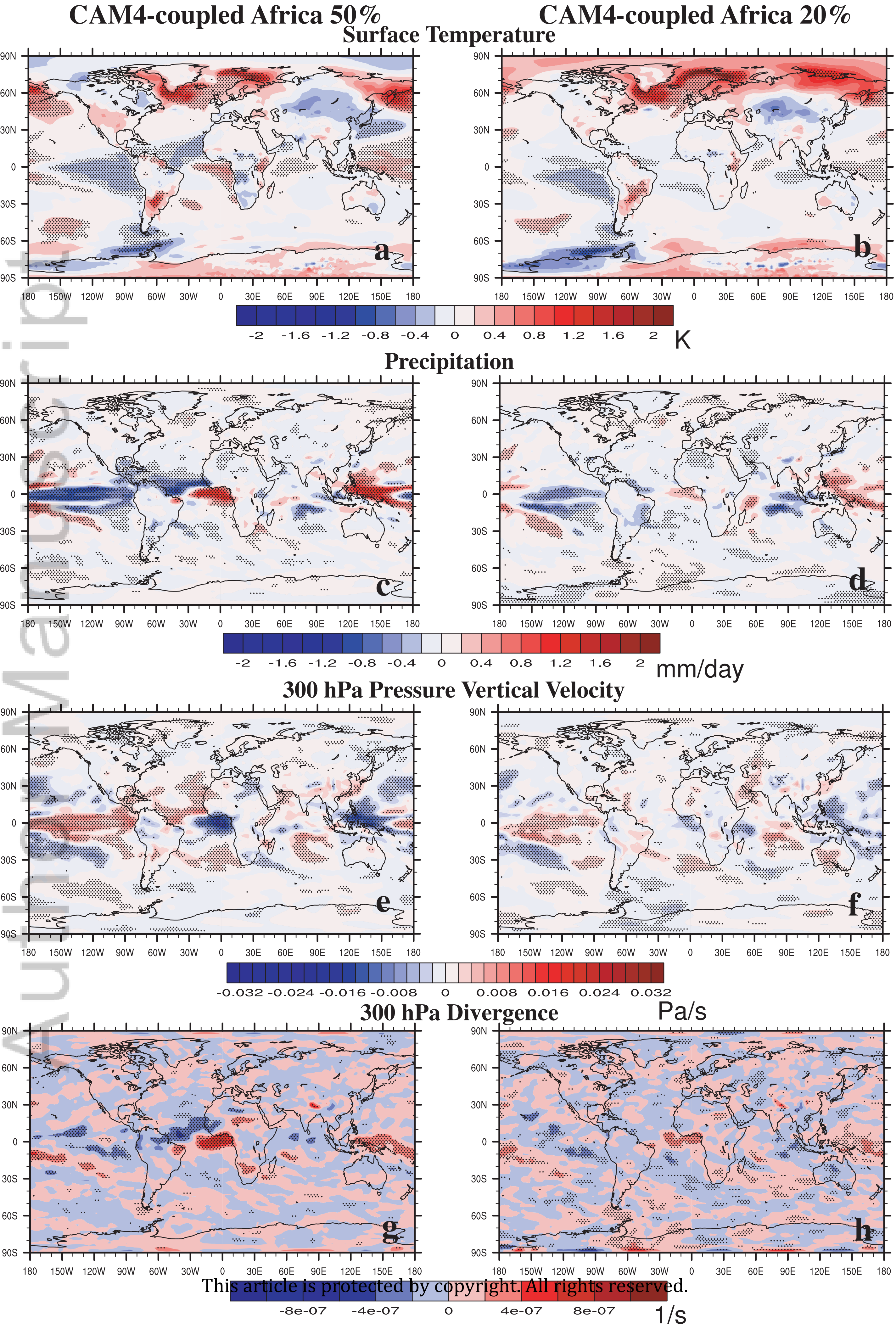
CAM4-coupled Africa 50%
CAM4-coupled Africa 20%
Surface Temperature
90N 60N 30N 0 30S 60S 90S
180 150W 120W 90W 60W 30W 0 30E 60E 90E 120E 150E 180
a
b
-2 -1.6 -1.2 -0.8 -0.4 0 0.4 0.8 1.2 1.6 2
K
Precipitation
c
d
-2 -1.6 -1.2 -0.8 -0.4 0 0.4 0.8 1.2 1.6 2
mm/day
300 hPa Pressure Vertical Velocity
e
f
-0.032 -0.024 -0.016 -0.008 0 0.008 0.016 0.024 0.032
Pa/s
300 hPa Divergence
g
h
-8e-07 -4e-07 0 4e-07 8e-07
1/s

Figure 10.

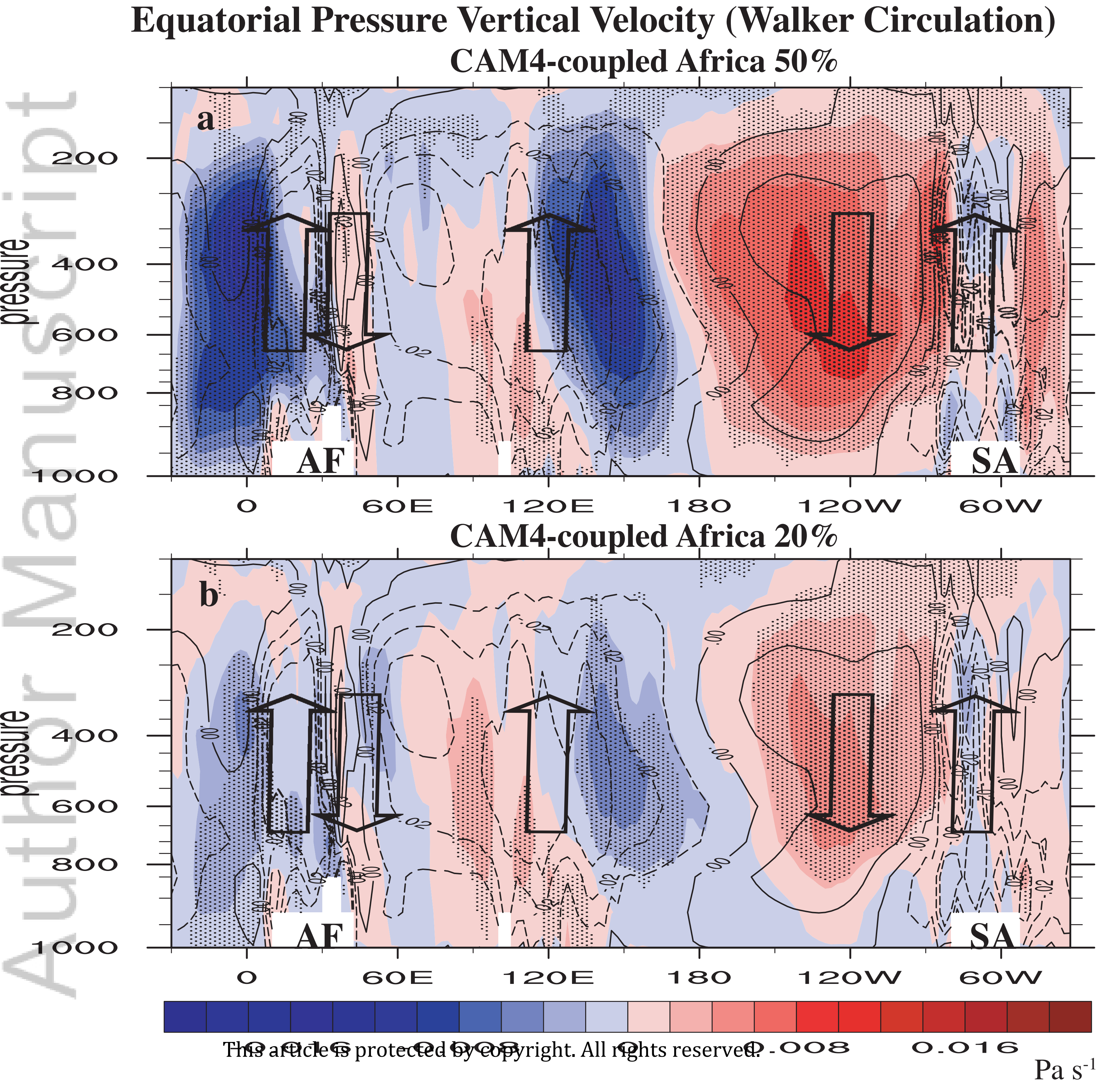
Equatorial Pressure Vertical Velocity (Walker Circulation)
CAM4-coupled Africa 50%
a
pressure
200
400
600
800
1000
AF
SA
0
60E
120E
180
120W
60W
CAM4-coupled Africa 20%
b
-0.016
-0.008
0
0.008
0.016
Pa s-1

Figure 11.

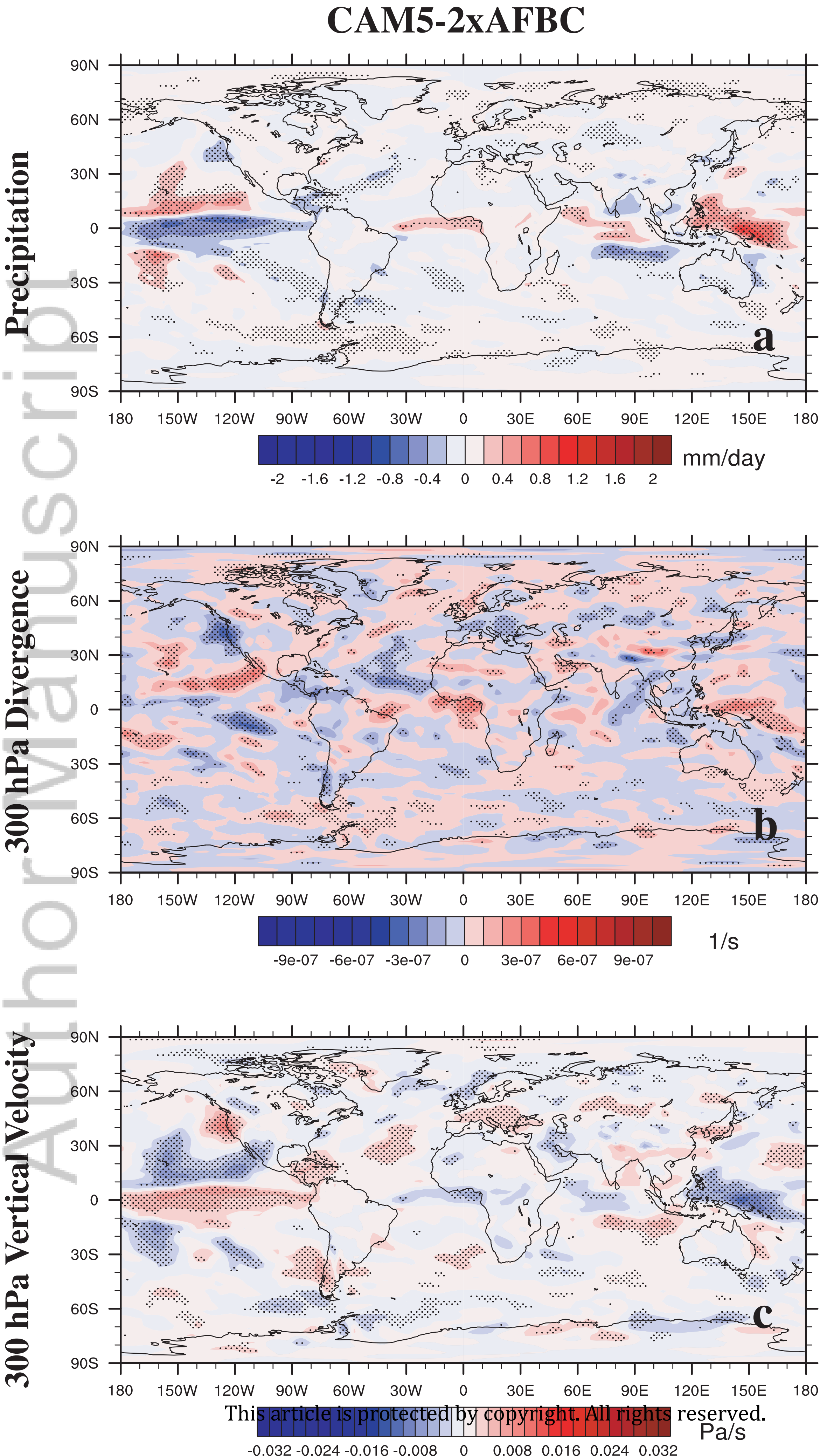

CAM5-2xAFBC
Precipitation
a
mm/day
-2 -1.6 -1.2 -0.8 -0.4 0 0.4 0.8 1.2 1.6 2
300 hPa Divergence
b
1/s
-9e-07 -6e-07 -3e-07 0 3e-07 6e-07 9e-07
300 hPa Vertical Velocity
c
Pa/s
-0.032 -0.024 -0.016 -0.008 0 0.008 0.016 0.024 0.032
90N 60N 30N 0 30S 60S 90S
180 150W 120W 90W 60W 30W 0 30E 60E 90E 120E 150E 180

Figure 12.

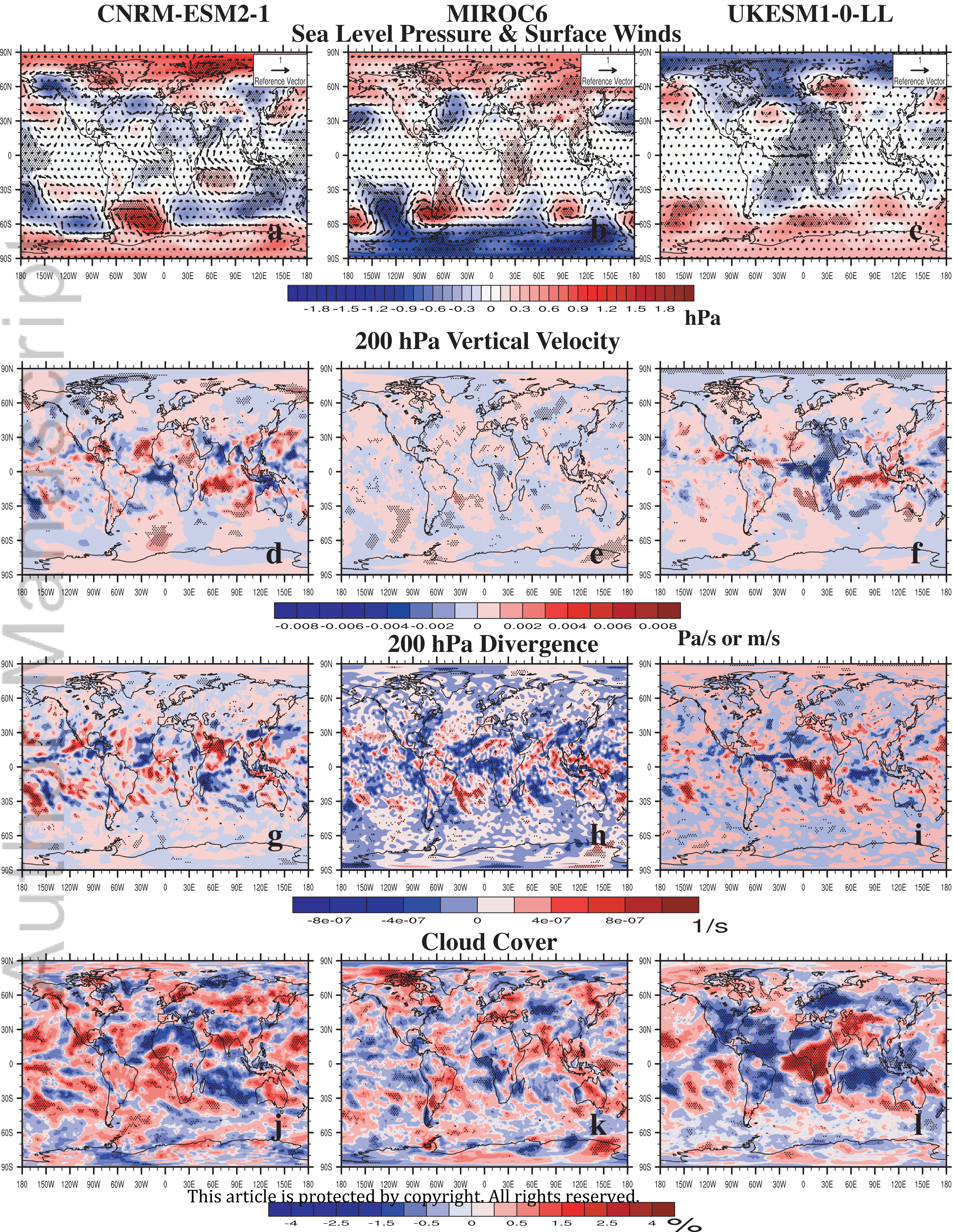
CNRM-ESM2-1
MIROC6
UKESM1-0-LL
Sea Level Pressure & Surface Winds
Reference Vector
a
b
c
-1.8 -1.5 -1.2 -0.9 -0.6 -0.3 0 0.3 0.6 0.9 1.2 1.5 1.8
hPa
200 hPa Vertical Velocity
d
e
f
-0.008 -0.006 -0.004 -0.002 0 0.002 0.004 0.006 0.008
Pa/s or m/s
200 hPa Divergence
g
h
i
-8e-07 -4e-07 0 4e-07 8e-07
1/s
Cloud Cover
j
k
l
-4 -2.5 -1.5 -0.5 0 0.5 1.5 2.5 4
%

Figure 13.

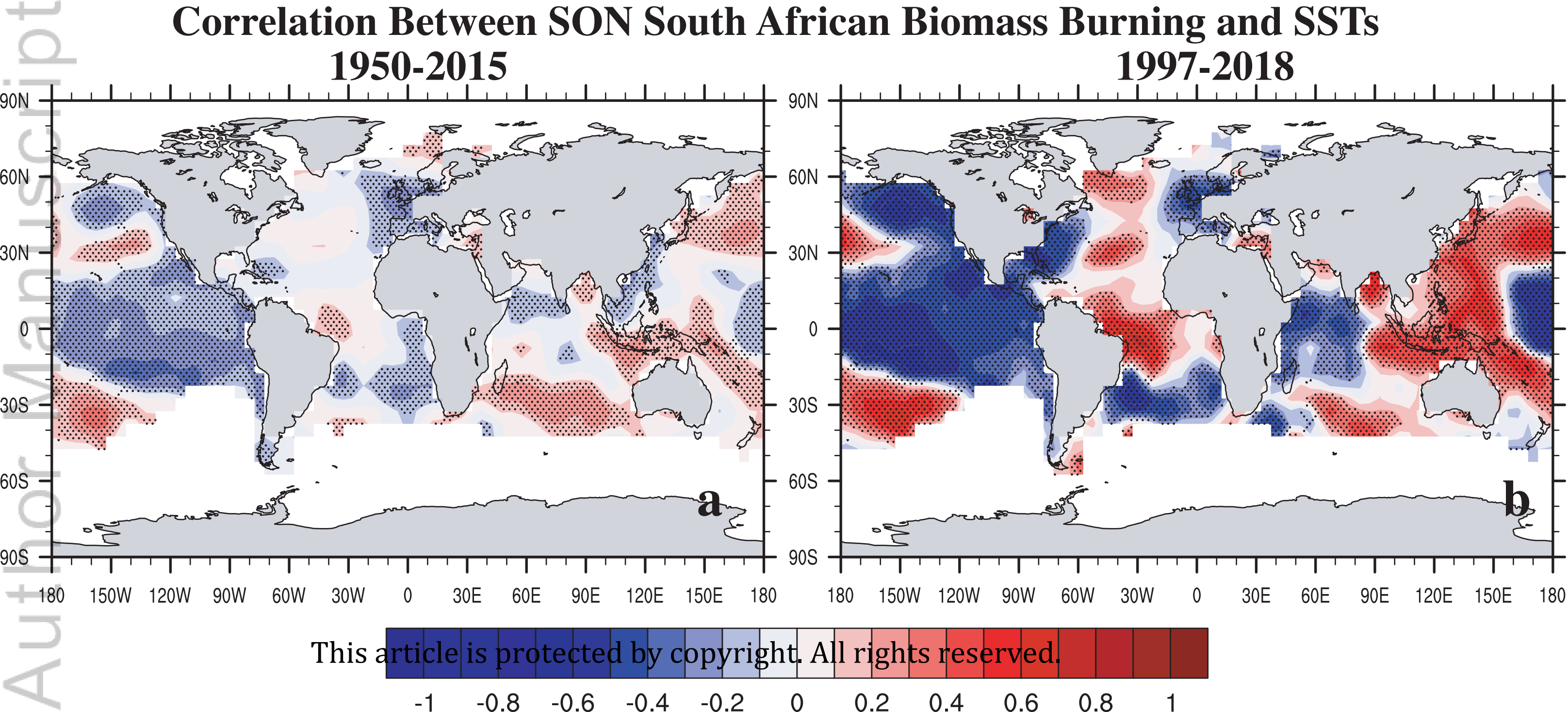
Correlation Between SON South African Biomass Burning and SSTs
1950-2015
1997-2018
90N
60N
30N
0
30S
60S
90S
180
150W
120W
90W
60W
30W
0
30E
60E
90E
120E
150E
180
a
b
-1
-0.8
-0.6
-0.4
-0.2
0
0.2
0.4
0.6
0.8
1

Figure 14.

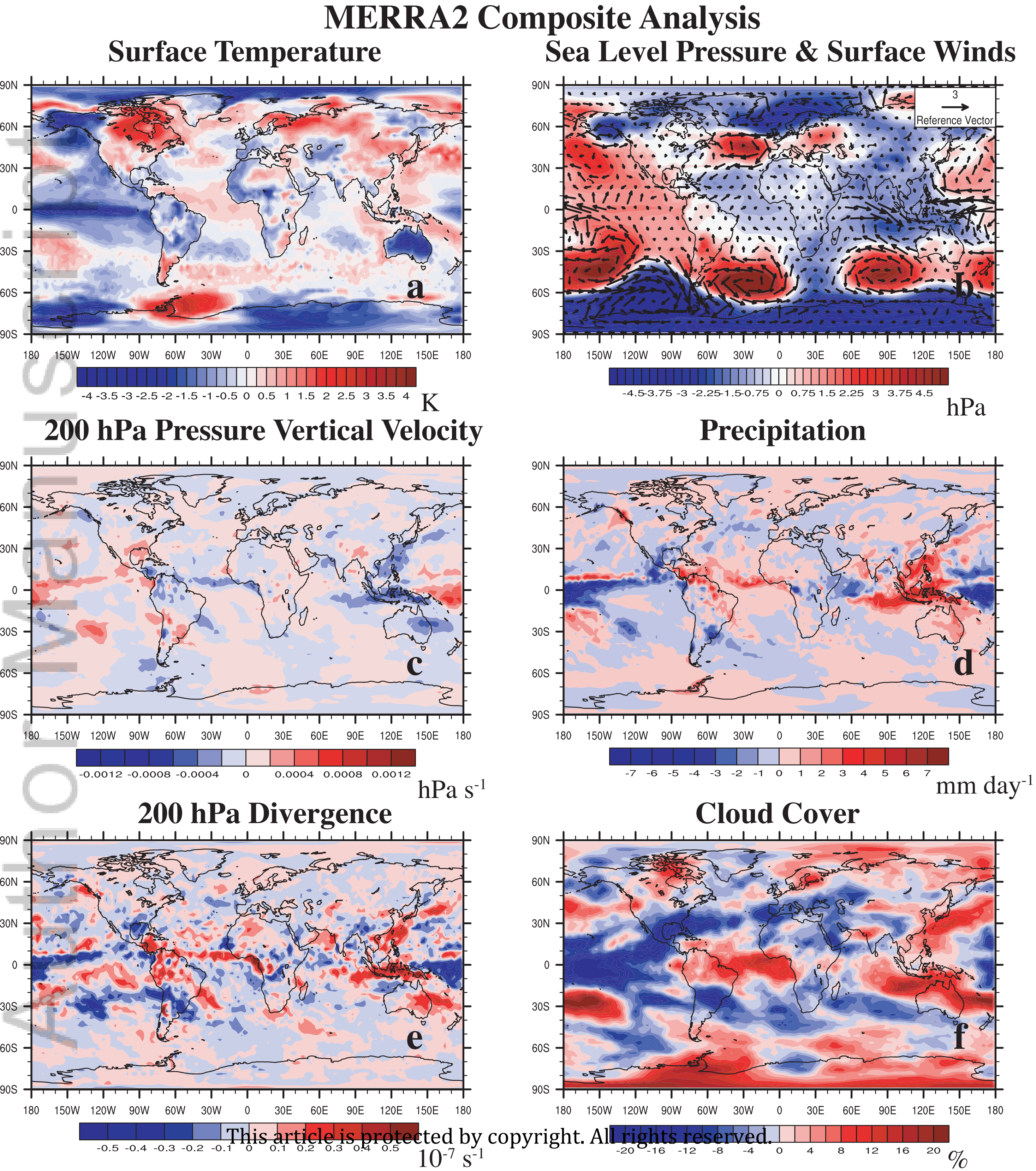
MERRA2 Composite Analysis
Surface Temperature
a
K
-4 -3.5 -3 -2.5 -2 -1.5 -1 -0.5 0 0.5 1 1.5 2 2.5 3 3.5 4
Sea Level Pressure & Surface Winds
3
Reference Vector
b
hPa
-4.5 -3.75 -3 -2.25 -1.5 -0.75 0 0.75 1.5 2.25 3 3.75 4.5
200 hPa Pressure Vertical Velocity
c
-0.0012 -0.0008 -0.0004 0 0.0004 0.0008 0.0012
hPa s-1
Precipitation
d
-7 -6 -5 -4 -3 -2 -1 0 1 2 3 4 5 6 7
mm day-1
200 hPa Divergence
e
-0.5 -0.4 -0.3 -0.2 -0.1 0 0.1 0.2 0.3 0.4 0.5
10-7 s-1
Cloud Cover
f
-20 -16 -12 -8 -4 0 4 8 12 16 20
%
90N 60N 30N 0 30S 60S 90S
180 150W 120W 90W 60W 30W 0 30E 60E 90E 120E 150E 180

Figure 15.

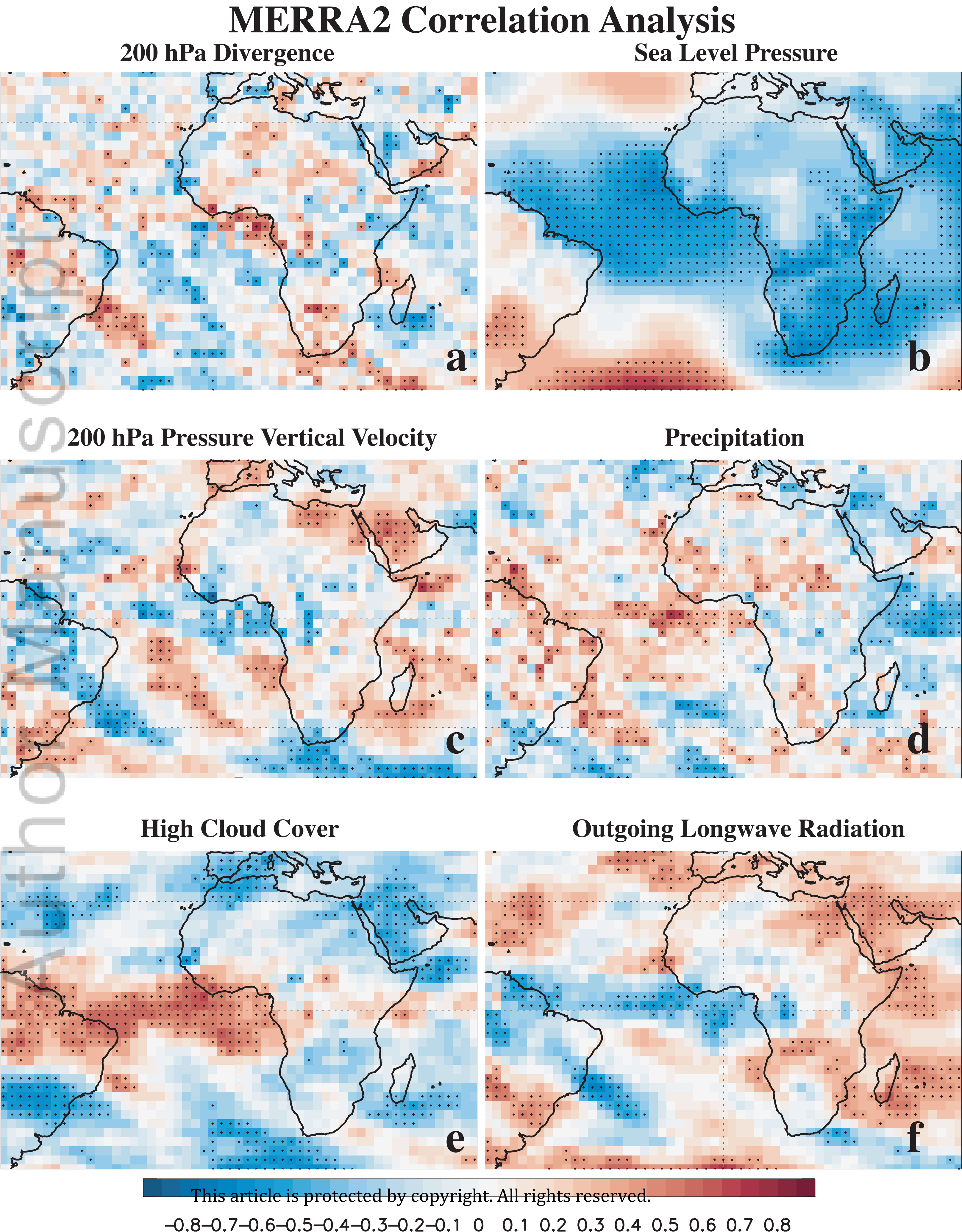
MERRA2 Correlation Analysis
200 hPa Divergence
a
Sea Level Pressure
b
200 hPa Pressure Vertical Velocity
c
Precipitation
d
High Cloud Cover
e
Outgoing Longwave Radiation
f
−0.8 −0.7 −0.6 −0.5 −0.4 −0.3 −0.2 −0.1 0 0.1 0.2 0.3 0.4 0.5 0.6 0.7 0.8

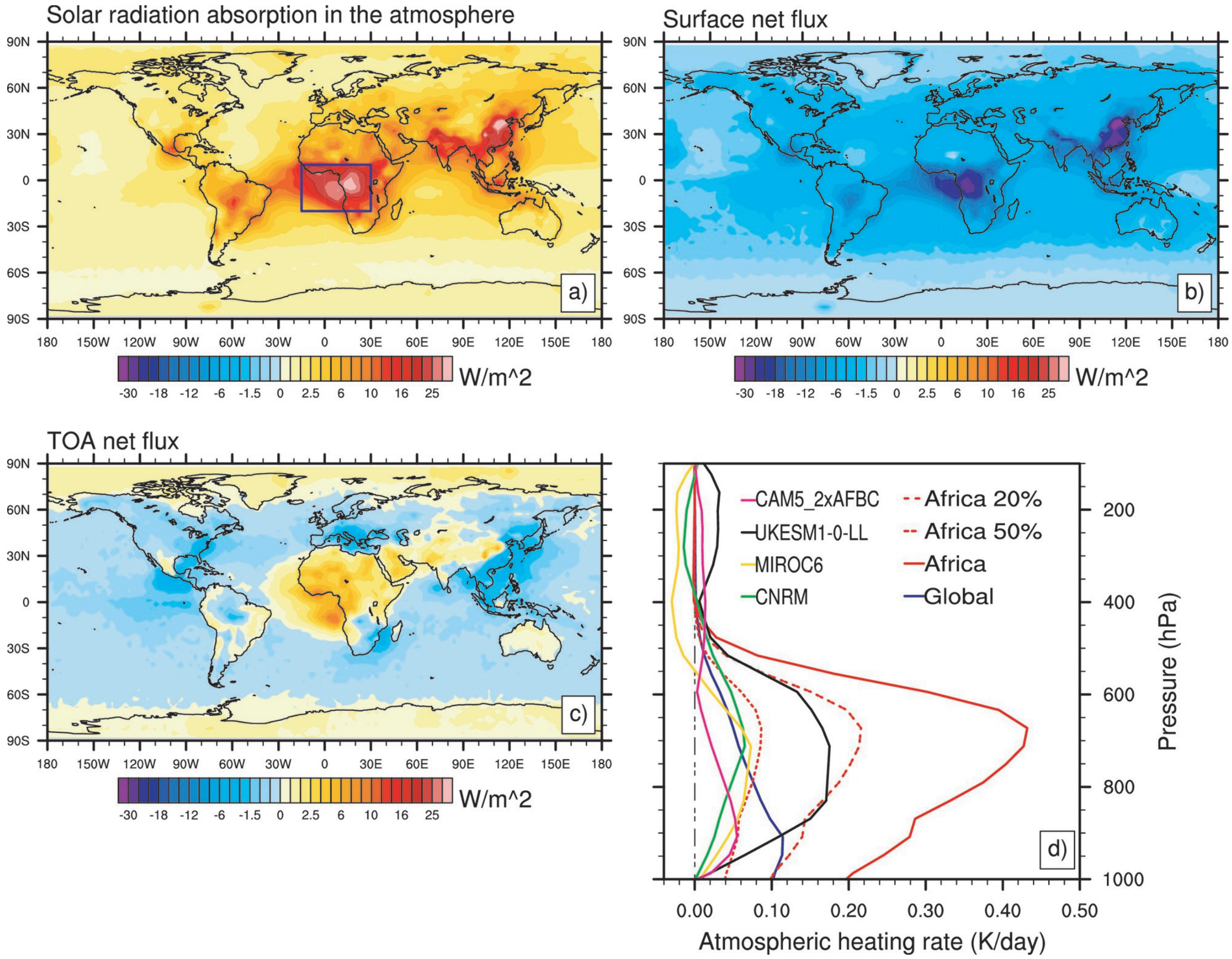

2019jd031832-f01-z-.eps

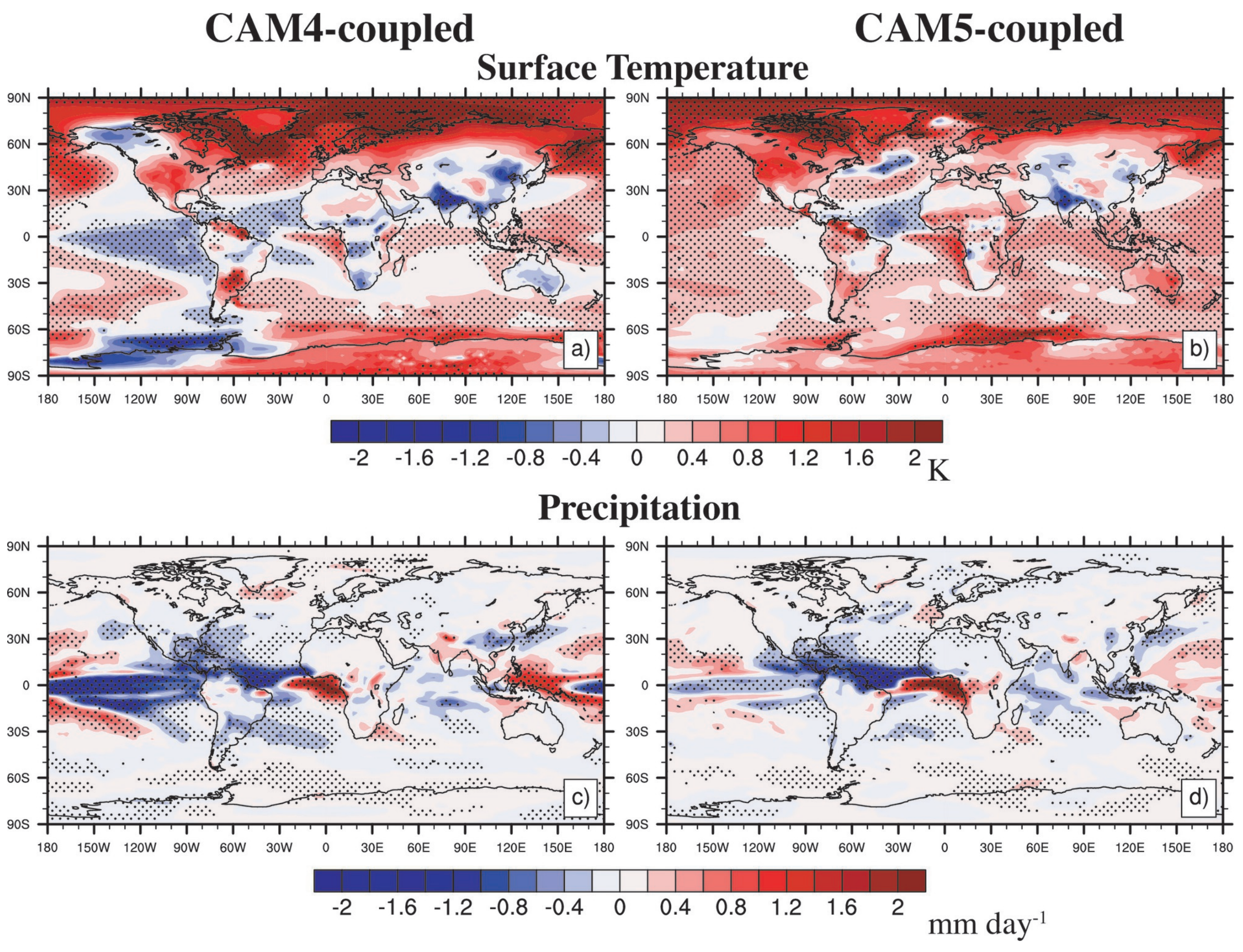

2019jd031832-f02-z-.eps

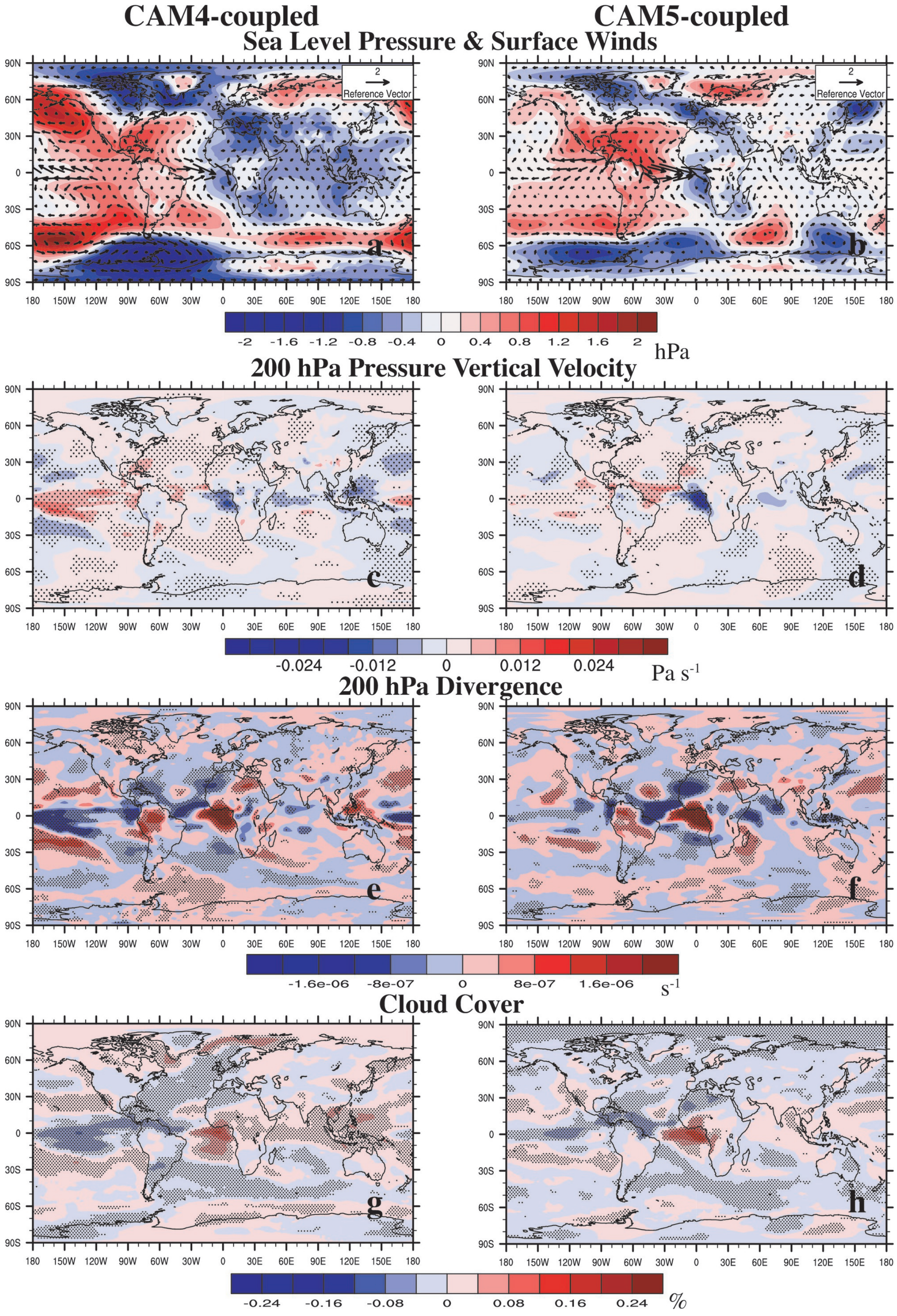

2019jd031832-f03-z-.eps

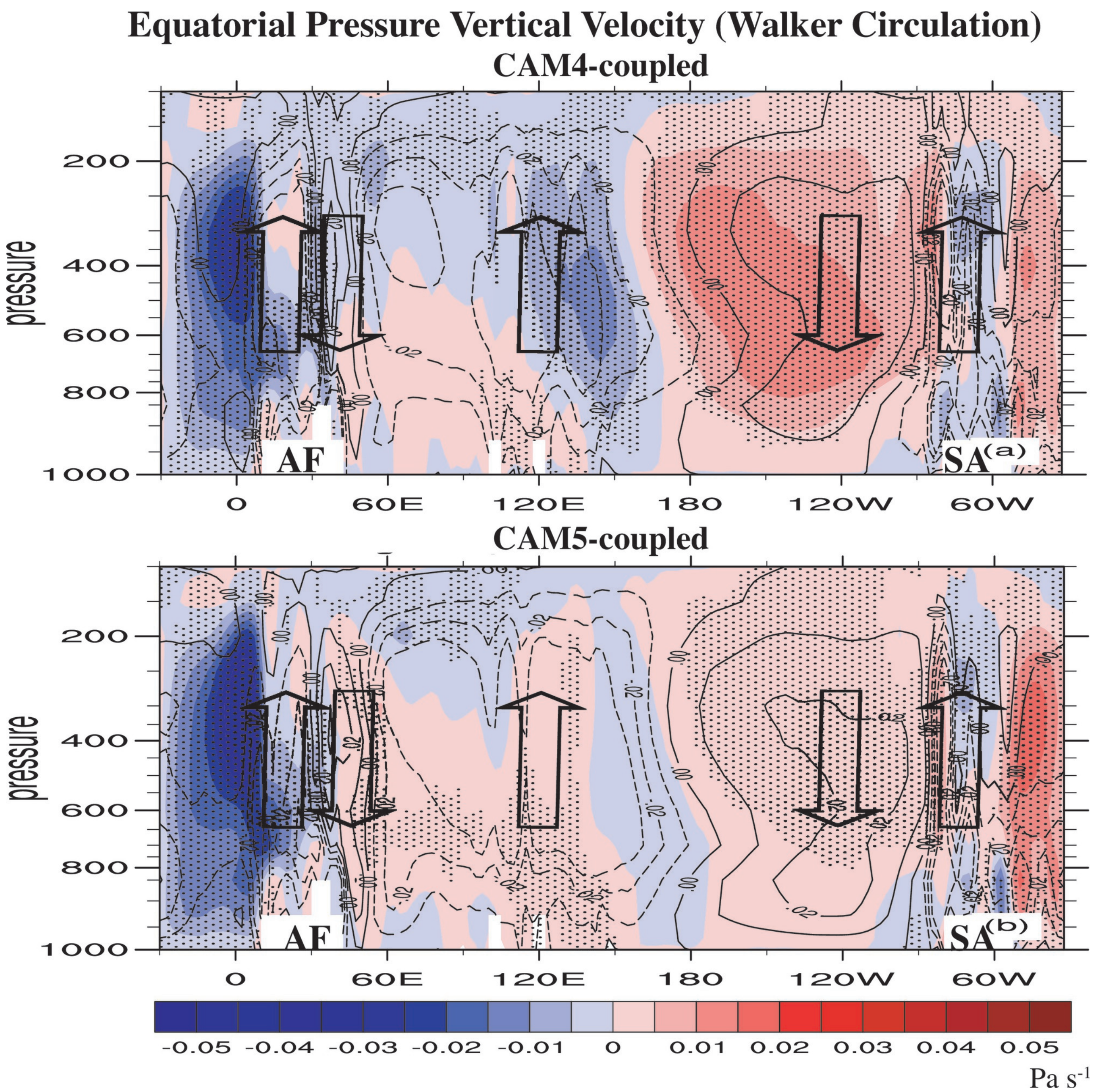

2019jd031832-f04-z-.eps

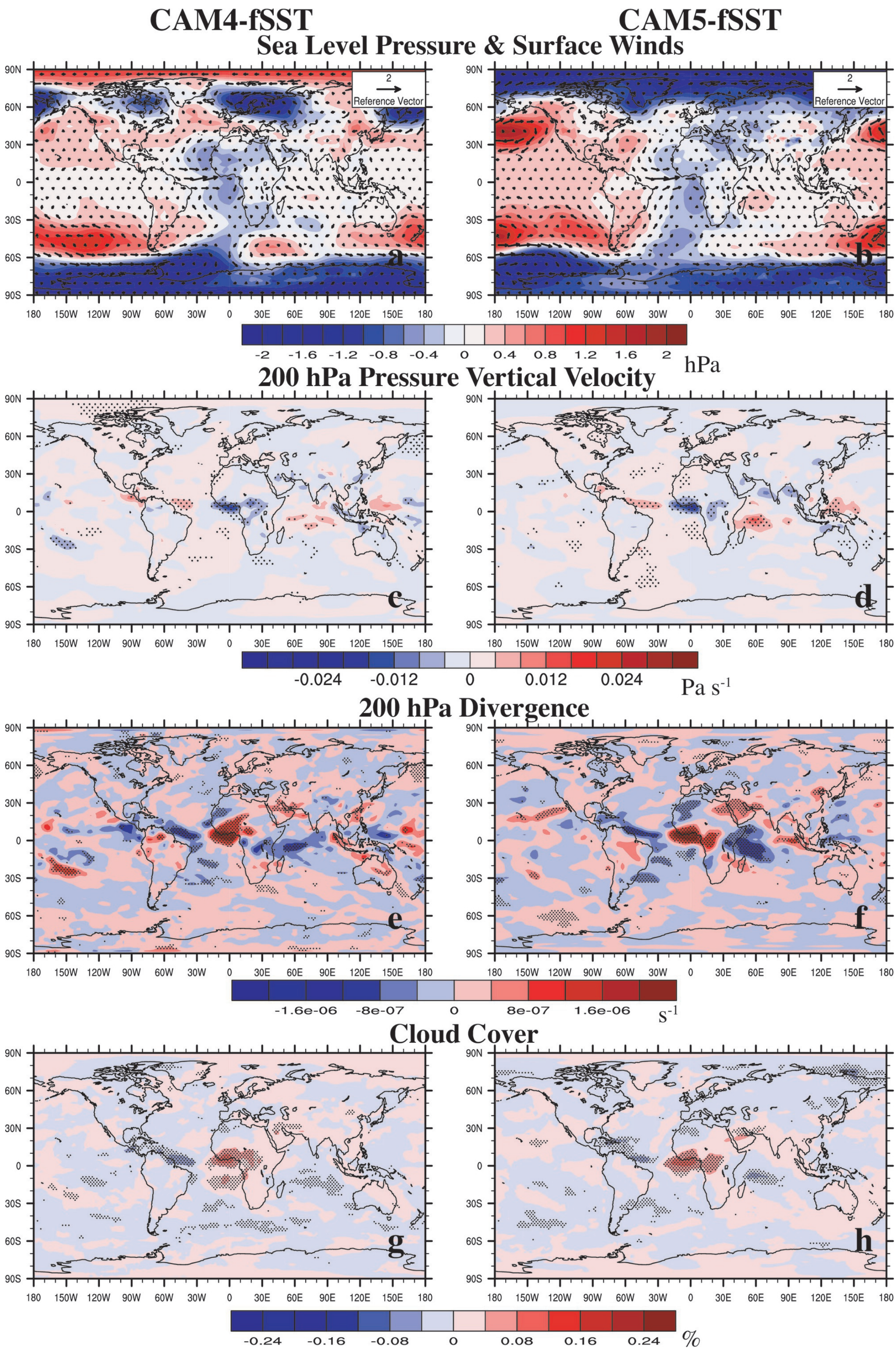

2019jd031832-f05-z-.eps

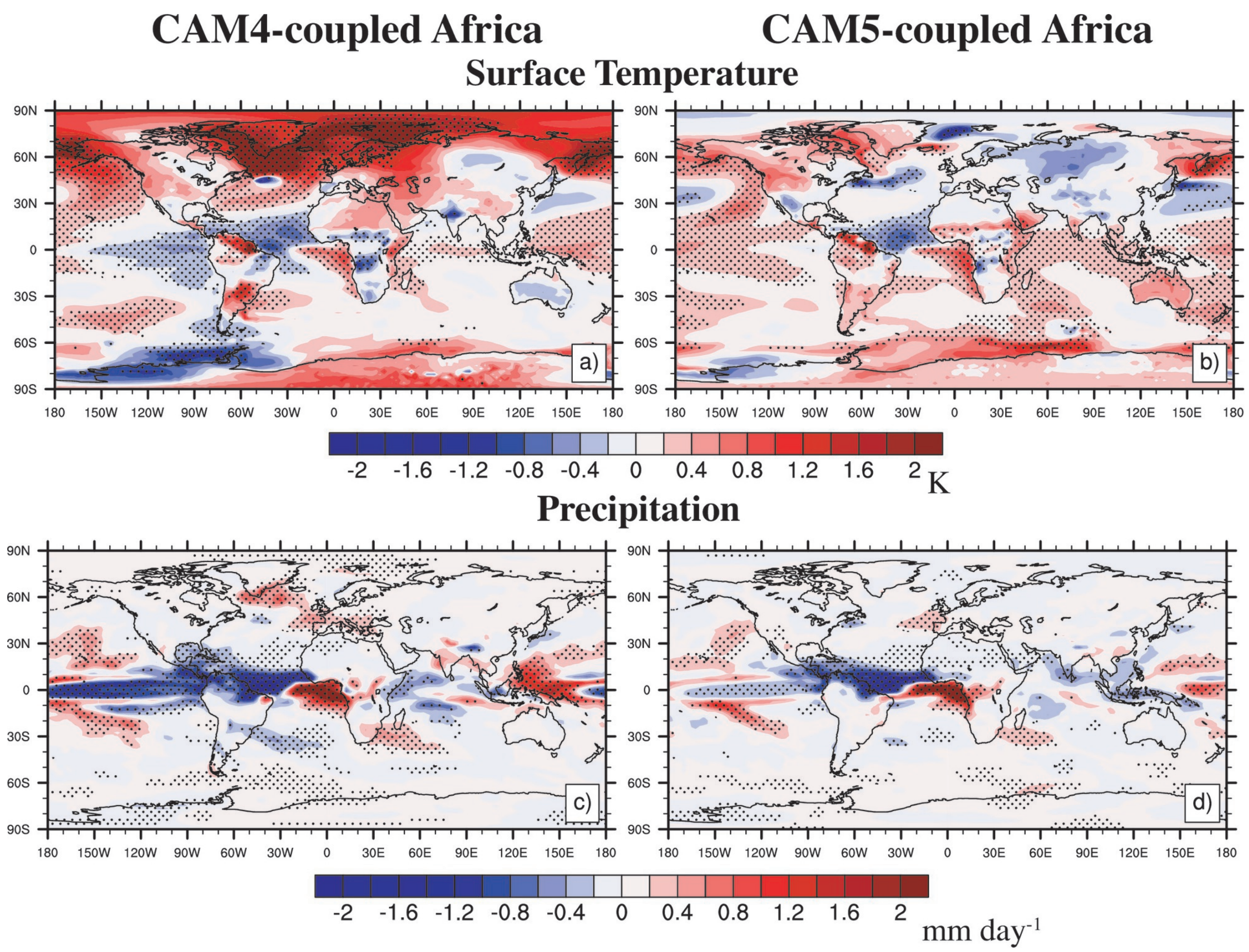

2019jd031832-f06-z-.eps

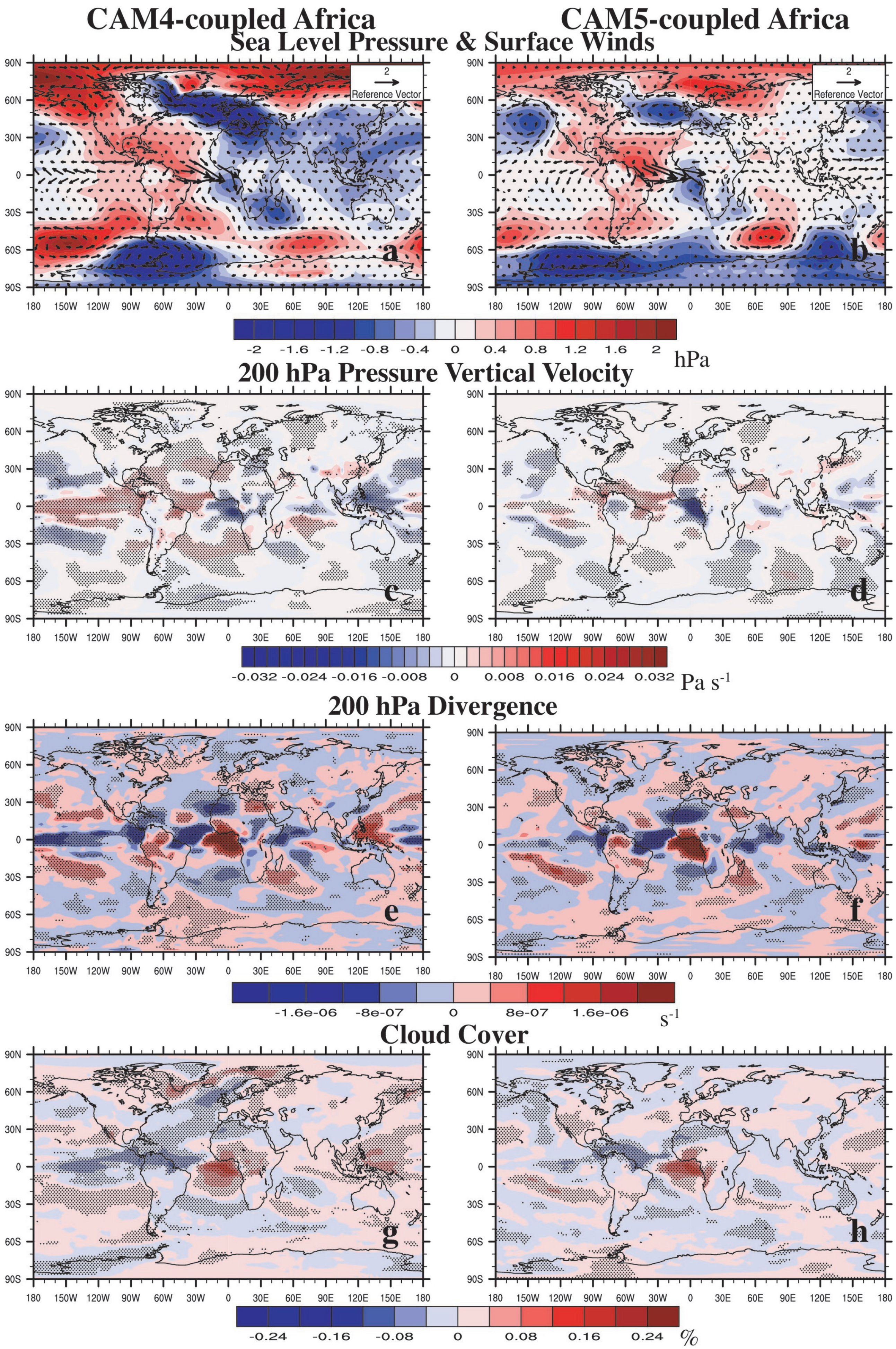

2019jd031832-f07-z-.eps

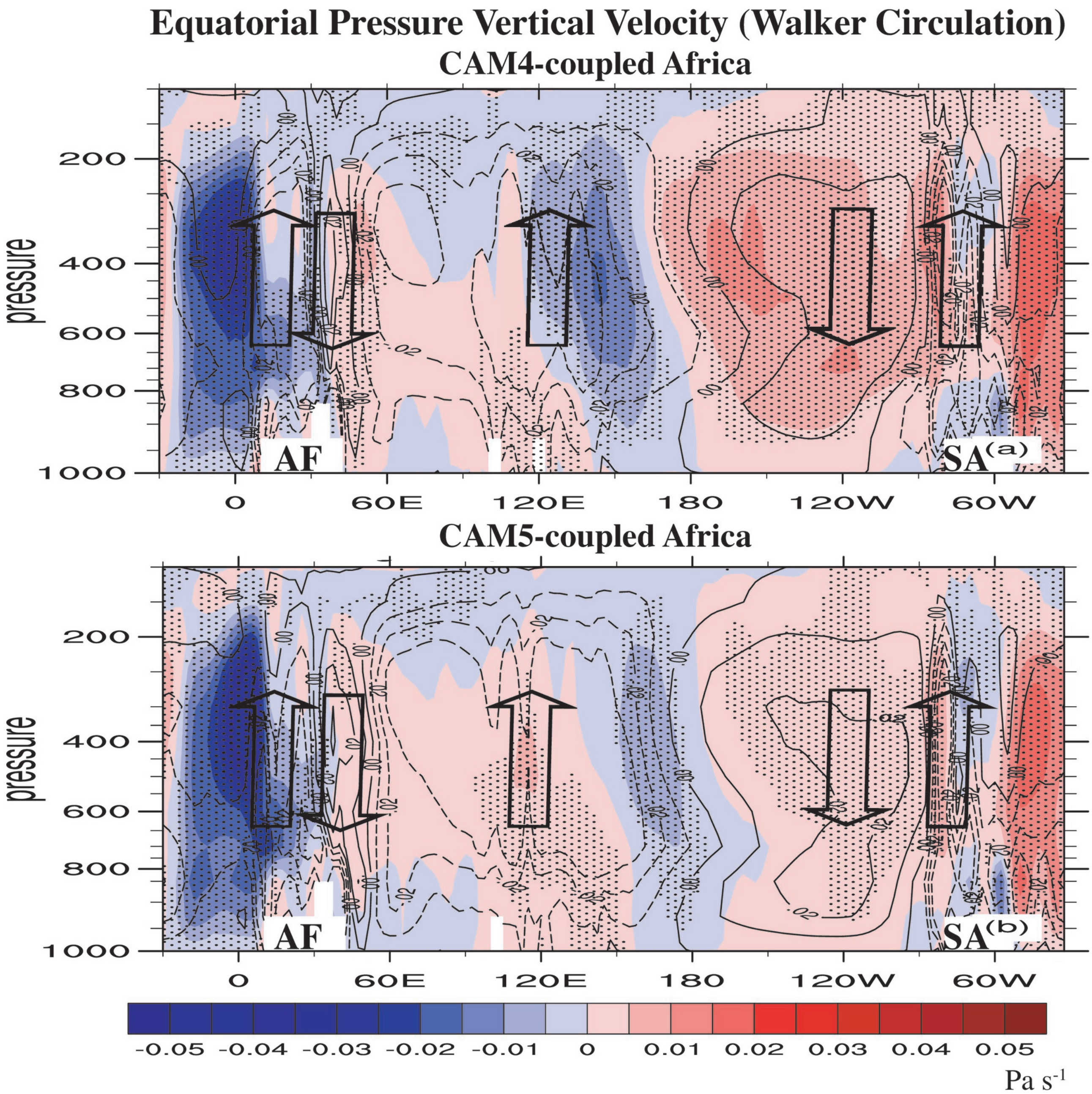

2019jd031832-f08-z-.eps

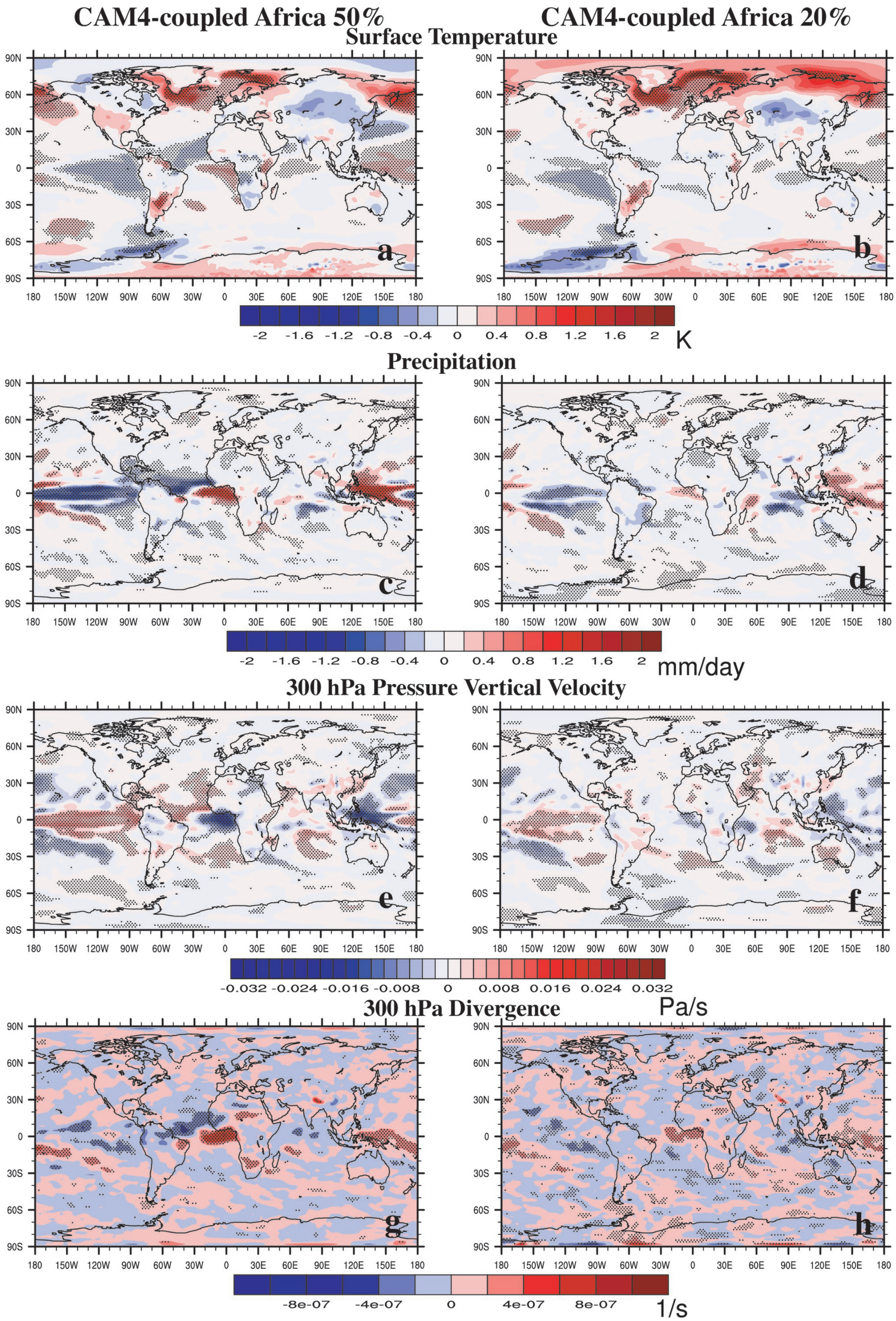

2019jd031832-f09-z-.eps

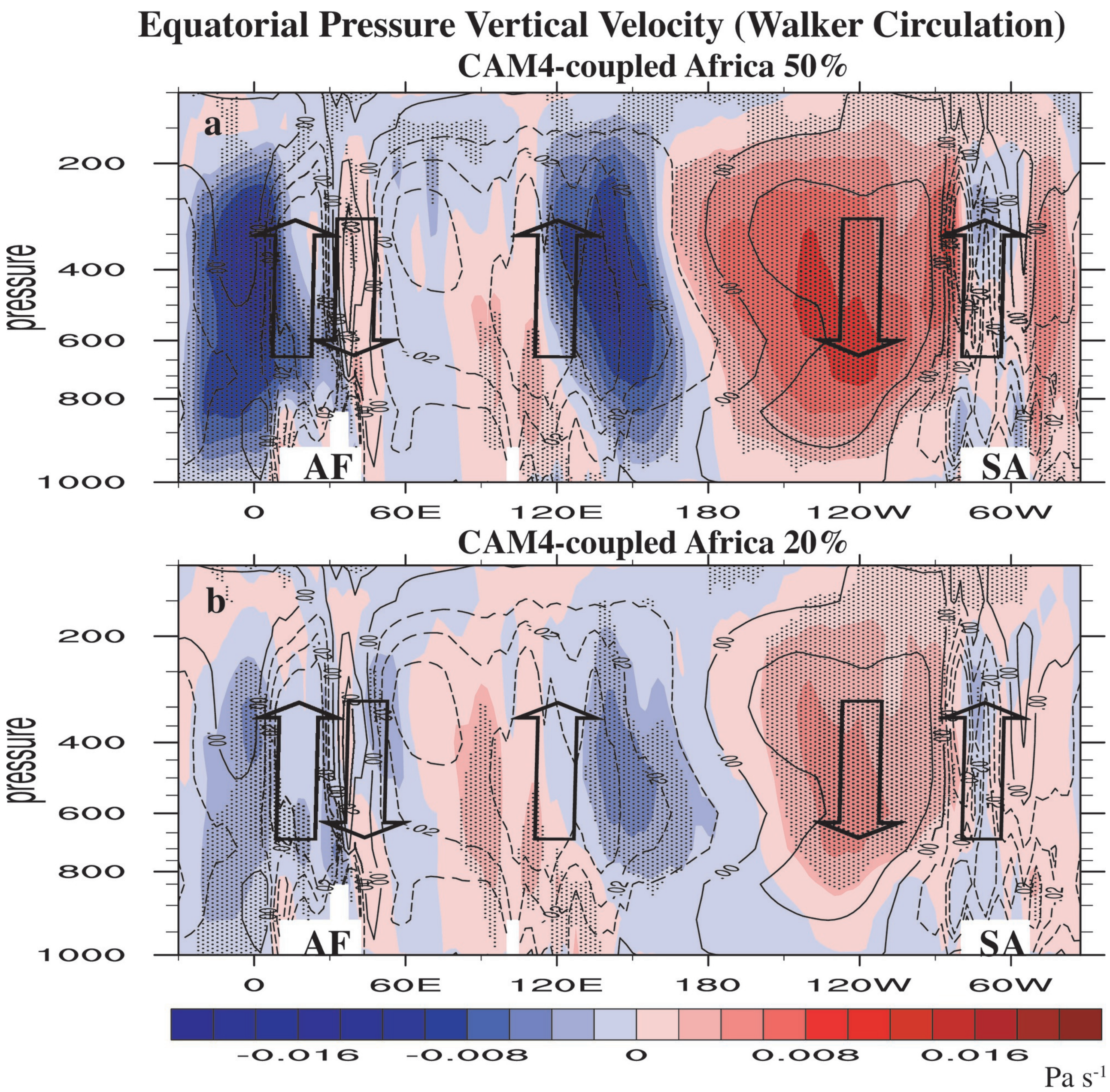

2019jd031832-f10-z-.eps

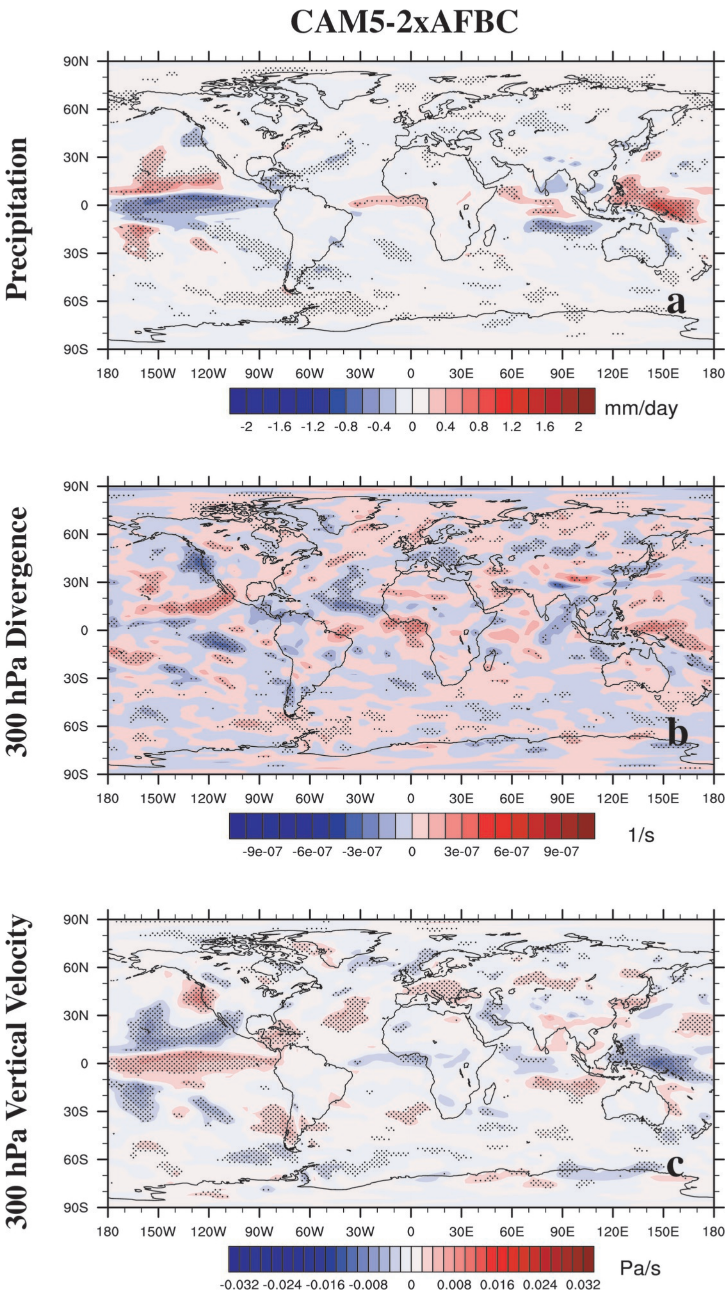

2019jd031832-f11-z-.eps

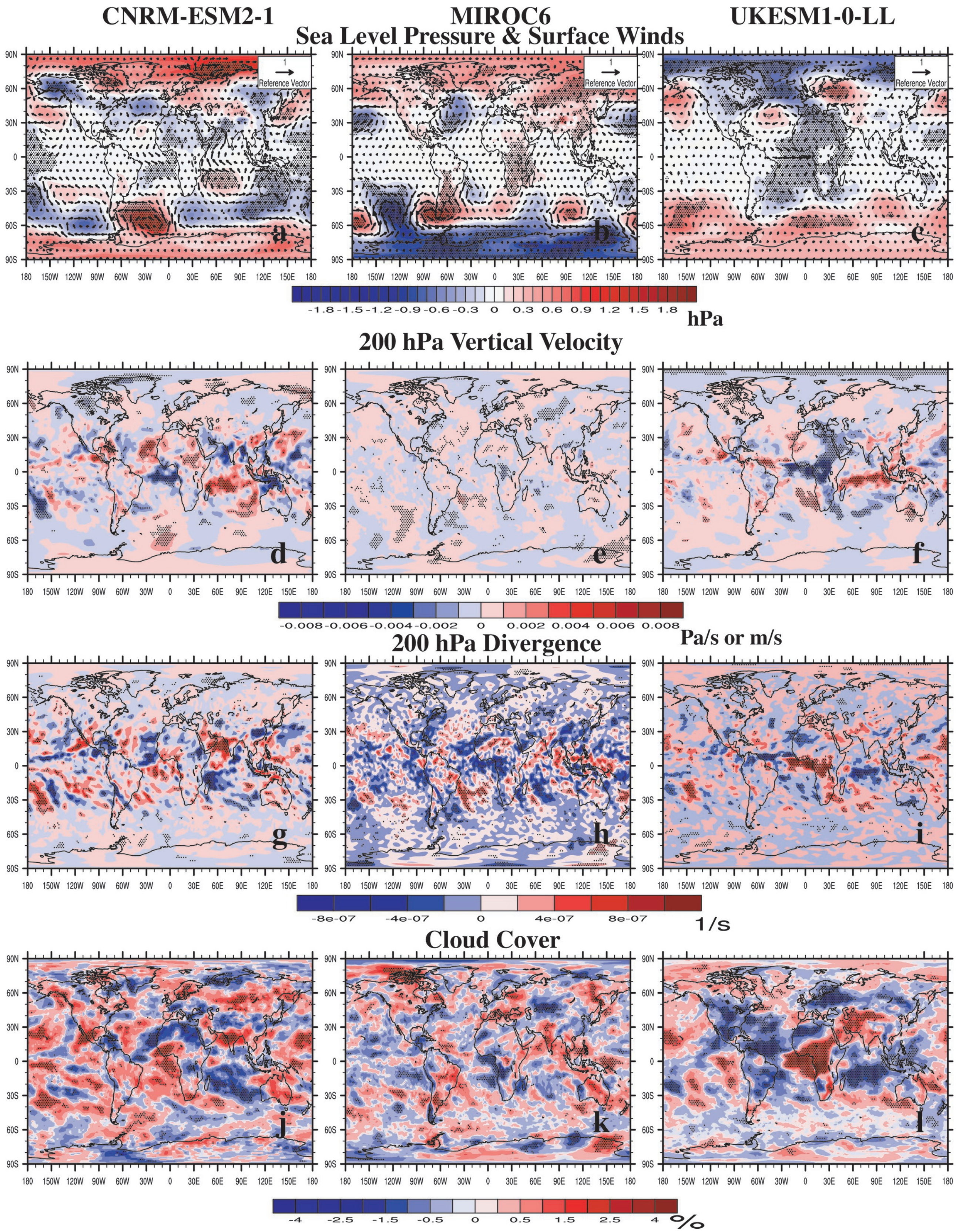

2019jd031832-f12-z-.eps

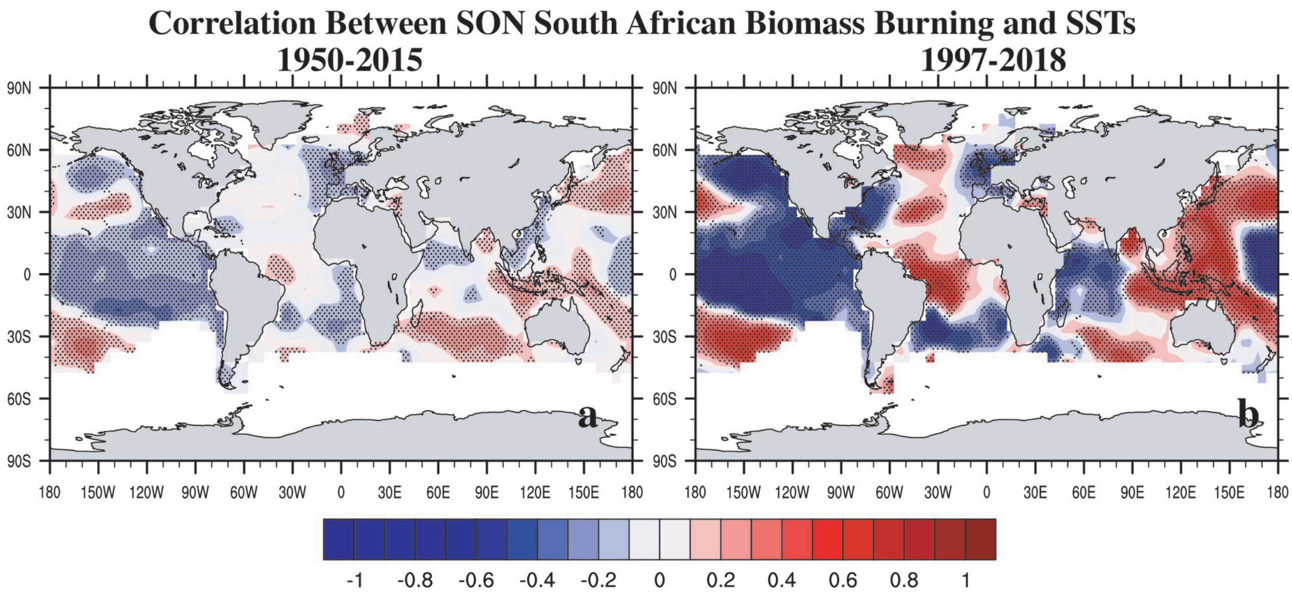

2019jd031832-f13-z-.eps

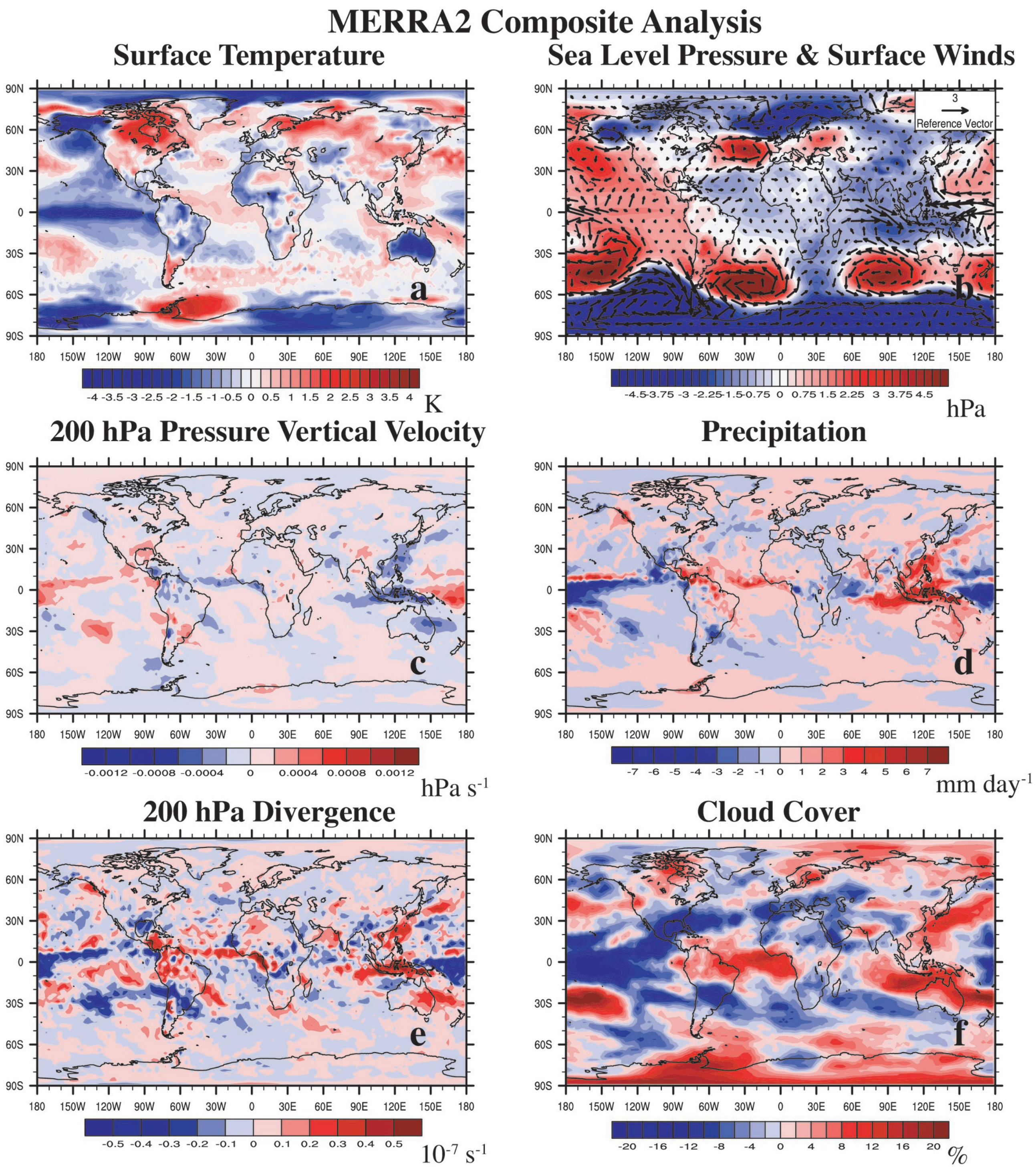

2019jd031832-f14-z-.eps

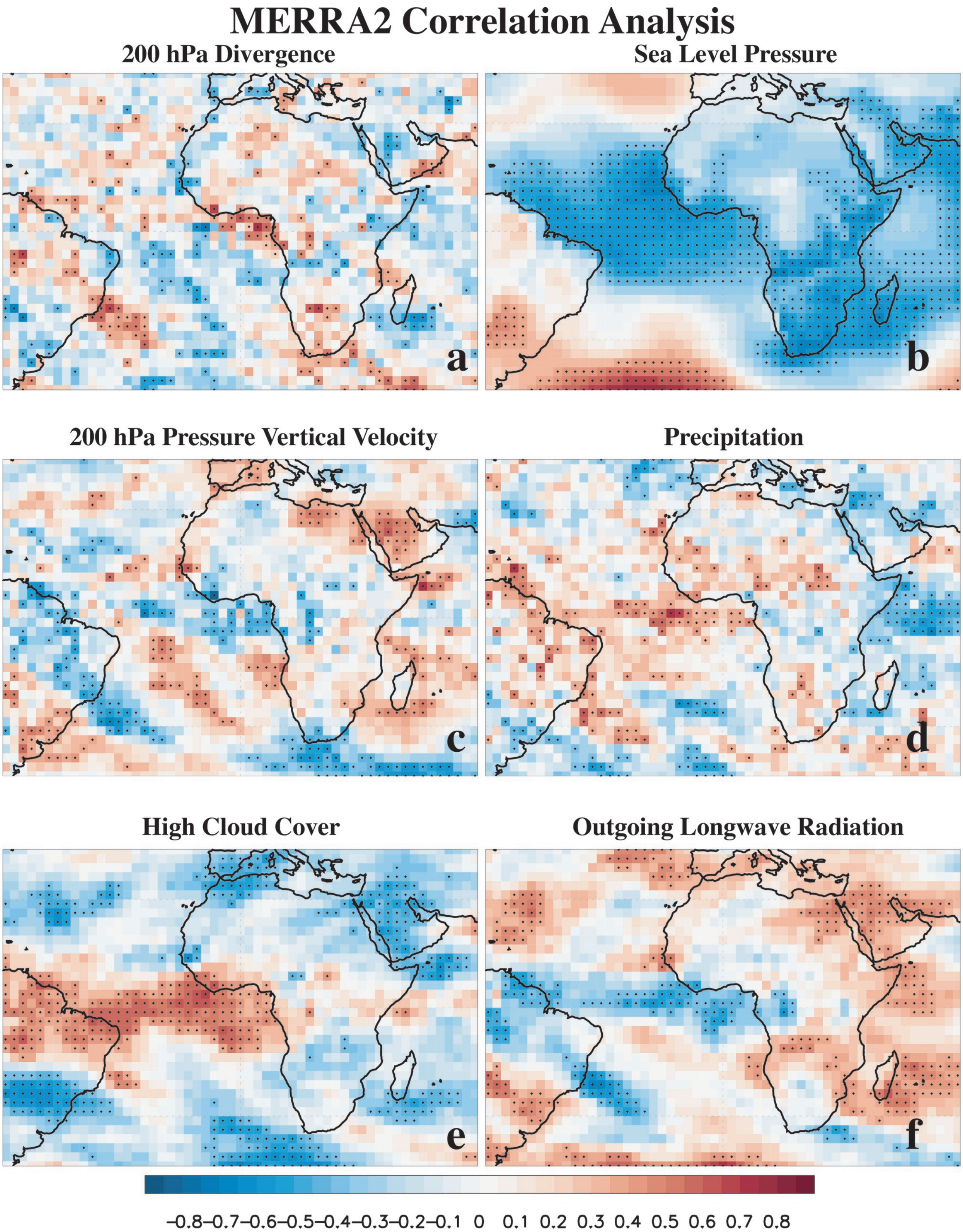

2019jd031832-f15-z-.eps